UNIVERSITA' DEGLI STUDI DI PADOVA

SCUOLA DI SCIENZE

Dipartimento di Geoscienze

Direttrice Prof.ssa Cristina Stefani

TESI DI LAUREA MAGISTRALE

IN

GEOLOGIA E GEOLOGIA TECNICA

STUDY OF CARBON PHASES IN METEORITES

Relatore: Prof. Fabrizio Nestola

Correlatore: Dr.ssa Anna Maria Fioretti

Laureanda: Anna Barbaro

n. matricola 1156600

Anno accademico 2017/2018

ABSTRACT

Almahata Sitta is the first meteorite originated from detonation of a known asteroid, which is the 2008TC_3 asteroid. Such asteroid was discovered on October 6th 2008 and tracked a few hours before it hit Earth on Nubian Desert, Sudan.

Past and ongoing studies on the Almahata Sitta meteorite (ASM) fragments show a great lithological diversity, so that the meteorite is defined as *"polymictic breccias"*. The samples contain different lithologies of ureilitic rocks and enstatite, ordinary, carbonaceous and Rumuruti chondrites.

This Master thesis focuses on the investigation of carbon phases present in ASM. Diamonds and graphite from ASM have been investigated using several methodological approaches, based on Scanning Electron Microscopy (SEM), Micro-Raman Spectroscopy (MRS) and Micro X-Ray powder diffraction (MXR), to ultimately unravel the geological processes behind their crystallization. The investigation of crystallite size of diamonds is used to better understand their origin within the ASM fragments.

The results from SEM analyses provide morphological information on graphite beds and several information about textural aspects of ASM ureilitic fragments.

The results from MRS provide a I(D)/I(G) ratio (with I = intensity; D = D band of graphite; G band of graphite) between 0.3 and 0.6 collocating the graphite phase of analysed sample in Stage 1) of amorphized trajectory determined by Ferrari and Robertson (2000), which correspond to graphite up to nanographite step.

The characterization of the crystalline size of graphite at nanometric scale (~100 nm) using the Tunistra and Koenig equation (Tuinstra and Koenig, 1970) also supports the collocation of graphite phases in our samples in Stage 1) of amorphized trajectory (Ferrari and Robertson, 2000).

The application of literature graphite geothermometry based on the FWHM data of graphite G-band provides an average maximum temperature of ~ 1200-1300 (± 120) °C.

Crystallite size of diamond was determined for each sample using line profile analysis by micro-XR powder diffraction data. Such analysis indicates that diamonds in ASM studied in this work is nanometric (between about 10 and 40 nm). In addition, the X-ray data clearly show the presence of lonsdaleite, a defect stacking diamond, which is a typical feature deriving from impact events.

Concluding, the above results definitively suggest that the diamond formation could be better explained in terms of an impact event investing a pre-existing graphitic or carbonaceous material. The presence of lonsdaleite would confirm such formation conditions.

RIASSUNTO

Almahata Sitta è la prima meteorite originatasi dalla detonazione di un asteroide già conosciuto ed identificato precedentemente al suo impatto, a cui è stato attribuito il nome di asteroide 2008TC_3. Questo asteroide è stato scoperto il 6 Ottobre del 2008 e poche ore prima del suo impatto con l'atmosfera terrestre ne è stata tracciata la traiettoria di collisione con la Terra, che è avvenuta nel deserto di Nubia in Sudan.

Da studi passati, e tuttora in corso, sui frammenti della meteorite di Almahata Sitta (ASM) si è vista una grande diversità litologica, per questo motivo questa meteorite è stata identificata come "breccia polimittica". I campioni di *ASM* contengono differenti litologie composte da rocce sia ureilitiche che condritiche (condriti ad enstatite, condriti ordinarie e carboniose e un frammento di condrite tipo Rumuruti).

Questa tesi magistrale è focalizzata sull'investigazione delle fasi a carbonio presenti in *ASM*.

Il Diamante e la Grafite appartenenti a *ASM* sono stati investigati tramite approcci multi- metodologici, basati sull'uso di Microscopia Elettronica a Scansione (SEM), Spettroscopia Micro-Raman (MRS) e Micro diffrazione da polveri RX (MXR), con il fine di svelare i processi geologici celati dietro la loro cristallizzazione. L'investigazione della taglia del cristallite dei diamanti è stata utilizzata per meglio comprendere l'origine dei diamanti ritrovati all'interno della *ASM*.

I risultati delle analisi SEM hanno conferito informazioni sulla morfologia dei letti di Grafite e altre importanti dettagli sull'aspetto tessiturale dei frammenti ureilitici di *ASM*.

I risultati ottenuti dalla MRS riportano valori del rapporto I(D)/I(G) (dove I=intensità; D= picco della D-band; G= picco della G-band) compresi tra 0.3 e 0.6, i quali suggeriscono la collocazione della fase Grafite, presente nei campioni analizzati, nello Stadio 1) della traiettoria di amorfizzazione determinata da Ferrari e Robertson (2000), che corrisponde al passaggio da Grafite a nanografite.

E’ stata effettuata la caratterizzazione della taglia cristallina della grafite, risultata essere alla scala nanometrica (~100 nm), stimata con l’equazione di Tunistra and Koenig (Tuinstra e Koenig, 1970); questa stima supporta la collocazione della fase Grafite dei campioni analizzati nello Stage 1) della traiettoria di (Ferrari and Robertson, 2000).
L’applicazione di un geotermometro a grafite trovato in letteratura, basato sull’utilizzo di dati della FWHM della banda-G della grafite, descrive un intervallo di temperature massime ~ 1200-1300 (± 120) °C.

La taglia del cristallite del diamante è stata determinata in ogni campione analizzato usando l’analisi del profilo di picco su dati ottenuti tramite micro-RX diffrazione da polveri. La taglia del cristallite è stata stimata e sembra corrispondere a scala nanometrica (tra 10 e 40 nm). Inoltre, i dati di diffrazione mostrano chiaramente la presenza di lonsdaleite, difetto di impilamento del diamante, la quale è riscontrato essere tipica di eventi da impatto.

Infine, questi risultati suggeriscono che la spiegazione alla ancora non definita formazione dei diamanti sia più congrua con un evento di impatto, che è andato ad investire la grafite (o materiale carbonioso) già preesistente. Inoltre, la presenza della lonsdaleite è un’ulteriore conferma alle condizioni di formazione proposte.

INDEX

Chapter V

INTRODUCTION

The main aim of this Master thesis is the investigation of carbon phases in meteorites. This study will allow to identify and to analyse the carbon phases in some fragments of an important meteorite, called *Almahata Sitta meteorite (ASM)*, which represents the totality of fragments of asteroid $2008TC_3$. Among the carbon phases in *ASM* fragments, this research mainly focuses on diamonds and graphite phases.

Diamond and graphite from *ASM* have been investigated using several methodological approaches, based on Scanning Electron Microscopy, Micro-Raman Spectroscopy and Micro XR powder diffraction, to ultimately unravel the geological processes behind their crystallization. The investigation of crystallite size of diamonds is used to better understand the origin of diamonds inside the ASM fragments.

Scanning Electron Microscopy, micro-Raman Spectroscopy and micro-XR Powder Diffraction were respectively conduct at CEASC ("Centro di Analisi per la Certificazione") of University of Padua, at Chemistry Science department of University of Padua and at Paul Scherrer Institute (PSI) in Switzerland, respectively.

The project was conducted in collaboration with University of Pavia, where an expert in meteorite research group headed by Prof. M. Chiara Domeneghetti, Dr. Anna Fioretti of IGG-CNR Padova and with external help of Prof. Cyrena A. Goodrich of Lunar and Planetary Institute of Houston.

Fragment of Almahata Sitta Meteorite in Nubian desert – Sudan.

Chapter I

Evolution of Almahata Sitta meteorite

1 EVOLUTION OF ALMAHATA SITTA METEORITE FRAGMENTS

1.1 Detection of Asteroid 2008TC$_3$

The samples analysed during this Master thesis derived from disintegration of Asteroid 2008TC$_3$, which impacted Earth on 7th October 2008 (Shaddad et al., 2010). The terms "asteroid" or "minor planet" have usually been applied to any astronomical objectives orbiting the Sun that did not exhibit the disc of a planet and did not show also the characteristics of an active comet (Rossi, 2018).

The importance of this asteroid is attributed to its detection in space before its impact with Earth. Richard Kovalski of the Catalina Sky Survey at Mt. Lemmon Observatory discovered this asteroid on October 6th, 2008, 20 hours before its impact on Earth (Shaddad et al., 2010). Asteroid 2008TC$_3$ was monitored from 11 hours before its impact, and Nubian Desert, northern Sudan, was identified as the impact area (Jenniskens et al., 2009).The figure 1.1a shows the trajectory of impact of asteroid 2008TC$_3$ while the rectangular in the figure 1.1b defines the impact area in Nubian desert.

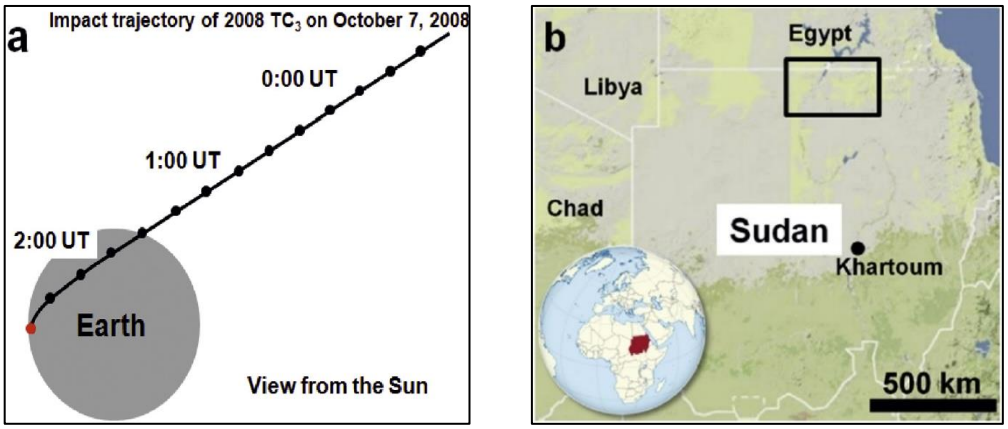

Figures 1.1 a) Calculated trajectory of asteroid 2008 TC3 on October 7th, 2008,as seen from the sun; **b)** Map of Sudan and adjacent countries (Horstmann and Bischoff, 2014).

The enter of asteroid 2008TC$_3$ in the atmosphere was observed by many eyewitnesses (Jenniskens et al., 2009, 2010) at Egypt-Sudan border, called Wadi

Halfa, and also close to the train station named Station 6, located in the Nubian Desert between Wadi Halfa and the city of Khartoum; this object was described as "rocket-like fireball with an abrupt ending" (Jenniskens et al., 2009), as showed in figure 1.2.

Figure 1.2 Photograph of the lingering trail/dust cloud of asteroid 2008 TC3over northern Sudan taken at early dawn October 7, 2008 (Shaddad et al., 2010).

Asteroid 2008TC_3 travelled from the geodetic longitude of 31.80° E and latitude of 20.85° N at an altitude of 50 km to 32.58° E and 20.71° N at 20 km altitude (Jenniskens et al., 2009). The impact was also observed by Meteosat 8 satellite, and the geographical coordinates of the spot in the visual and near-infrared channels at moment of deflagration were at longitude 32.16° E and latitude 20.97° N (WGS-84 ellipsoid) (Borovička and Charvàt, 2008). These coordinates of deflagration of 2008TC_3 are established by assuming that source of light was at sea level.

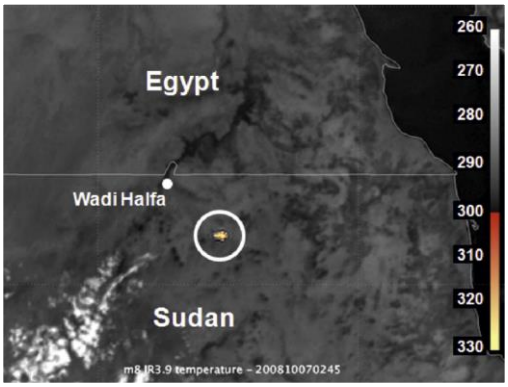

Figure 1.3 Meteosat 8 thermal photograph of the impact location of 2008TC_3 (Shaddad et al., 2010).

The figure 1.3 shows Meteosat 8 thermal photograph of the impact location of asteroid 2008TC_3 in the Nubian Desert, Sudan. The bright yellow spot illustrates that the image was taken at the exact moment when the asteroid detonated at an altitude of ~37 km.

1.2 Recovery of fragments from Asteroid 2008TC_3

The recovery of fragments from asteroid detonation was immediately coordinated by Prof. M. Shaddad of University of Khartoum. The potential search area (60x10 km^2) of 2008TC_3 was located on Southwest of train station 6 in the Nubian Desert, Northern Sudan (figure 1.4).

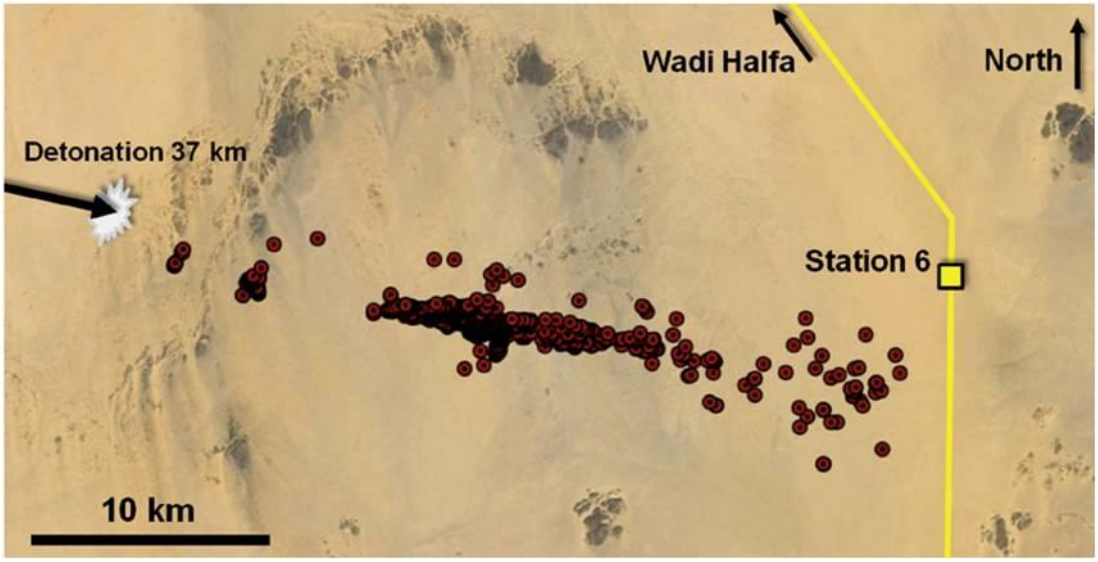

Figure 1.4 60x10 km fall area of 2008 TC_3 in Southwest of Station 6 in Nubian Desert, Sudan (Horstmann and Bischoff, 2014).

Chodas et al. (Shaddad et al., 2010) established the entry into Earth's atmosphere at around 2:45:28 UTC of 2008TC_3, 11 h prior to its atmospheric entry. The detonation of the body was at an altitude of 37 km, while at 2:45:54 the asteroid expected to reach maximum deceleration at an altitude of about 14 km.

The time at which any fragments could reach the ground depended on unknown physical properties of the object, but it was thought to be 52 s later, around 2:46:20 UTC. In the figure 1.4, the black arrow shows the flying trajectory of 2008TC_3,

while the red spots are the geographical coordinates of recovery of every meteorite fragments (Jenniskens et al., 2009; Shaddad et al., 2010).

Search campaigns were planned by Prof. Shaddad on 2008, December 6–8 and December 26–30 with a collaboration of several students and of the staff of University of Khartoum (figure 1.5); these searches were also continued on 2009, February 27–March 02 and 2009, December 9–12 (Shaddad et al., 2010).

Figure 1.5 Members of the first search team pose for a group photo at Station 6 on December 8, 2008, shortly after the successful recovery of 2008 TC3 (Shaddad et al., 2010).

The search consisted on surveys along the estimated ground track (east–west), as well as three surveys tangential to the track in sandy plains near the predicted impact points. The students were very engaged during the recovery of 2008TC_3 fragments and they formed a human chain to identify the fall trajectory of the fragments (figure 1.6).

Figure 1.6 Searching of pieces of *ASM* in Nubian desert on first search campaign (Shaddad et al., 2010).

Prof. Peter Jennisken of Carl Sagan Center of SETI Institute (California) was invited by the University of Khartoum to collaborate in the search campaign. He held a conference at the Physics Department of University of Khartoum on December 3, 2008. After his presentation, Prof. Jennisken with Prof. Shaddad and M. Elhassan, an eyewitness, (figure 1.7) travelled to the fall area to speak with other eyewitnesses. Then they joined together with the searching team, and about 600 stones of $2008TC_3$ were recovered at the end of search campaigns.

Figure 1.7: Prof. Jennisken and Elhassan, an eyewitness, with a fragment of 2008TC3 (Jenniskens et al., 2009; Shaddad et al., 2010).

Suddenly all fragments from $2008TC_3$ asteroid were called ***"Almahata Sitta meteorite"****(ASM)* (Weisberg et al., 2010).*"Almahata Sitta"* in Arabic language means *"Station 6"*, which is the name of the train station near the impact area of asteroid $2008TC_3$.

1.3 Collections of Almahata Sitta meteorite

The main collection of *ASM*, consisted of all fragments recovered by Prof. Shaddad, is situated at University of Khartoum (Sudan) and it is constituted of about 600 stones of *ASM* (Shaddad et al., 2010). At the moment, several fragments are investigated and some of them are temporarily located at Mailcode KT (NASA

Johnson Space Centre, Houston), at Carnegie Institution Washington (Geophysical Laboratory, NW, Washington DC, United States), at SETI Institute (Carl Sagan Centre, Mountain View, California, United States) and also in several European Universities.

Another collection of *ASM* is placed in Germany (the locality was not disclosed), and it consists in all fragments from $2008TC_3$ recovered during another search campaign conducted by Bischoff et al. (2010).

In detail, the fragments investigated during this Master thesis come from the collection of University of Khartoum. This study was realized with the partnership of University of Pavia and IGG-CNR of Padova, which have an international collaboration with University of Khartoum.

Chapter II

Mineralogy and Petrology of Almahata Sitta fragments

2 MINERALOGY AND PETROLOGY OF ALMAHATA SITTA FRAGMENTS

2.1 General overview

The *AS* meteorite was firstly classified as an *"anomalous polymictic ureilite"* (Jenniskens et al., 2009), but, after additional samples studied, turned out to be a *"complex polymictic breccia"* (Bischoff et al., 2010) because of several types of chondritic lithologies and a-chondritic lithologies samples are identified among its fragments.

Among the achondrites found in *ASM*, this Master thesis is focused to investigate ureilites fragments of *ASM*. Only the 10% of the ureilites samples are defined as *"polymictic breccias"* owing to few percentage of feldspatic mineralogical component (Mittlefehldt et al., 1998). The figure 2.1 reports several fragments of *ASM* with ureilite textures and many other textures.

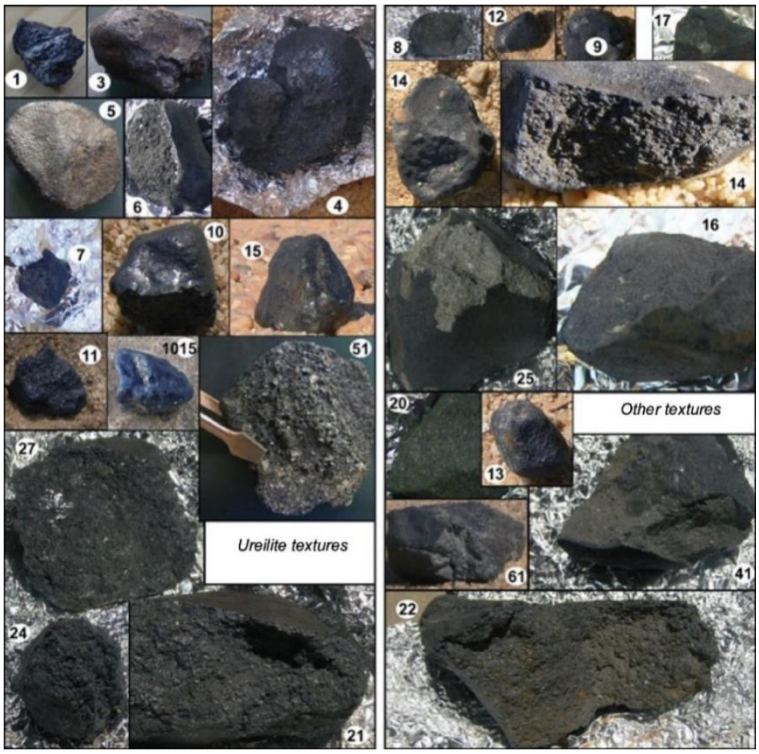

Figure 2.1 Examples of Almahata Sitta meteorites with ureilite textures (left) and other textures (right). The image scale for each meteorite varies from 2.5 cm to 8 cm (Horstmann and Bischoff, 2014).

2.2 Ureilites fragments

Ureilites constitute the second largest group of achondritic meteorites (figure 2.2). They are ultramafic rocks mainly composed of olivine and pyroxene. Pyroxene is the most abundant component in this type of rocks and the most abundant is pigeonite, the monoclinic clinopyroxene. Several assemblages of pigeonite, augite, and orthopyroxenes always occur (Rossi, 2018). Ureilites contain significant amounts of interstitial carbon which is either present as graphite or diamonds. The study of interstitial diamonds and the graphite beds are the main focus of this Master thesis.

Among the achondrites, only ureilites have preserved a primitive oxygen-isotopic composition and scatter along the carbonaceous chondrite anhydrous mineral mixing line (Rossi, 2018). *Ureilites* are surely achondrites, but their formation is almost unclear and controversially discussed.

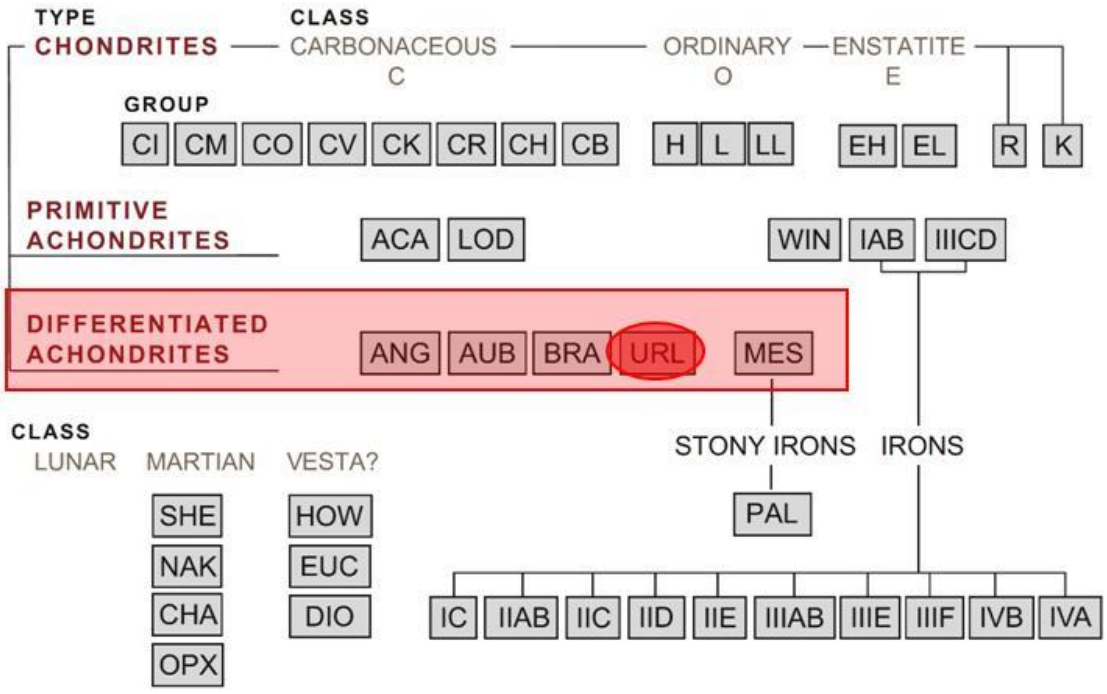

Figure 2.2 Classification of meteorites. ACA acapulcoites, *LOD* lodranite, *WIN* winonaites, *ANG* angrites, *AUB* aubrites, *MES* mesosiderites, *BRA* brachinites, *URL* ureilites, *SHE* shergottites, *NAK* nakhlites, *CHA* chassignites, *OPX* orthopyroxenite, *HOW* howardites, *EUC* eucrites, *DIO*diogenites, *PAL* pallasites
(Rossi, 2018).

Ureilites were originally classified as olivine -pigeonite achondrites (GP Vdovykin, 1970) but augite bearing ureilites and orthopyroxene – pigeonite were found (Takeda et al., 1989). Ureilites are generally coarse-grained bi-mineralogic rocks, consisting almost entirely of olivine and pyroxene (Goodrich, 1992).
After the study of some ureilitic fragments of *ASM*, Zolensky et al. (2010) identified three main lithologies:

- Pyroxene dominated, very porous, highly reduced;
- Pyroxene dominated, compact lithology;
- Olivine dominated, compact lithology.

The first lithology is "pyroxene dominated, very porous, highly reduced". Two hues among the fragments are present: dark coloured ones, and lighter-coloured ones; both dark and light lithologies present a similar very porous, fine-grained polycrystalline texture.

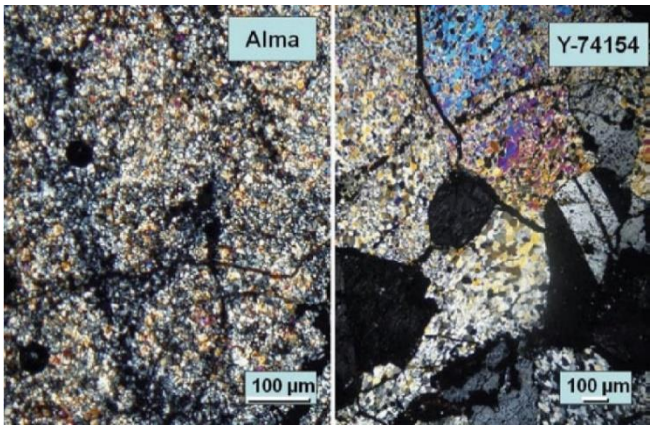

Figure 2.3 Optical photomicrographs (cross-polarized light) of Alma stone 1 (left) and Y-74154 (right), both showing mosaicized texture (Zolensky et al., 2010).

This lithology is mainly dominated by mosaicized pyroxene and olivine, with carbon phases and the presence of minor phases, as Fe-Ni metal.
Pyroxene abundance is usually higher than olivine, and, among pyroxene, the monoclinic clinopyroxene is the most abundant phase (pigeonite). Both pigeonite and olivine show granoblastic mosaic texture (figure 2.3) made up of 10-20 µm grains and rare crystals up to 1 mm in size are even present.

Carbon phases (up to 5 vol%), as graphite or diamond, and metal phases are present interstitially to silicate phases; the variable abundance of these phases probably explains the color differences among samples with the same pyroxene dominated, very porous, highly reduced lithology.

Pyroxene often shows twinning on (100) and it is present between euhedral crystal of olivine grains, at the boundary between olivine-rich and pyroxene rich regions.

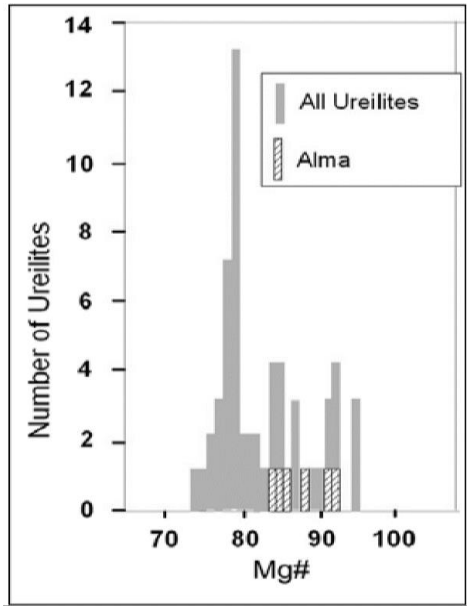

Figure 2.4 Histogram of olivine core composition (Mg#) for any different Alma samples, compared to cores for monomict ureilites (Mittlefehldt et al., 1998). The Alma olivine core compositions are generally distinct for each lithology (Horstmann and Bischoff, 2014).

Among olivines, forsterite (Fo) composition in the ureilitic fragments are quite variable. Olivine adjacent to carbon phases typically shows the reverse zoning characteristic of ureilites. The reverse zoning results from elevated temperature and reduction composition have a narrow range from $Fo_{86.6}$ to $Fo_{86.4}$. Many studies are conducted on Fo composition in ureilites fragments, showing a difference among the olivine composition of ureilites fragments of *ASM* and other many ureilites fragments of any monomict ureilites (Mittlefehldt et al., 1998). The figure 2.4 shows olivine core composition (Mg) of seven different *ASM* samples in confront of olivine core composition of other monomict ureilites. The *ASM* mineralogy of pyroxene dominated, very porous, highly reduced lithology is summarized on Table 2.1.

Table 2.1 Almahata Sitta lithologies mineralogy of pyroxene dominated, very porous, highly reduced lithology (Zolensky et al., 2010).

	pyroxene dominated, very porous, highly reduced lithology	**pyroxene dominated compact lithology**	**olivine dominated compact lithology**
Low-Ca pyroxene	$En_{90\text{-}80}$ $Wo_{3\text{-}10}$	$En_{99\text{-}74.2}$ $Wo_{1\text{-}7.2}$	$En_{75.3\text{-}75.8}$ $Wo_{10.1\text{-}10.3}$
High-Ca pyroxene	En_{57} Wo_{40}	$En_{57.6\text{-}54.9}$ $Wo_{40.6\text{-}35.7}$	$En_{75\text{-}85}$ $Wo_{5\text{-}10.3}$
Olivine	$Fo_{92.4}$-$Fo_{83.6}$, 0.13-0.92 wt% CaO, 0.25-0.6 wt%	$Fo_{95.9}$-$Fo_{86.9}$ 0.19-0.70 wt%CaO, 0.25-0.91 wt%Cr_2O_3, 0.33-0.66 wt% MnO	$Fo_{82.7}$-$Fo_{96.5}$ 0.31-0.51 wt%CaO,0.59-1.06 wt%Cr_2O_3,0.39-0.57 wt% MnO
Olivine cores	$Fo_{86.6}$-$Fo_{86.4}$	$Fo_{86.9}$-$Fo_{86.4}$	$Fo_{82.7}$-$Fo_{83.0}$
Olivine in pores	$Fo_{88\text{-}85}$		
Fe-Ni metals	$Fe_{0.92}Ni_{0.08}$-$Fe_{0.96}Ni_{0.04}$	Fe-Ni metal	Fe-Ni metal
	Troilite with significant Cr	Troilite with significant Cr	Troilite with significant Cr
	Graphite and diamond	Graphite and diamond	Graphite and diamond

"Pyroxene dominated compact lithology" is mainly of pyroxene -rich (<50%), low porosity region, with sometimes the presence of olivine-rich regions, which is usually associated with the highest porosity. Pyroxene and olivine show an intertwining texture similar to major group ureilites (Mittlefehldt et al., 1998), with individual pyroxene and olivine crystals measuring 500 μm and 200 μm respectively.

The graphite in *ASM* fragments pyroxene dominated compact lithology mainly occurs as fine, friable masses within the fine-grained aggregates; some fragments of *ASM* ureilites apparently contain large euhedral crystal of graphite (figure 2.5). This could be associated to a projection phenomenon because the crystal are all thin plates with random cuts through hexagonal plates characteristic of graphite.

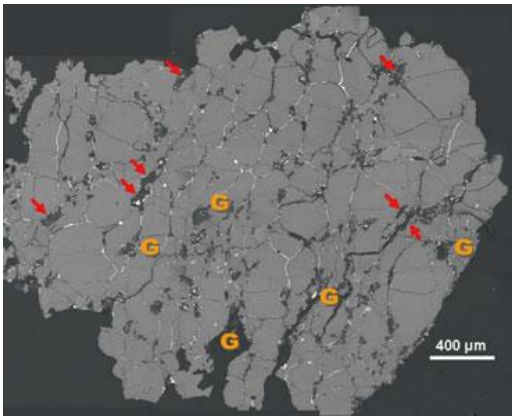

Figure 2.5 BSE image of a pyroxene-rich, low-porosity sample. The large black areas are carbon (principally graphite, labelled G), and euhedral graphite crystals are arrowed (Zolensky et al., 2010).

The validation of presence of euhedral-appearing graphite crystals in Alma is important, because such grains are usually found only in ureilites of very low shock degree (Goodrich, 1992; Mittlefehldt et al., 1998). This observation emphasizes the brecciated nature of *ASM*. The *ASM* mineralogy of pyroxene dominated compact lithology is summarized on Table 2.1.

Olivine is more abundant than pyroxene in the "Olivine dominated compact lithology". The olivine near to carbon phases usually displays the typical reverse zoning of ureilites. Pores and metal blebs are present, and the presence of these blebs was probably due to high-temperature reduction.

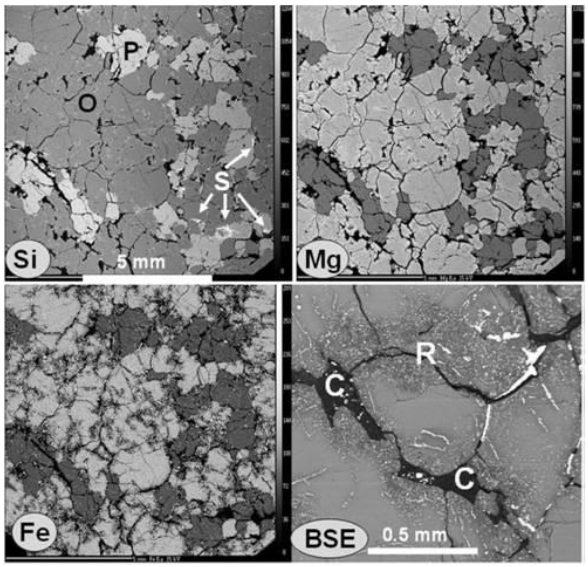

Figure 2.6 An olivine-dominated Alma lithology (Zolensky et al., 2010).

The *ASM* mineralogy of olivine dominated lithology is summarized on Table 2.1. The figure 2.6 shows an olivine dominated compact lithology, which shows three element maps, i.e. Si, Mg, and Fe, of an *ASM* ureilite fragment and one higher magnification BSE image. In these image "O" refers to olivine, "P" to pigeonite, silica is "S", carbon is "C" and reduced olivine plus metal is indicated "R". In the figure 2.6, the metal was segregated from olivine adjacent to carbon, probably during high-temperature smelting (Zolensky et al., 2010).

2.2.1 Textural aspect of ASM ureilites fragments

The investigation of textural aspects of *ASM* in several fragments suggested that *ASM* comprises a wealth of grain sizes, textures, and mineral compositions. The textural aspects of *ASM* fragments are very important to add more information about the evolutionary story of these fragments and they were subdivided as follows (Horstmann and Bischoff, 2014):

- **Coarse-grained ureilites:**

in these fragments both olivine-rich and pyroxene-rich ureilites were identified. Olivine-rich coarse-grained ureilites exhibit grain size up to more than a few millimetres, while pyroxene-rich coarse-grained ureilites present grain size minor of 1 mm. *ASM* coarse-grained ureilites are sometimes characterized by many little Fe-metal grains and often by reduction rims around olivine grains, as reported in the figure 2.7.

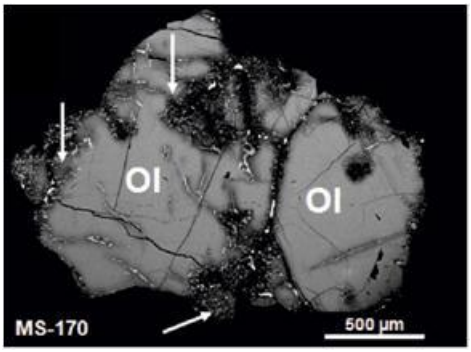

Figure 2.7 BSE images of coarse-grained ureilites, illustrating the reduction textures typical of ureilites, in detail olivine characterized by reduced (Horstmann and Bischoff, 2014).

❖ **Fine-grained ureilites:**

they are characterized by strongly recrystallized mineral assemblage for both olivine and pyroxene, and another important characteristic is the presence of an abundant porosity (figure 2.8). The textures of some of these rocks were described as granoblastic and mosaicized (Zolensky et al., 2010) with small grains of silicates. Pyroxene is usually present in interstitial zone between olivine euhedral grains.
In many fragments, rare zoning in olivine demonstrated larger-sized carbonaceous aggregates, with a high metal composition and high porosity (Jenniskens et al., 2009).

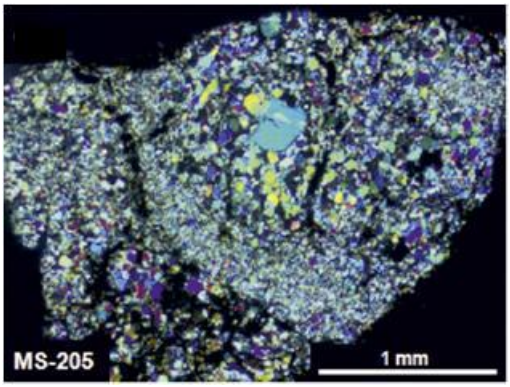

Figure 2.8 *ASM* fine-grained ureilites, as typical example of recrystallized fine-grained ureilites (Horstmann and Bischoff, 2014).

❖ **Dark ureilites and/or those with variable grain size:**

variable grain-sizes are present; some domains are fine-grained (<50μm), while some domains show larger crystals (>700μm). The fragments with these differences in grain-sizes are often classified as *breccias*.

❖ **Ureilitic metal-sulphide assemblages:**

sulphide metal assemblages with any fine-grained ureilites material are present, and the abundance of rounded metal grains, with micrometric sizes, embedded in large mass of FeS is found (Bischoff et al., 2010). The metal grains exhibit Ni zoning, with usually low-Ni core, surrounded by Ni-rich rim (figure 2.9).

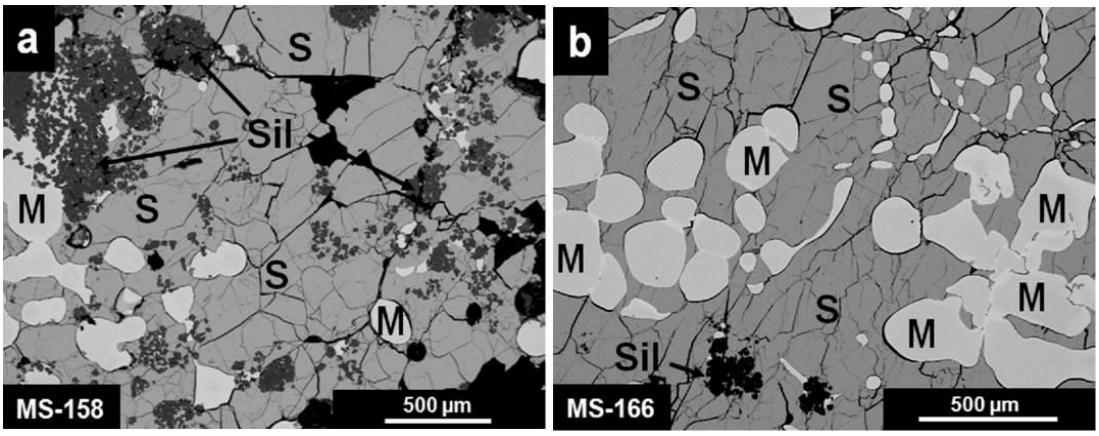

Figure 2.9 Two examples of *ASM* sulphide-metal assemblages in BSE images. In the figure silica is "S" and metal grains is "M" (Horstmann and Bischoff, 2014).

❖ **Ureilite-related andesite:**

based on its texture, the meteorite is comparable to basalt, but bulk chemistry revealed that it is an andesite; it was firstly considered as a doubtful meteorite specimen. This type of ureilites is abundant in feldspar and pyroxene, but also metal grains are present, and they are usually Ni-free (figure 2.10).

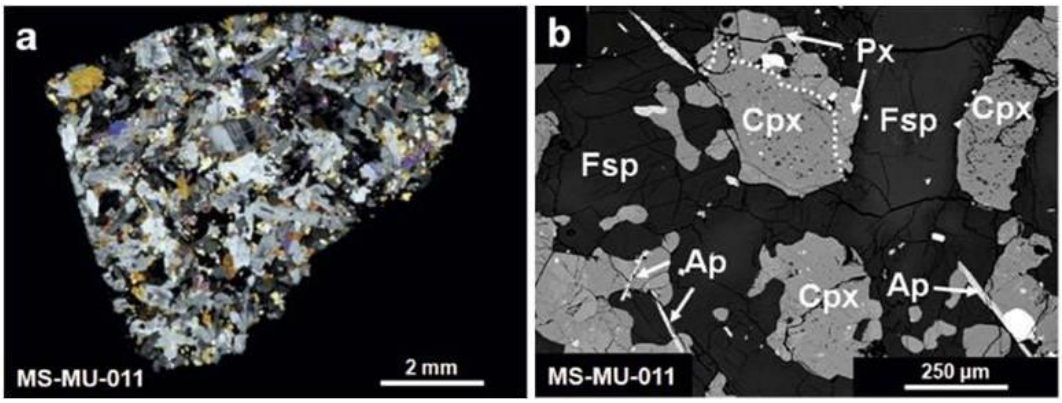

Figure 2.10 ASM andesite.
(a) Optical photomicrograph of a thin section with crossed polarizer.
(b) BSE image showing details of the typical texture of this type of ureilites (Horstmann and Bischoff, 2014).

2.3 Chondritic fragments

Some chondrites are also present among fragments of *ASM*.

Chondrites are the oldest and most primitive rocks of the Solar System. These rocks are *cosmic sediments* that predominantly consist of chondrules, refractory objects (calcium-aluminium-rich inclusions (CAIs) and olivine aggregates, Fe-Ni metal and fine-grained matrix (Rossi, 2018). The division of chondrites are into three major classes, *carbonaceous chondrites (C)*, *ordinary chondrites (O)* and *enstatite chondrites (E)*, as reported in figure 2.11.

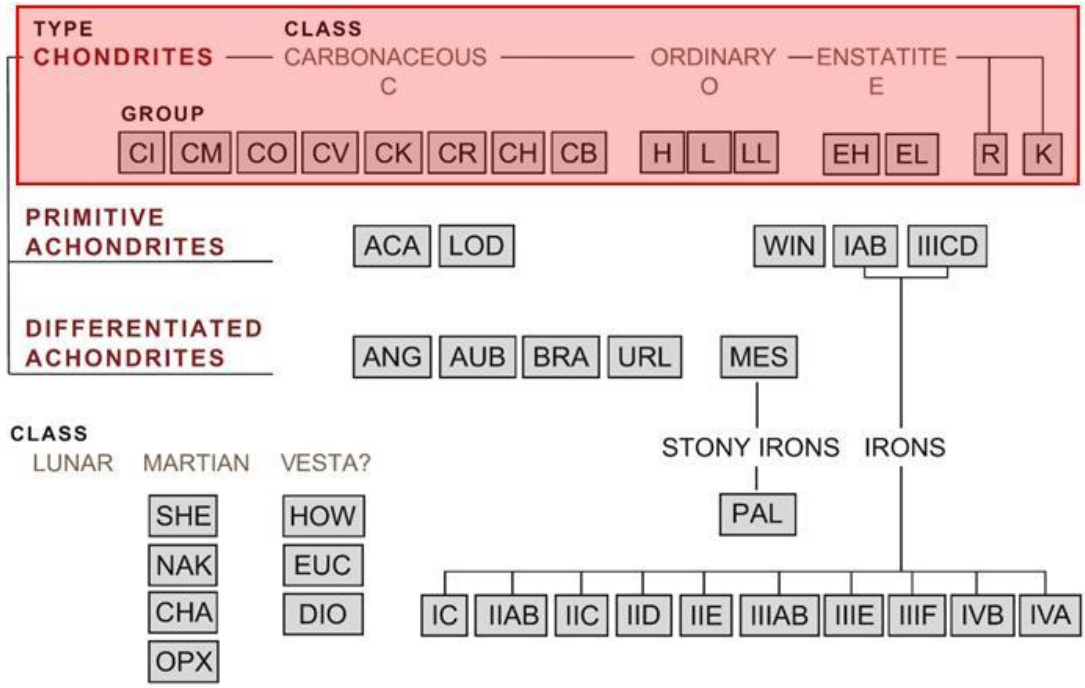

Figure 2.11 Classification of meteorites. ACA acapulcoites, *LOD* lodranite, *WIN* winonaites, *ANG* angrites, *AUB* aubrites, *MES* mesosiderites, *BRA* brachinites, *URE* ureilites, *SHE* shergottites, *NAK* nakhlites, *CHA* chassignites, *OPX* orthopyroxenite, *HOW* howardites, *EUC* eucrites, *DIO* diogenites, *PAL* pallasites
(Rossi, 2018).

The chondrites classes identified in *ASM* four different categories (Horstmann and Bischoff, 2014):

- E*nstatite chondrites* (Bischoff et al., 2010) are characterised by different textures of their silicate and especially their metal constituent, which there are present as nodules (figure 2.12);

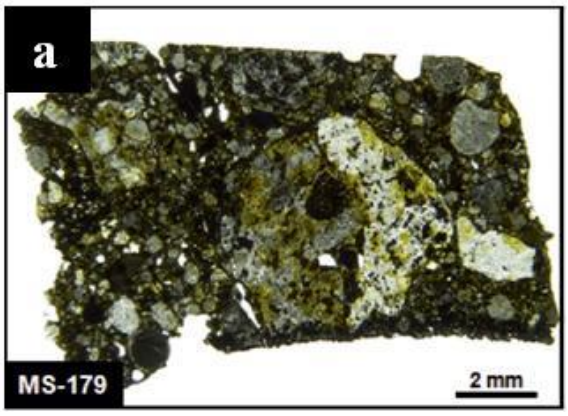

Figure 2.12 Optical photomicrograph of one MS-179 thin section illustrating the various lithologies/fragments in this rock (Horstmann and Bischoff, 2014).

- *Ordinary chondrites*, several fragments of them are found among *ASM* strewn field. Some authors (Bischoff et al., 2010) considered that ordinary chondrites might to be unrelated to *ASM*. A particularity of this type of chondrite is the presence of a shock melted area. In the figure 2.13 is showed an example of *ASM* ordinary chondrites.

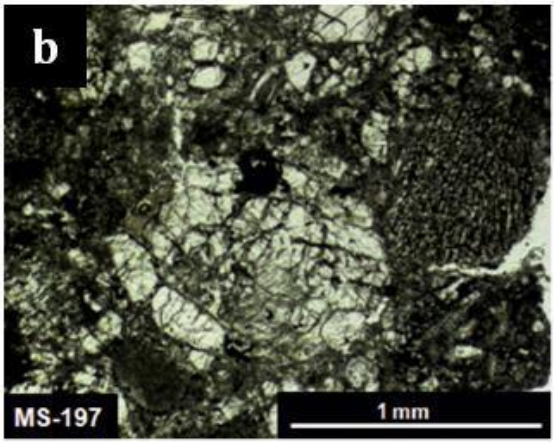

Figure 2.13 Almahata Sitta ordinary chondrites (Horstmann and Bischoff, 2014).

- *Rumuruty-like chondrite fragments*. Only one piece of this type of meteorite was found among *ASM* chondritic fragments. This is characterized by altered spinel-rich Ca-Al rich inclusions (figure 2.14);

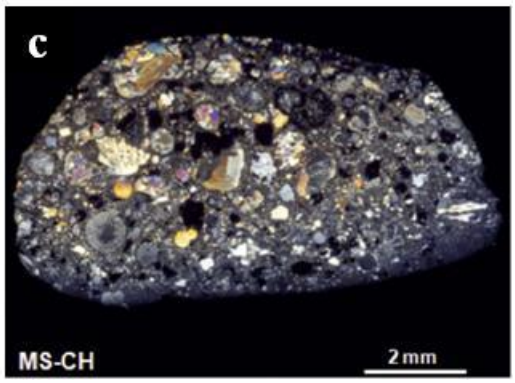

Figure 2.14 Unique Rumuruti-like chondrite MS-CH showing abundant chondrules and high matrix abundance (~45 vol%) (Horstmann and Bischoff, 2014).

- *Carbonaceous chondrite*, which presents chondrule silicate whit different textural type (figure 2.15);

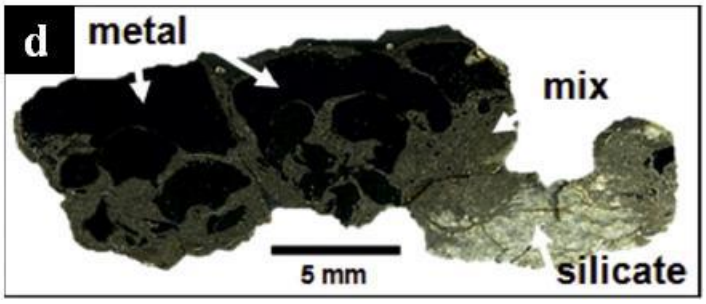

Figure 2.15 Carbonaceous chondrite fragment show silicates in complex intergrowths with smaller metal grains (Horstmann and Bischoff, 2014).

Chapter III

Carbon phases in ASM

3 CARBON PHASES IN ALMAHATA SITTA METEORITE

Several carbon compounds are contained in *ASM* ureilites samples. In detail, they include diamond, lonsdaleite, graphite and other graphitic compounds. Lonsdaleite was initially defined as a higher-pressure hexagonal polymorph of diamond but now it is considered like a defect diamond (Nemeth et al., 2014).
The main aim of this Master thesis is to identify and characterize the carbon phases in *ASM* fragments. The investigation of diamond and graphite in *ASM* can help to ultimately unravel the geological processes behind their crystallization and to recovery information about the moment of their crystallization, during the evolutionary story of asteroid 2008TC_3.

3.1 Diamonds from Almahata Sitta meteorite

Diamonds are present in many ureilites fragments from *ASM*, but the origin of diamond in ureilites is still unclear and largely debated.

At the moment, three major hypotheses were formulated by the scientific community about origins of diamonds in ureilites. The first hypothesis for *ASM* is that diamond and graphite are intimately related to shock levels recorded in olivine and this would suggest that diamonds were formed from graphite by shock. A second contrasting hypothesis, based on the report of one large diamond crystal (i.e. above 0.04 mm crystal size), excludes the origin from shock impact and assumes that diamonds in *ASM* were formed under high static pressure conditions in the deep interior of the ureilites parent body (UPB), similar to Earth's mantle diamonds. Finally, the third hypothesis suggests the formation of diamonds by chemical vapor deposition (CVD) prior to accretion of UPB (Fukunaga et al., 1987)**.**

One of the main questions about ureilites is why they contain large amount of noble gasses concentrated in carbon veins: diamond is shown to be one of the noble

gas carriers, while graphite is usually gas-free. An answer to this question is proposed by the formation of diamonds by chemical vapour deposition.

In typical chemical vapour deposition (CVD), the substrate is exposed to one or more volatility chemistry precursors, which react and/or decompose on the substrate surface to produce the desired deposit. Frequently, volatile by-products are also produced.

Fukunaga et al. (1987) synthesized diamonds by CVD from gaseous mixture of H_2 and CH_4 including Argon (Ar) using experimental apparatus shown in the figure 3.1. Ar entrapped in diamond was examined by mass spectrometry to compare the results with data obtained by ureilites samples. The comparison showed many differences between content of Ar in diamond and in graphite. This was consistent with the observations of Göbel et al. (1978), where graphite was excluded as a carrier of noble gases in ureilites. Few years later, a further hypothesis was proposed about the CVD formation of diamonds in ureilites, stating that diamond with noble gas content was probably formed from the solar nebula (Fukunaga et al., 1987).

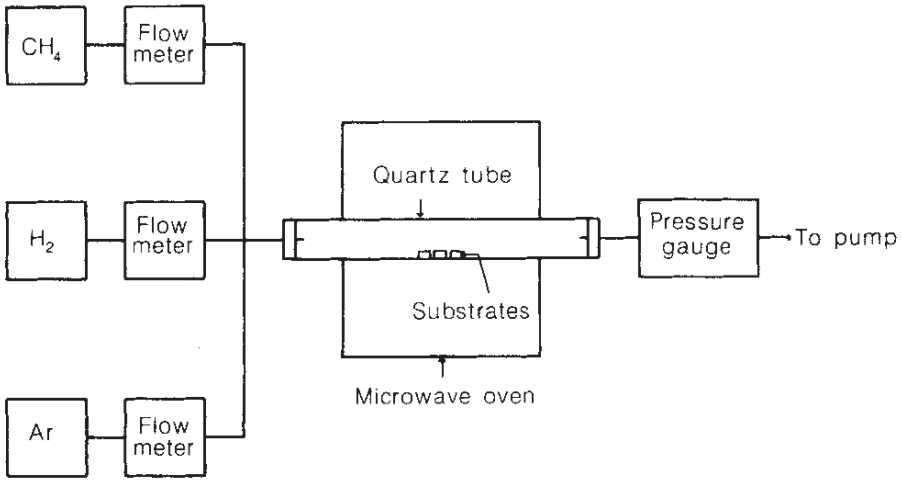

Figure 3.1 Schematic diagram of the experimental apparatus of diamonds synthesis by CVD (Fukunaga et al., 1987).

Another interpretation about the presence of noble gases content in diamonds was proposed by Lewis et al. (1987), suggesting the primary formation of diamond by stellar condensation, based on study of many ureilitic samples of Allende, Murchison and Indarch meteorites.

The second hypothesis proposed that diamonds formation in ureilites took place under static high-pressure conditions in the deep interior of a ureilite parent body (UPB) similar to Earth's mantle diamonds. This hypothesis was proposed for the first time by Urey et al. (1956), investigating diamonds samples collected in the Canyon Diablo meteorite, which are collected in Arizona in the crater of the same name. The authors affirmed that diamonds cannot be produced except under fairly high temperature and high pressure. Using thermodynamic data and the density of graphite (2.26 gcm^{-3}) and diamond (3.51 gcm^{-3}), they understood that the required minimum pressure at 1000 K and 1200 K are at 31,000 and 37,000 bars, respectively. This huge pressure can explain the formation of these objects in the deep interior of a big parent body, with dimension similar approximately to Lunar mass or greater (Urey, 1956).

These approaches were also proposed for many ureilites samples of *ASM*. Some individual fragments of *ASM* diamond have similar crystallographic orientation, suggesting that the adjacent diamond segments were originally a single crystal (Miyahara et al., 2015). Large diamond assemblages occur besides such individual diamond grains, and one of this big diamond assemblages (about 100 μm in size) has the equal crystallographic orientation. These fragments can previously be a part of unique single diamond, suggesting the possible presence of large single-crystals diamond in the asteroid. The hypothesis of *ASM* diamond formation, suggested by Miyahara et al. (2015), was the partial melted magma or a C–O–H fluid in the deep interior of the ureilite parent-body or, alternatively, through a chemical vapour deposition (CVD) process in the solar nebula.

A section of the *AS* ureilite was investigated using transmission electron microscopy, hypothesizing that large diamonds were formed at high pressure inside the parent body (Nabiei et al., 2018). Nabiei et al. (2018) found many chromites, phosphates, and (Fe,Ni) sulphide inclusions embedded in diamond, and the authors reported that the composition and morphology of these inclusions can be only explained if the formation pressure was higher than 20 GPa. The pressures suggested that the size of ureilite parent body was even of Mercury or Mars dimensions.

Two different types of diamonds in *ASM* ureilites were found: multigrain diamond, which results from shock events producing clusters of nanometric sized individual diamonds, and large diamonds (up to 100 μm in diameter) grow at high-static pressure inside the UPB.

Another investigation about diamonds in ureilites of Canyon Diablo showed a pronounced similar crystallographic orientation among diamond fragments (Lipschutz, 1964). These authors proposed the formation of diamond in ureilites as product from graphite after a shock event.

Some experiments on meteoritic fragments of ureilites and in particular on diamonds were carried out using X-ray diffraction and Raman spectroscopy (Nakamuta et al., 2016). The properties of diamond and graphite revealed a high correlation with shock levels recorded in olivine, based on the classification of Stöffler et al. (1991). The data resulted from these experiments suggested that diamond in ureilites can be formed from graphite by shock.

The problem of noble gas content in diamond, graphite and silicates in ureilites are difficult to be interpreted by the shock model but Matsuda et al. (1995) showed that considerable amount of noble gases are trapped in the shock-produced diamond, when starting material are in a close system. This was carried out during many experiments conducted by Matsuda et al. (1995), demonstrating a possible interpretation of noble gas content in diamond using the shock model. This supports the explanation of diamond formation through shock events from graphite compounds.

3.2 *Lonsdaleite from Almahata Sitta meteorite*

Since 1967, year of its discover, lonsdaleite was considered a hexagonal polymorph of diamond (Frondel and Marvin, 1967), while nowadays it is not identified as a real different phase but preferably like a diamond defect (Nemeth et al., 2014). The figure 3.2 shows a crystal structure projection along hexagonal axis for cubic diamond, hexagonal diamond and finally for stacking disordered diamond.

These defects give rise to nanometre-scale structural complexity, and the study about the existence of lonsdaleite is important for re-evaluating the interpretations of many lonsdaleite-related studies and phenomena (Nemeth et al., 2014).

An electron microscopy study has demonstrated that so-called hexagonal diamond samples are not really discrete materials but faulted and twinned cubic diamond (Salzmann et al., 2015).

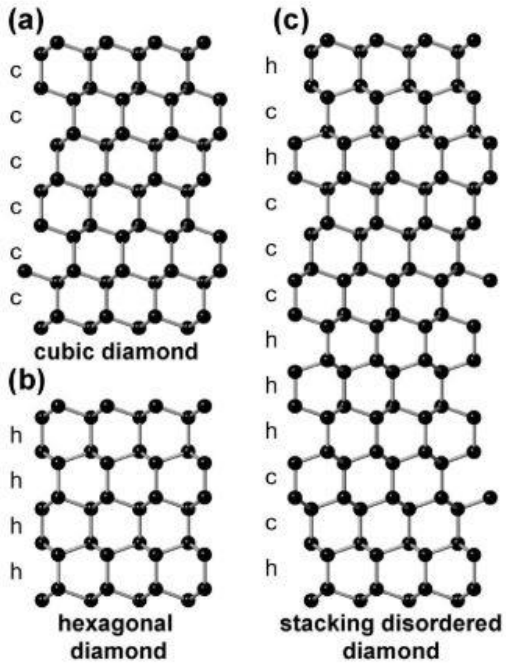

Figure 3.2 Projections of crystal structure along the hexagonal a axis for (a) cubic diamond, (b) hexagonal diamond and (c) stacking disordered diamond (Salzmann et al., 2015).

A quantitative analysis of cubic and hexagonal stacking in diamond samples was performed using X-ray diffraction by Salzmann et al. (2015), by processing these data with the DIFFaX software package (figure 3.3).

The highest fraction of hexagonal stacking in materials was previously referred to a hexagonal diamond and it was below 60%. The remnants of the stacking are cubic. Cubic and hexagonal sequences are interlaced in a complex way. Lonsdaleite is not associated to a simple physical mixture of cubic and hexagonal diamond but it is better structurally described as stacking disordered diamond.

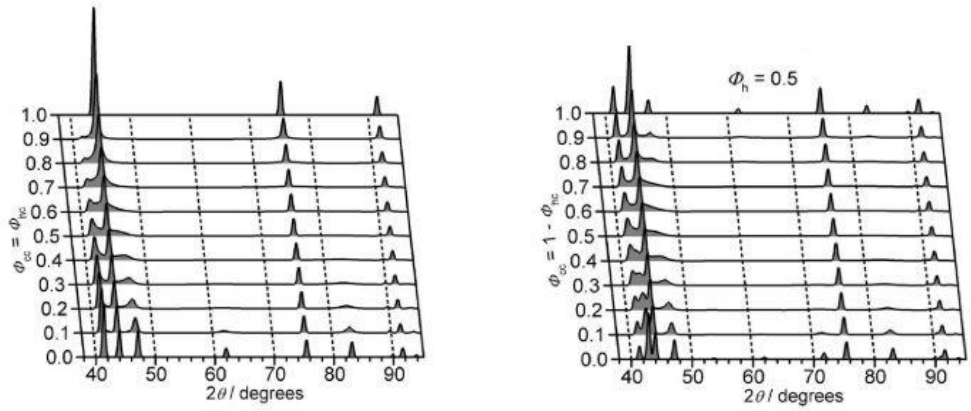

Figure 3.3 Calculated powder diffraction patterns (Cu Kα) along the random stacking as well as the 0.5 hexagonality line (Salzmann et al., 2015).

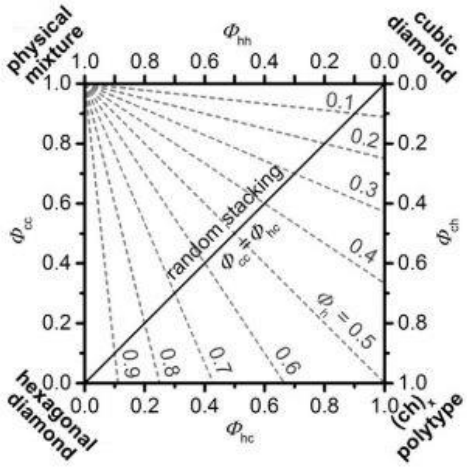

.

Figure 3.4 Example of stackogram used for the structural description of stacking disorder (Salzmann et al., 2015).

The figure 3.4 indicates a stackogram, which describes the structural stacking disorder in diamond (Salzmann et al., 2015). The random stacking is indicated by right black line, whereas the structure with a constant hexagonality is expressed by dashed line.

Lonsdaleite is usually used as a marker of asteroid impacts because it plays a central role during the graphite-to-diamond transformation and it has never been produced or described as a separate, pure material (Nemeth et al., 2014).

3.3 Graphite and graphitic compounds from Almahata Sitta meteorite

Graphite is most abundant carbon phases in the ureilites samples of *ASM*, and its presence is marked in the figures 3.5a and 3.5b with "G". It is located among interstitial silicates, which also contain fine-grained troilite, kamacite, silicon and phosphorous. In graphite beds, diamonds are generally in ureilites samples.

Fe-Ni metals are usually present in ureilites, and in all *ASM* ureilitic samples. They are generally the largest masses close to carbon phase, as reported with white colour in the figures 3.5a and 3.5b.

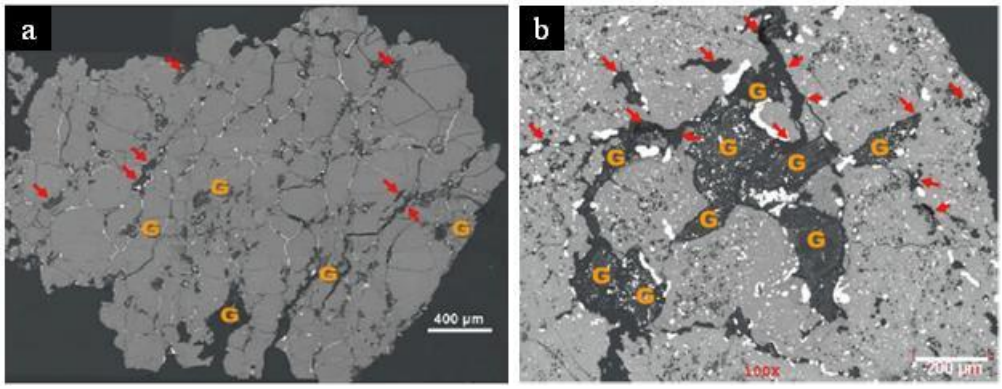

Figure 3.5 BSE images of ASM ureilites fragments, the large black areas are graphite and graphite compounds (Zolensky et al., 2010).

The identification of graphite beds in the *ASM* samples is a very important step to better understand the formation of diamond and therefore to comprehend any correlation between graphite and diamond crystallization.

This Master thesis is usually conducted using a preliminary analysis by Optical Microscopy and then a deeper analysis by Secondary Electron Microscopy (SEM) to detect right the graphite beds.

Graphite is also the main phase analysed by Micro-Raman spectroscopy with the purpose to understand the ureilitic parent body temperature (T_{max}) and the

crystalline size of graphite in *ASM* samples to try to insert *ASM* in a geological contest.

Interesting and important papers about studies of graphite phases through Raman Spectroscopy were conduct by Ferrari and Robertson (2000) and Visser et al. (2018) and in particular a study on graphite phase through Raman Spectroscopy of Almahata Sitta ureilites was proposed by Ross et al. (2011).

3.4 Shock and Foliation

To understand *ASM* ureilites crystallization, the evaluation of possible shock phenomena in carbon phases is very crucial. Some ureilites show mosaicized olivine and deformed pigeonite, suggesting a possible formation by shock at high temperature, possibly related to the breakup of the ureilite parent body or its reassembly. Several fragments of *ASM* have been associated to suffer from shock metamorphism and possibly some melting (Zolensky et al., 2010). The absence of orthopyroxene in *ASM* ureilites indicates that the probably pyroxene equilibration temperature was higher than 1300°C (Takeda et al., 1989).

The determination of the shock level in ureilites was proposed by Stöffler et al. (1991). He proposed six stages of shock, based on shock effects in olivine and plagioclase which probably had been correlated whit level of shock in diamond and carbon phases (Nakamuta et al., 2016). The characteristic shock effect was observed by thin section microscopy and consist of:

- **S1**-sharp optical extinction;
- **S2**-undulatory extinction of olivine;
- **S3**-planar features in olivine;
- **S4**-mosaicism in olivine;
- **S5**-isotropization of plagioclase and planar deformation features in olivine;
- **S6**-recrystallization of olivine;

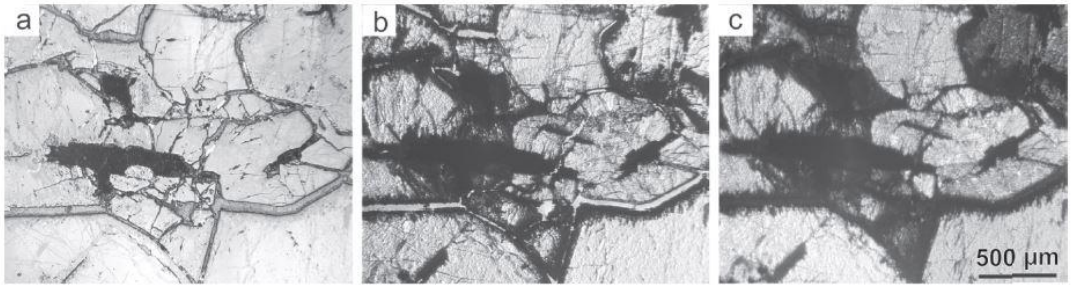

Figure 3.6 Optical microscope image of ureilites of representative low-shock features (Nakamuta et al., 2016).

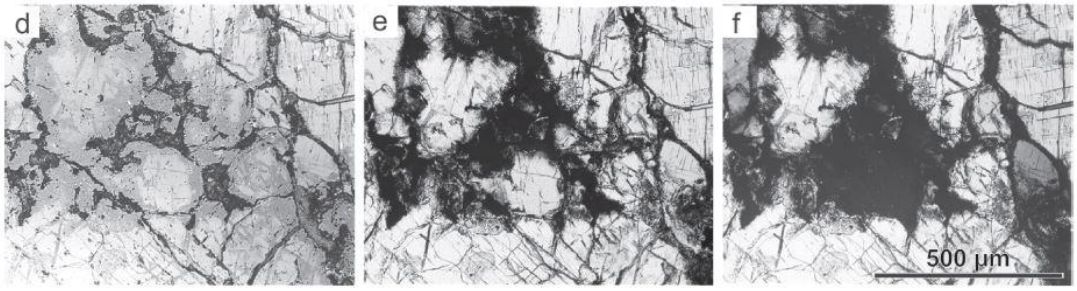

Figure 3.7 Optical microscope image of ureilites of representative moderate-shock features (Nakamuta et al., 2016).

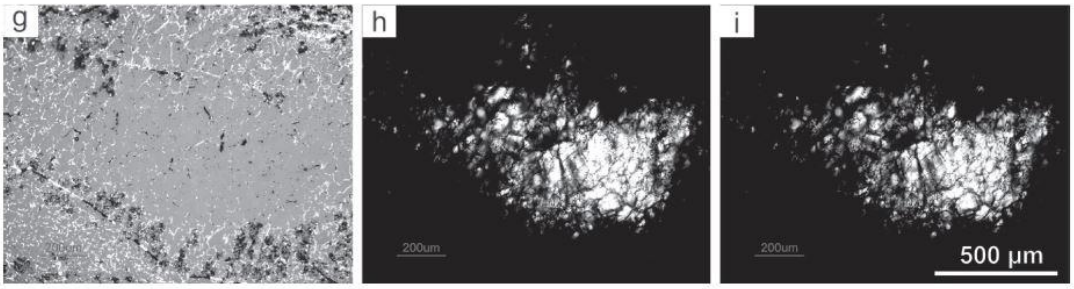

Figure 3.8 Optical microscope image of ureilites of representative high-shock features (Nakamuta et al., 2016).

Several thin microscopy sections of ureilite samples are necessary to assign the shock level through Stöffler method. Nakamuta et al. (2016) determined the shock stage of ureilites defining the shock level of olivine.

The optical microscope image in the figures 3.8 shows varying features of shock in ureilites reported by Nakamuta et al. (2016), sharing different levels in low-shock feature, moderate-shock feature and high-shock feature.

However, we were not able to carry out any optical microscopy observation due to the pervasive presence of diamonds, which prevented any thin section polishing due to the extreme hardness of diamond.

In this Master thesis, another method was adopted to determine the shock level of our samples: a multimethodological approach by Scanning Electron Microscopy (SEM), Micro-Raman Spectroscopy and finally by Micro-RX Diffraction (used to determine crystallite size of the samples), was proposed. The determination of the shock level in the fragments is an important parameter to understand the causes of diamonds formation.

Chapter IV

Methods

4 METHODS

4.1 *Samples*

The samples examined during Master thesis consist in three ureilites fragments of ASM, labelled as AHS_209B, AHS_72 and A135A. The first step of the analysis was to detect the graphite beds in the fragments, in order to collect the diamonds probably present in these sites and the graphite phase.

Detection of graphite beds was realized through Scanning Electron Microscopy (SEM) analysis, and the samples was prepared embed in epoxy. The figure 4.1 shows the optical microscope image of the samples A135A in a characteristic tablet of epoxy, in preparation for SEM analysis.

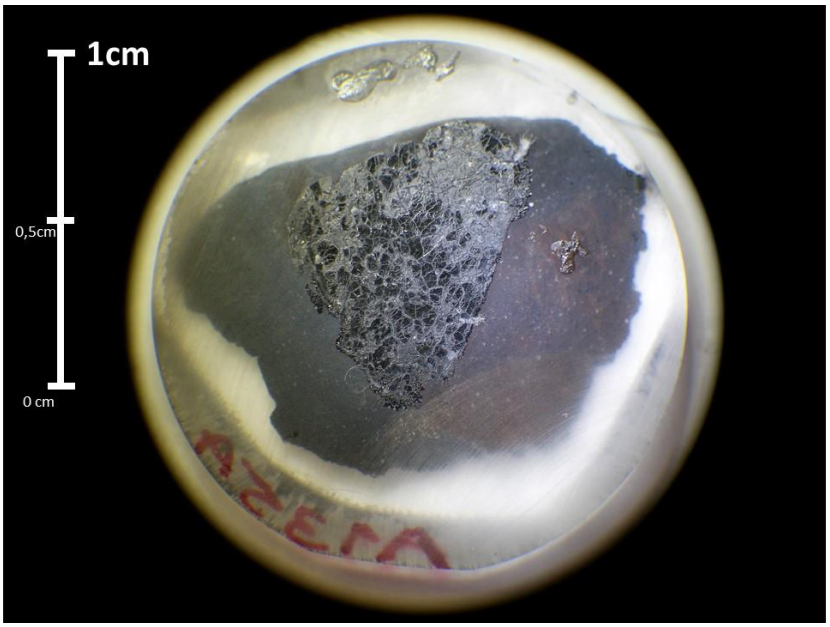

Figure 4.1 Optical image by Nikon smz645 of the A135A ureilites samples, tablet of epoxy.

To avoid the samples cut with a diamond's saw, a plausible contamination source, the samples were scratched on the surface of epoxy samples with an abrasive grinding paper of silicon carbide.

When graphite beds are detected on various fragments, the collection of diamonds occurred. This delicate operation is carried out using a needle, which we rubbed the zones identified as graphite beds. Suddenly, with a little fraction of glue, the materials obtain through this procedure are attached at the top of 100 μm diameter

vitreous capillary. The figures 4.2-4.4 report the images on optical microscopy, in reflection mode, with 10x objective of the samples collected on the surface of the three *ASM* fragments; in the figures are even possible recognized the diamonds aggregates.

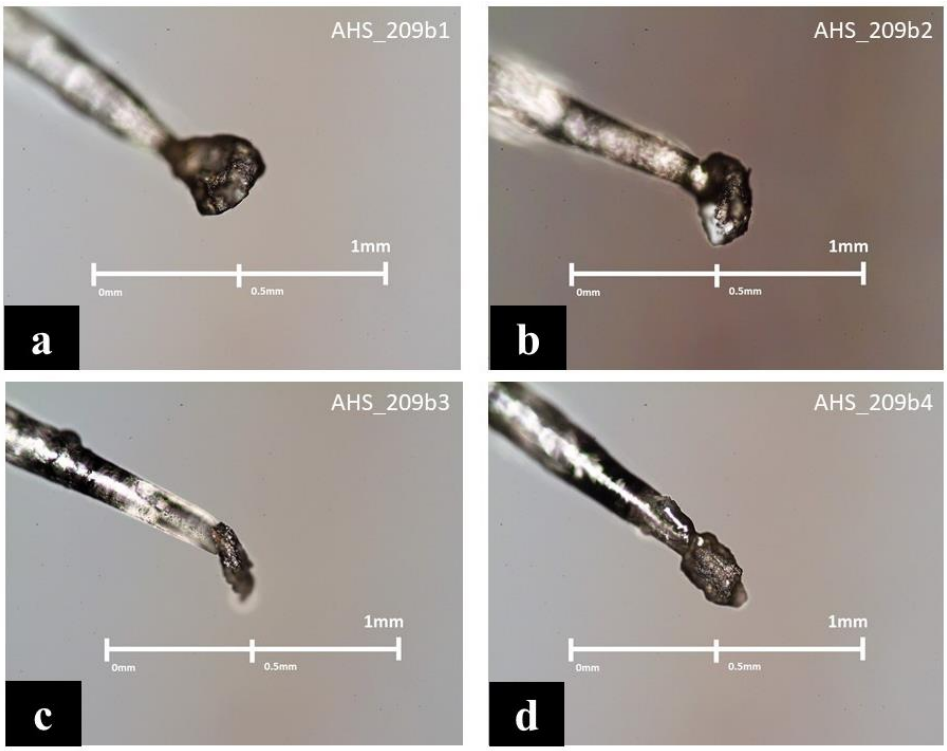

Figure 4.2 Optical microscopy images 10x (reflection mode) by Nikon eclipse ME600 of AHS_209b (b1, b2, b3, b4) ureilites sample of ASM attached on the top of 100 μm vitreous capillary.

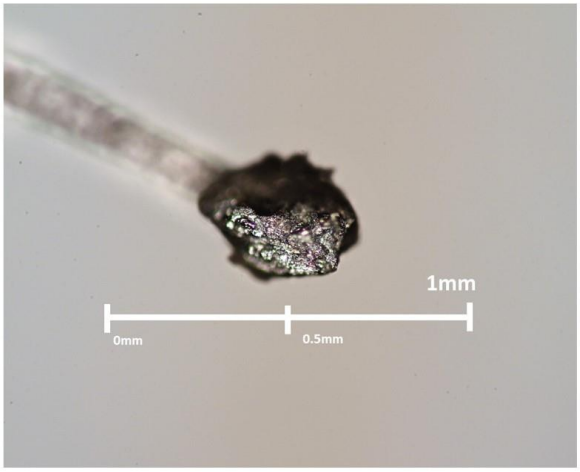

Figure 4.3 Optical microscopy images10x (reflection mode) by Nikon eclipse ME600of AHS_72 ureilite sample of ASM attached on the top of 100 μm vitreous capillary.

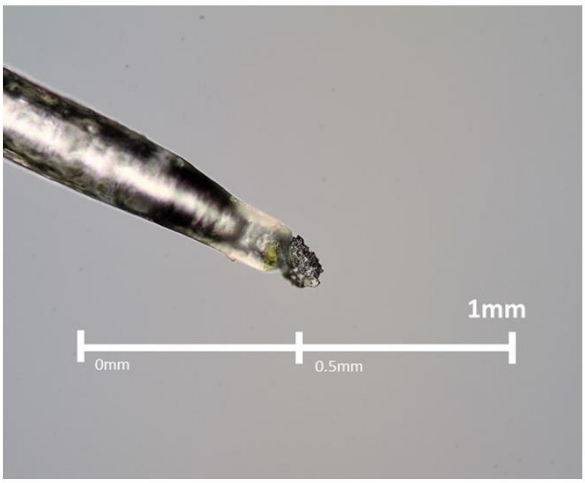

Figure 4.4 Optical microscopy 10x (reflection mode) images by Nikon eclipse ME600 of A135A ureilite sample of ASM attached on the top of 100 μm vitreous capillary.

The portions of samples attached on vitreous capillaries were confirmed to contain the diamond phase (through XR analysis); capillaries were utilized for micro-Raman microscopy analysis at Department of Chemical Sciences (University of Padua) and Micro XR Powder diffraction analysis at Paul Scherrer Institute (Switzerland).

4.2 *Scanning Electron Microscopy (SEM)*

The Scanning Electron Microscopy was conducted on *ASM* samples to identify the graphite beds and the diamond phase.

Scanning Electron Microscopy (SEM) is a determinate type of electron microscopy, which produces images of samples by surface scanning utilizing a focused beam of electrons. A focused electron beam (2-10 keV) scans on the surface, and several types of signals are produced and detected as a function of position on the surface. Various signals are product and they contain several information about the surface topography and composition of the sample. The space resolution can be as high as 1 nm.

In this Master thesis analyses, signals of Secondary electrons were used to obtain surface texture information, while backscattered electrons were applied to acquire surface structure and average elemental information. Through SEM, X-ray and Auger electrons signals were possible also collected, for information about elemental composition (with different thickness-sensitivity).

The figure 4.5 shows the different signals produced when an electron beam impacted on a surface.

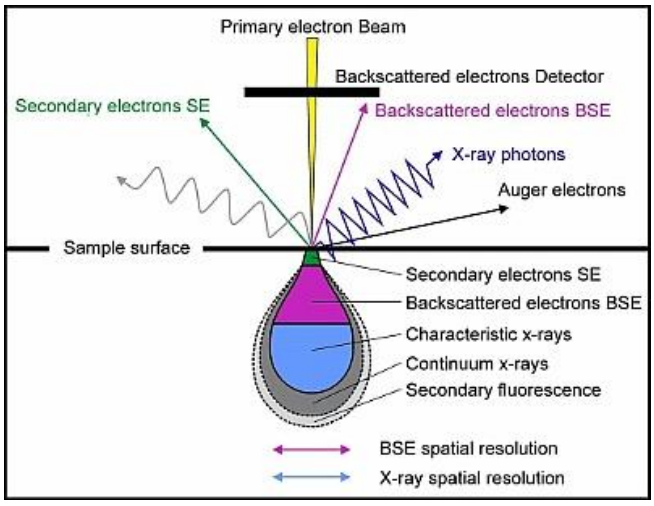

Figure 4.5 Scheme of several signal produced by Scanning Electron Microscopy when electron beam invested the surface.

- Secondary electrons (SE) give mainly information about topography. SE are low energy electrons (10-50 eV) and they are generated from the collision between the incoming electrons and the loosely bonded outer electrons (figure 4.5). The number of SE is greater than the number of incoming electrons. SE give information with high resolution and surface signal depend on curvature surface;

- Backscattered electrons (BSE) give also information about chemistry. BSE derived by a fraction of the incident electrons, which is retarded by the electro-magnetic field of the nucleus of the atoms and, if scattering angle is greater than 180°, the electron can escape from the surface. BSE are considered as high energy electrons and "bulk" signal depend on atomic number of the component of the samples analysed (figure 4.5).

Scanning electron microscopy utilized during the analysis of the *ASM* samples is located at CEASC of University of Padua. The instrument model is JSM Jeol 6490 , and it is also connected with XR fluorescence microanalysis (figure 4.6).

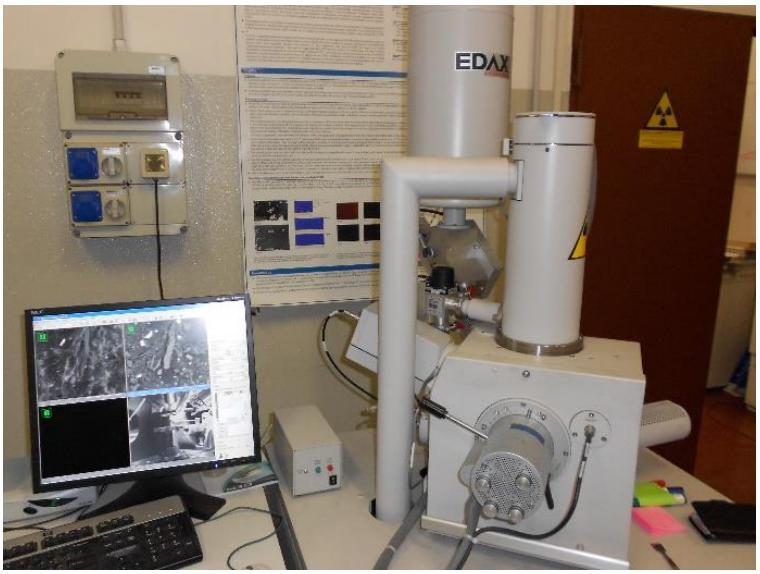

Figure 4.6 Scanning Electron Microscope of CEASC of University of Padua.

4.3 *Micro-Raman Spectroscopy (MRS)*

Micro-Raman spectroscopy (MRS) is necessary to obtain peak temperature estimations, which is important to evaluate the process of crystallization occurred on different carbon phases.

Raman spectroscopy is a spectroscopic technique used to observe vibrational, rotational, and other low-frequency modes in a system. It depends on inelastic scattering, or Raman scattering, of monochromatic light, usually from a laser in the visible, near infrared, or near ultraviolet ranges. The laser light interacts with molecular vibrations, phonons or other excitations in the system, resulting in the energy of the laser photons being shifted up or down. The shift in energy gives information about the vibrational modes in the system.

Vibrational frequencies are characteristic of chemical bonds or groups of bonds in a specific molecule and shift of vibrational frequencies are sensitive to local environment of a molecule, such as crystal phase, local strain, and degree of crystallinity. A Raman spectrum provides a "fingerprint" representing the set of bonds present in the material (figure 4.7).

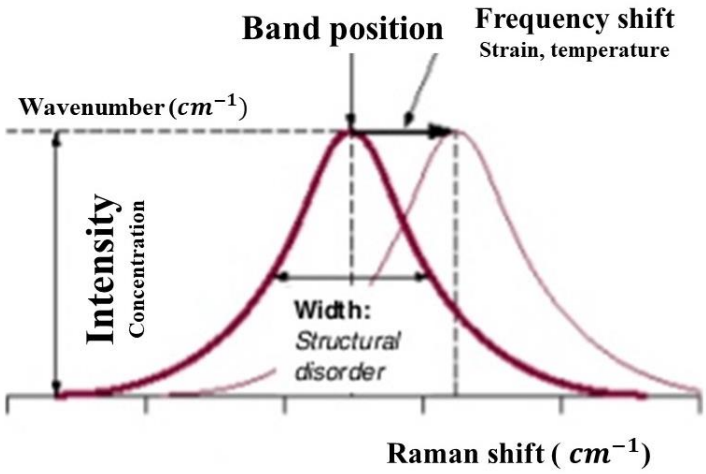

Figure 4.7 An example of Raman peak, where are indicated the intensity, band position, frequency shift and width of the spectra.

MRS was applied on the samples extracted from graphite beds from AHS_209B, AHS_72 and A135A, which were previously attached on the top of vitreous capillaries of 100 μm. During the analyses several spectra of graphite phases were collected.

The MRS analysis was conducted using an inVia Renishaw micro-Raman spectrometer (figure 4.8), with excitations laser capacity at 488, 633 and 780 nm at Department of Chemical Sciences of Padua University.
On ureilites samples, several punctual micro-Raman analyses are obtained with a laser excitation of 514 nm and with a laser operating power of 1.9 mW.

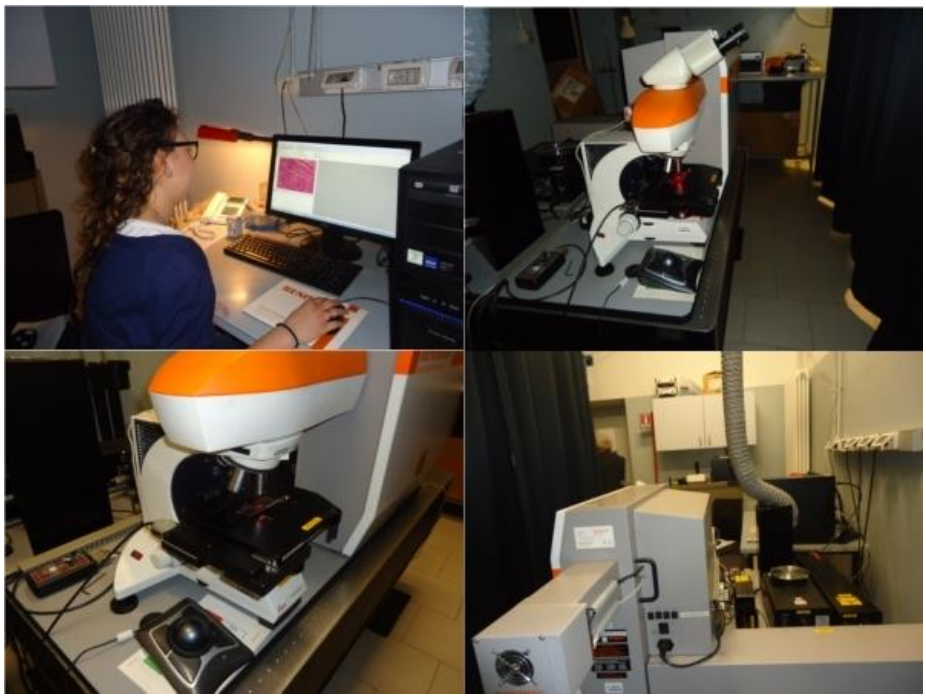

Figure 4.8 inVia Renishaw micro-Raman spectrometer at Department of Chemical Sciences of University of Padua.

4.4 *Micro-Powder XR Diffraction at Paul Scherrer Institute (PSI)*

The Micro-XR Powder diffraction analyses were performed at Paul Scherrer Institute (PSI) in Switzerland. PSI is the largest research institute for natural and engineering sciences in Switzerland and it shows characteristic shape of a doughnut with an outer diameter of 138 m, an inner diameter of 32 m and a height of 14 m (figure 4.9).

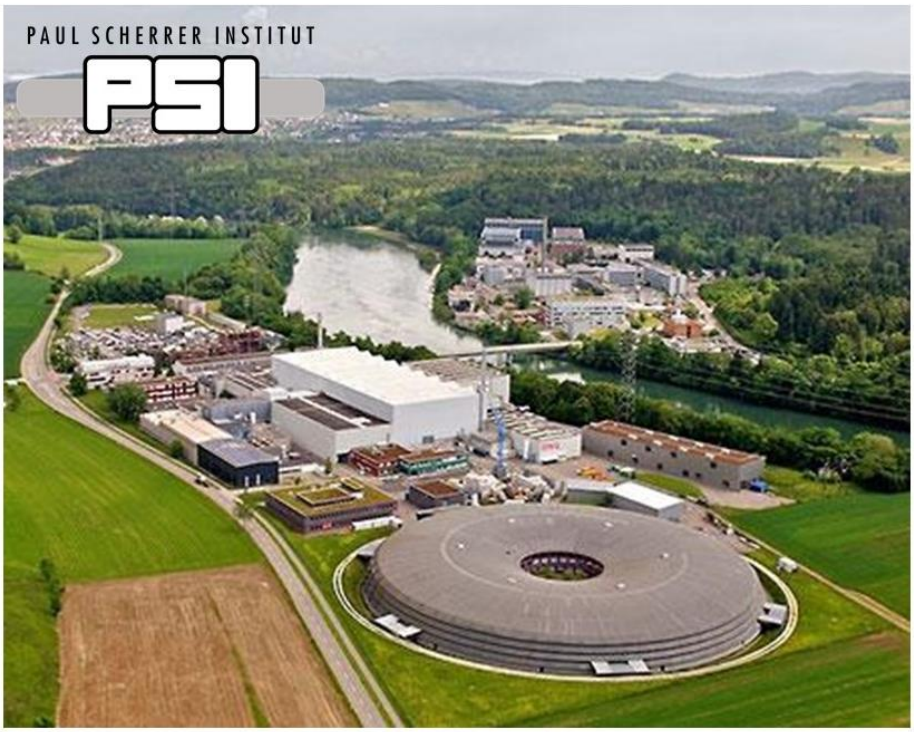

Figures 4.9 Paul Scherrer Institute at Villigen (Switzerland).

At PSI sixteen beamlines are in user operation, depending on the type of radiation source used: each beamline at Swiss Light Source (SLS) is optimised for a precise technique. To acquire Synchrotron Light, electrons have to be accelerated to near light speed, inside an electron accelerator, and then magnetic fields force the flying electrons into a circular orbit.

Synchrotron Light Source become efficient arranging many magnets into a storage ring, where the high energy electrons can circulate for hours. In a so called undulator one has a periodic array of magnets with alternating polarity of the

magnetic field. This forces the electrons into a slalom course. This in turn concentrates the synchrotron light into discrete wavelength, a brilliant light beam, and this produces an intense synchrotron light beams, which are sharply focused like a laser beam.

A beamline guides the synchrotron light (X-rays), which is produced by the circulating electrons, to the experimental stations. Beamline consists of several parts, as follows:

- **the source**, which is either an undulator, a wiggler or a bending magnet. The most common source in a modern synchrotron light source is the undulator;
- **the front end**, which contains slits, beam windows, beam shutter and beam stopper;
- **mirrors,** which deflect and focus the X-rays onto the experimental sample and that have a filters function to cut away the unwanted part of SL spectrum;
- **conventional lenses,** which are used as well polished, high precision mirrors, such as copper plates or crystals (like silicon);
- **the monochromator,** which selects a single wavelength with high resolution;
- **the experimental station**, which consists on sample holder and a detector equipment, which registers the X-ray signals.

The samples AHS_209B (B1, B2, B3, B4), AHS_72 and A135A were analysed through MS-X04SA beam line (figure 4.10). The MS beamline is powered by a short-period (14 mm) in-vacuum, cryogenically cooled, permanent-magnet undulator, (CPMU, U14), while the front end and optics are designed to optimally exploit the characteristics of the U14 source. Characteristic of MS-X04SA beam line are reported in Tab. 4.1.

Power X-Ray Diffraction experiments allowed to obtain qualitative and quantitative information about diamond and graphite phases in the samples. The main purpose

of these experiments was used the diffractometers obtained through line profile analysis to understand the crystallite size of the diamonds through a consecutive data processing.

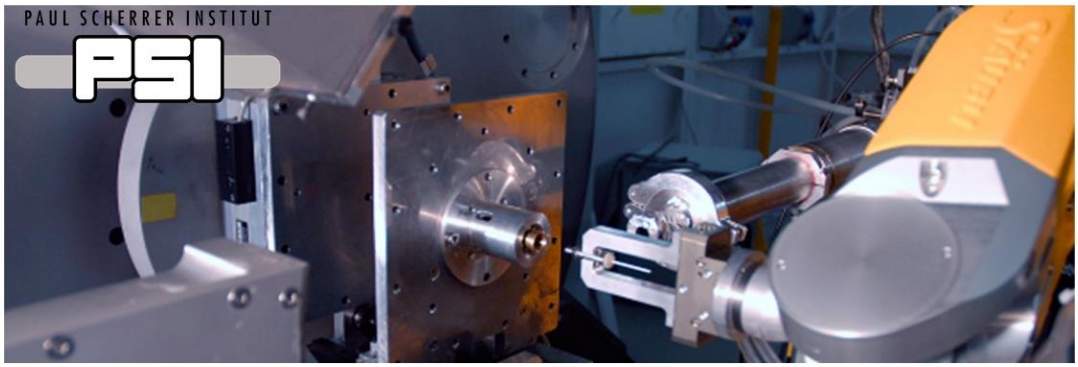

Figure 4.10 MS-X04SA beam line Swiss Light Source (SLS).

Powder diffraction was performed in Experimental Hutch 1 (EH1), where scientific responsible are Nicola Casati and Antonio Cervellino. The utilised MS Powder diffractometer works in Debye-Scherrer geometry and is equipped with a unique solid-state silicon microstrip-detector, called MYTHEN (Microstrip sYstem for Time-resolved ExperimeNts).

Tab 4.1 Characteristic of MS – X04SA beamline at Paul Scherrer Institute

Energy range	**5-38 keV**
Flux (10 keV)	2.5 x 10^{13} ph/s/0.4 A
Focused spot size	130 µm x 40 µm (1:1 focussing)

The MYTHEN II detector is a general-purpose detector, with maximum resolution of 3.7 mdeg in 2θ, and very high efficiency and rapidly acquisition time.

This detector is particularly useful when either the scattering power is very low, or the acquisition times must be very short. It is therefore particularly suitable for time-resolved in-situ non-ambient XRPD.

Chapter V

Results and discussion

5 RESULTS AND DISCUSSION

5.1 *Results from Scanning Electron Microscopy analyses*

The samples AHS_209B and AHS_72 were analysed by Prof. Goodrich at Lunar and Planetary Institute of Houston using Scanning Electron Microscopy (SEM). These samples are defined as *"fine-grained, porous ureilites"* showing various degrees of "impact-smelting" and metamorphism as previously described for fine-grained AS ureilites and a few main group ureilites (Bischoff et al., 2010; Horstmann and Bischoff, 2014; Warren and Rubin, 2010; Zolensky et al., 2010). Olivine areas in AHS_209B are completely mosaicized. In detail, they consist of equigranular tiles aggregates of ~5-20 μm-sized (Warren and Rubin, 2010) with tiny amounts of interstitial pyroxene and Si-Al glass (Fig. 5.1a).

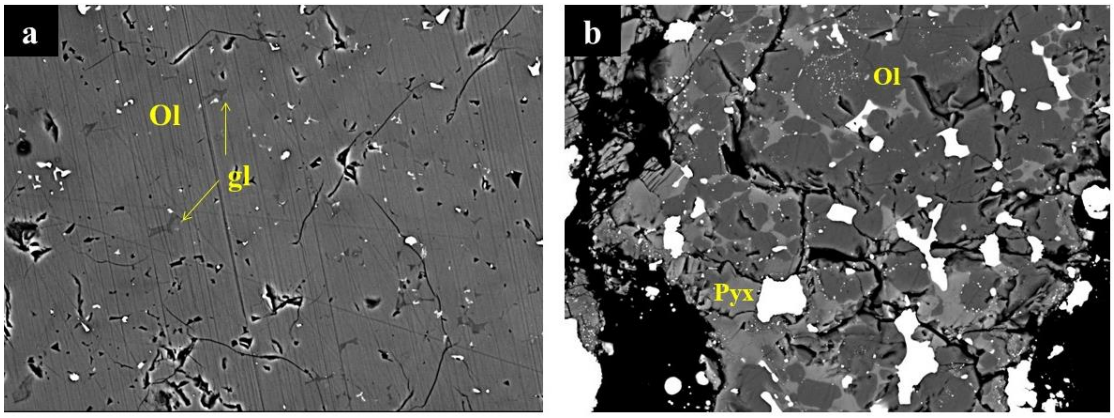

Figure 5.1 a) Back-scattered electron image of AHS_209B, showing dominant texture of olivine areas, **b)** Back-scattered electron image of less common, impact-smelted olivine area in AHS_209B.

The figure 5.1a shows a Back-scattered electron image of AHS_209B, where is present a dominant texture of olivine areas. Original olivine crystals are completely mosaicized (~5-20 mm-sized equigranular tiles) with minor interstitial Si-Al-enriched glass (marked as "gl" in the figure 5.1a). AHS_209B sample retains a typical ureilite primary olivine core composition of Fo ~79. Instead, the figure 5.1b shows a back-scattered electron image of less common, impact-smelted olivine area in AHS_209B, showing texture of equigranular, reduced olivine (Ol in figure 5.1b)

which presents composition of Fo 87-95, with interstitial pyroxenes (Pyx in the figure 5.1b) of various compositions.

The outlines of the originally larger (~mm-sized) primary grains are defined by cracks, masses of graphite, and metal. The olivine largely preserves a typical ureilite olivine core composition of Fo ~79, except in reduction rims near original grain boundaries or graphite inclusions. Reduction rim compositions range up to Fo ~93. Pigeonitic pyroxene areas in AHS_209B also show complete mosaicism with extensive in-situ reduction and porosity (Fig. 5.2).

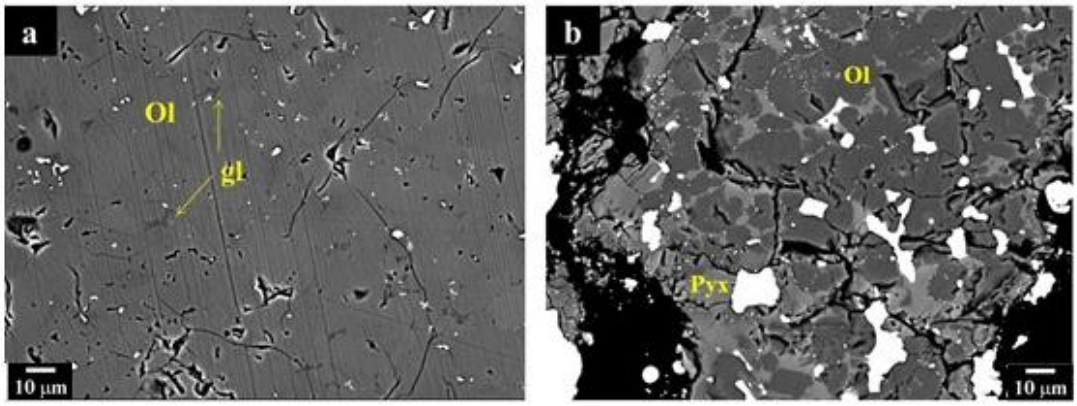

Figure 5.2 a) Back-scattered electron image of AHS_209B showing area of impact-smelted pyroxene and **b)** Secondary electron image of pore in AHS_209B, containing crystals that grew into pore space.

The figure 5.2a shows a back-scattered electron image of AHS_209B where is present the impact-smelted pyroxene area, consisting of aggregates of ~5-10 μm-sized subhedral grains, with small amounts of interstitial Ca-enriched pyroxenes and Si-Al enriched glass. Pores and small grains of metal and sulfide are common among the pyroxene grains.

Some pyroxenes in AHS_209B show additional in-situ reduction evidenced by dustings of fine metal grains. In this case, the grains do not show fully equilibrium metamorphic textures. The figure 5.2b shows secondary electron image of pore in AHS_209B, containing crystals that grew into pore space. Pores (Fig. 5.2b) and small grains of metal and sulphide among the pyroxene grains are common. The pyroxene tiles shown reverse zoning and the cores are reduced (core mg#s up to

~93) with varying Wo contents (~2-8) relative to inferred primary compositions (such as would have been in equilibrium with Fo ~79 olivine).

Dustings of very fine metal grains occur in some of the cores indicating multiples episodes of reduction. Similar pyroxene textures were described by Warren and Rubin (2010) in Almahata Sitta ureilites and attributed to "impact smelting."

The sample of AHS_72 examined is dominated by olivine and shows higher degree of metamorphism than AHS_209B. Olivine is completely re-crystallized to ~1-20 μm-sized equigranular (anhedral to subhedral) grains in a groundmass (of varying proportions relative to the amount of olivine) of pyroxene (Fig. 5.3).

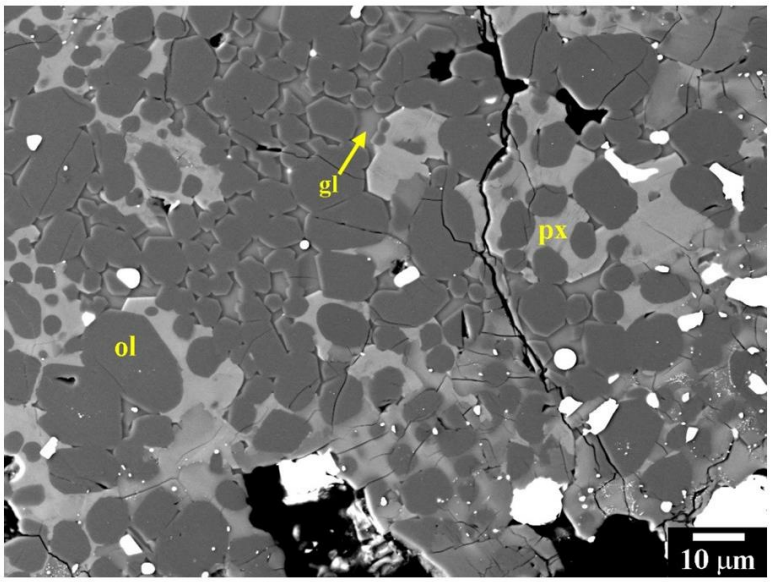

Figures 5.3 BSE image of AHS_72 with interstitial pyroxenes (px) and Si-Al glass.

The figures 5.3 shows back-scattered electron image of AHS_72, showing texture of equigranular, highly reduced olivine (ol) with cores composition of Fo 98-99, interstitial pyroxenes (px) of highly varied compositions (mg # 88-99, Wo ~1-33) and Si-Al-rich glass (gl).

The olivine grains are highly reduced (Fo ~99) and nearly free of inclusions, suggesting re-crystallization from a melt (or at least at very high temperatures) under highly reducing conditions. Interstitial pyroxene range composition from Wo 0.8 to Wo 34 and are also reduced (mg# 88-99).

Pores and masses of metal are abundant and generally on a much larger scale (~20 to 100s of μm) than the olivine grains.

Large graphite beds are interstitially present to silicate. The figure 5.4 shows an area of graphite masses, and some of these graphite beds in AHS_209B sample seem to have very fine-grained metal and sulfides mixed in.

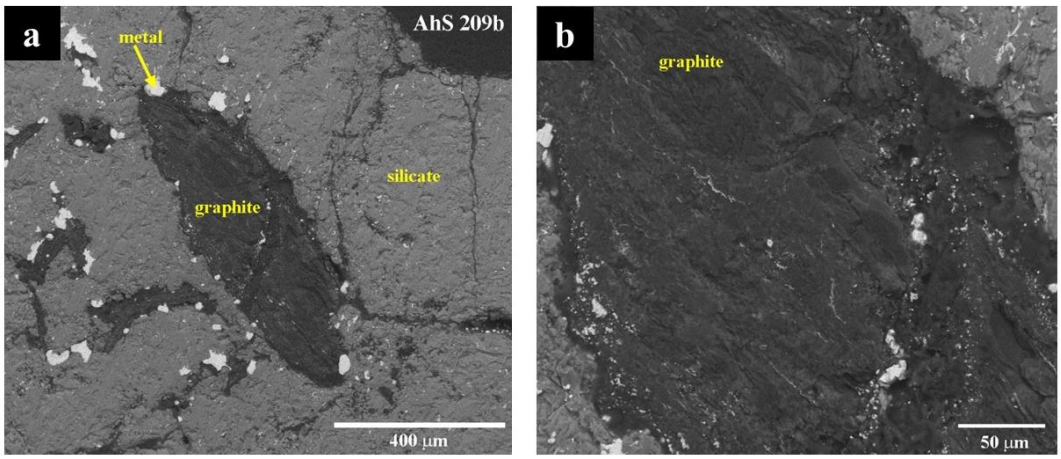

Figure 5.4 Back-scattered electron image of AHS_209B: individuation of graphite beds, where probably are situated the diamond phase; **a)** graphite (dark grey) surrounded by silicate (px and ol, light grey) and metal sulphide (white); **b)** a detail of graphite bed.

The SEM analyses was principally conducted to identify the graphite beds, where probably are situated the diamond phase. Suddenly the graphite beds identification, a little portion of material were collected from these regions and attached at the top of a 100 μm diameter vitreous capillary. This type of preparation of the samples was mandatory for the successive analyses by Micro-Raman Spectroscopy and Micro-XR Powder Diffraction.

The A135A ureilites sample was analysed at CEASC of University of Padua through Scanning Electron Microscopy (JSM Jeol6490). The SEM analysis focused on acquisition of BSE and SE images of graphite beds on A135A sample.

The A135A sample is very different with respect to AHS_209B and AHS_72 samples at BSE and SE observation. This examined sample is dominated by olivine and pyroxene (pigeonite) and shows many porous and metal sulphides blebs. The olivine does not show mosaicism, as well as demonstrated in the AHS_209B and

AHS_72 samples. Some point EDS and areal analyses were carried out on any portions of A135A sample, to have a first information about the phases present in the sample.

The figure 5.5 shows a back-scattered image of A135A sample, the spots and the rectangles in the figure 5.5 indicate the positions where point EDS analyses and areal EDS analyses were collected.

EDS analysis give qualitative and semi-quantitative information about the elements included in the sample.

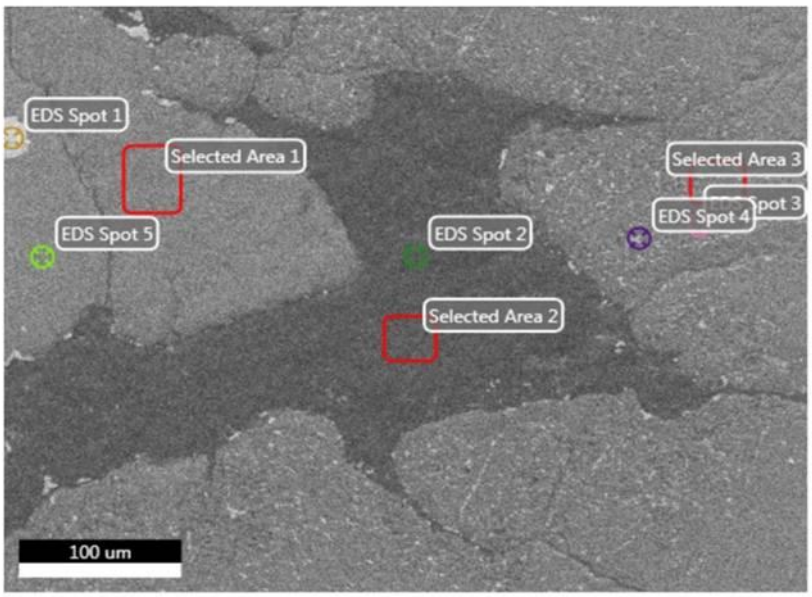

Figure 5.5 Graphite bed of A135A sample, where are collected some punctual micro-analyses of mineral composition, and three different areal EDS micro-analyses.

The EDS analyses were carried out suing the following conditions:

- Tension: kV 20;
- Amp. Time: 3.84;
- Live Time of 50(s);
- Resolution of eV 127.8;
- Take off: 45.3;
- Mag: 300;

Some EDS analyses were carried out on the areas of the figure 5.5; the graphic 5.1 compares the different weight% of elements individuated in selected areas of A135A sample (as shown in the figure 5.5) while the graphic 5.2 considers the EDS spots analysis. The values of weight% are reported in Tab.A1- A8 of the *Appendix A: EDS* analyses. The main aim of these measurements was to individuate the type of mineralogically phases present in the A135A sample.

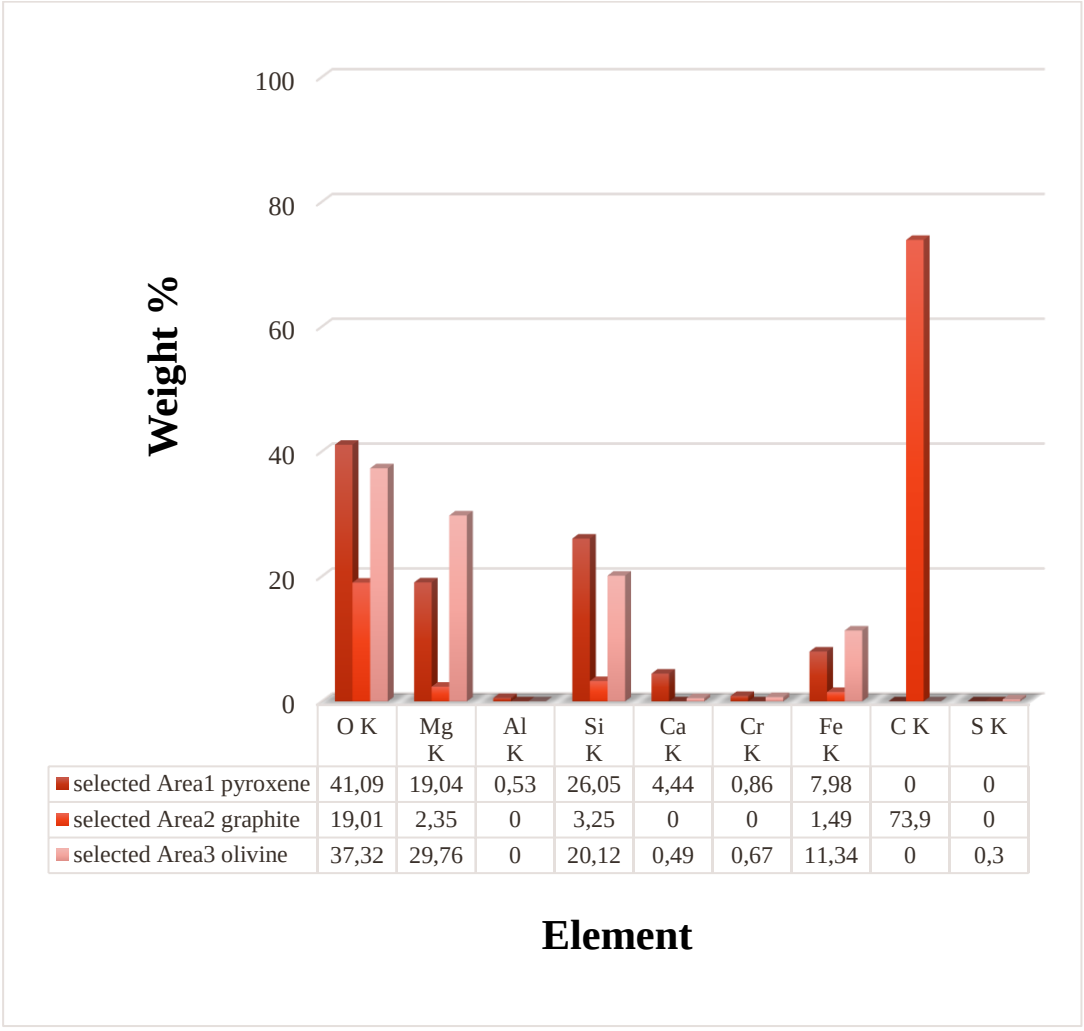

	O K	Mg K	Al K	Si K	Ca K	Cr K	Fe K	C K	S K
selected Area1 pyroxene	41,09	19,04	0,53	26,05	4,44	0,86	7,98	0	0
selected Area2 graphite	19,01	2,35	0	3,25	0	0	1,49	73,9	0
selected Area3 olivine	37,32	29,76	0	20,12	0,49	0,67	11,34	0	0,3

Graphic 5.1 Comparion of element weight% of selected Areas indicated in figure 5.5 using EDS.

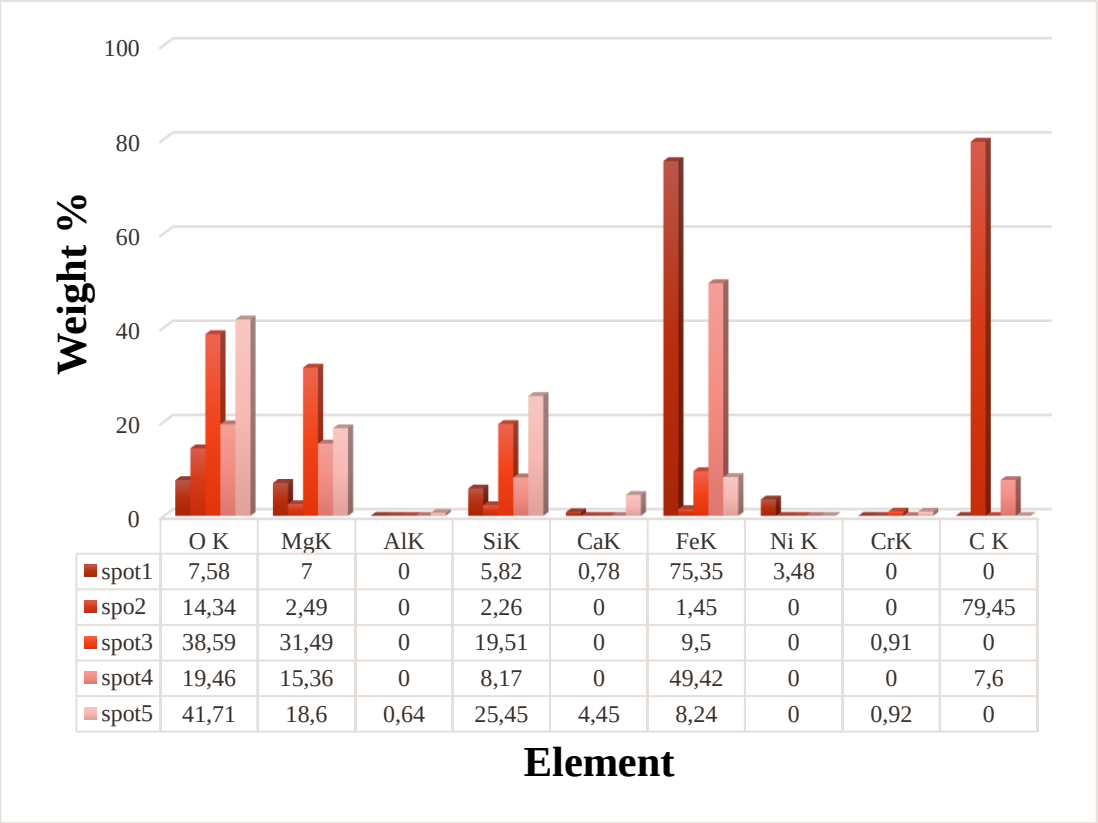

	O K	MgK	AlK	SiK	CaK	FeK	Ni K	CrK	C K
spot1	7,58	7	0	5,82	0,78	75,35	3,48	0	0
spo2	14,34	2,49	0	2,26	0	1,45	0	0	79,45
spot3	38,59	31,49	0	19,51	0	9,5	0	0,91	0
spot4	19,46	15,36	0	8,17	0	49,42	0	0	7,6
spot5	41,71	18,6	0,64	25,45	4,45	8,24	0	0,92	0

Graphic 5.2 Comparion of element weight% of selected spots indicated in figure 5.5 using EDS.

The presence of O K (~41.09 wt%), Si K (~26.05 wt%), Mg K (~19.04 wt%) and a few contents of Ca K (~4.45 wt%) in the selected area 1 and in the spot 5 indicates the pyroxene phase, and in particular pigeonite (low-calcium pyroxene, labelled Px in the figure 5.6). A large amount of C K (~73.9 wt%), O K (~19.01 wt%) and other minor negligible phases are present in selected area 2 and in the spot 2, indicating a graphite phase (labelled as G in the figure 5.6).

The selected area 3 and the spot 3 are composed by O K (~37.32 wt%), Mg K (~29.76 wt%), Si K (20.12 wt%) and Fe K (11.34 wt%) with other minor phases; these properties indicate olivine phase (labelled Ol in the figures 5.6).

The figure 5.6 summarizes the phases attribution conducted using the EDS analysis, previously discussed.

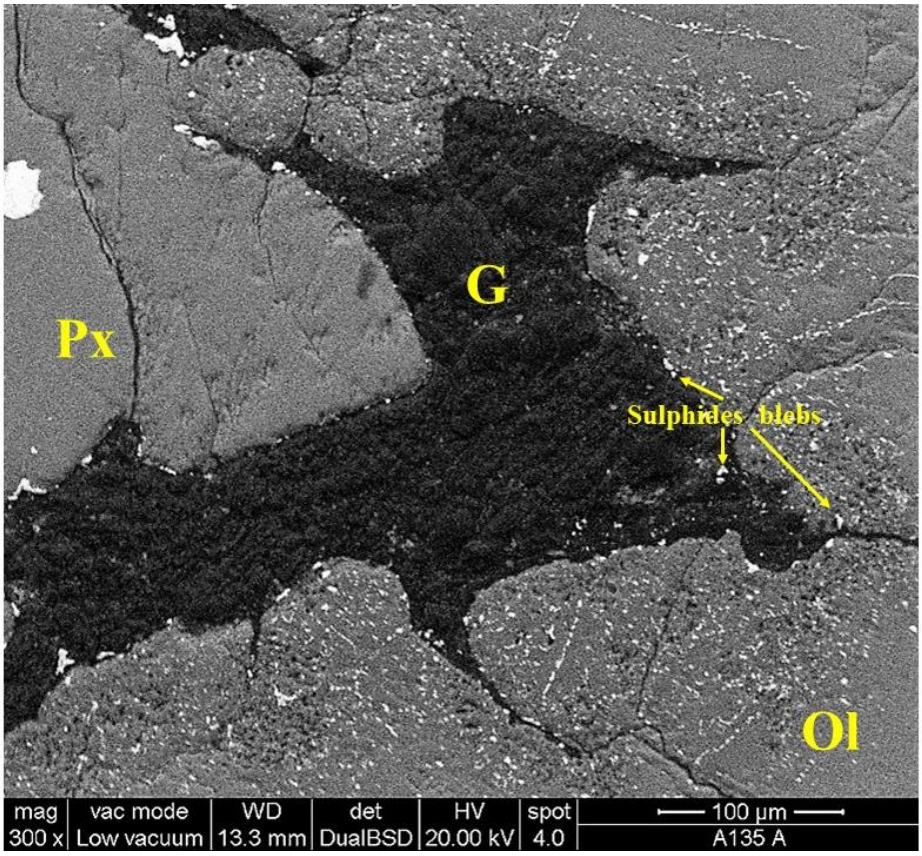

Figure 5.6 BSE image of same portion of figure 5.5. Three main mineral phases were detected using EDS analysis: Pyroxene (Pigeonite, Px), Olivine (Ol) and Graphite (G).

To detected diamonds, the identification of graphite bed is mandatory. Moreover, the study of graphite phase is crucial to successive individuation of a temperature crystallization through MRS. Several SE and BSE images of graphite beds of the sample A135A were collected; a deeply examination of these images revealed a disturbance, occurred during sample preparation. In the majority of individuated graphite beds, the presence of epoxy resin all around the graphite beds was found. The epoxy, which are embed A135A sample, was penetrated into the interstitial fractures among silicate and graphite. The evidence of this event is a difference C/O ratio between EDS spot analyses on the spot 1 respect to the spot 2 (figure 5.7).

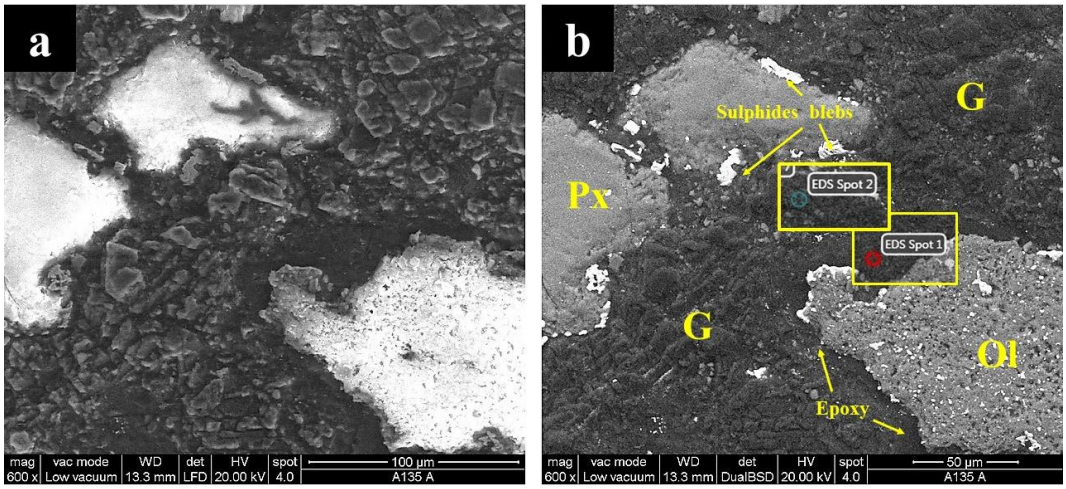

Figure 5.7 a) SE and b) BSE image of graphite beds in A135A sample, in **b)** are indicated the mineralogical phases associated and with spot 1 and spot 2 are indicated two point where EDS punctual analyses was effectuated.

The graphic 5.3 shows the different content of C K and O K in wt % among the spot 1 and spot 2 to underline the differences between the two spots collected, which referred to an epoxy resin zone and a graphitic zone, respectively.

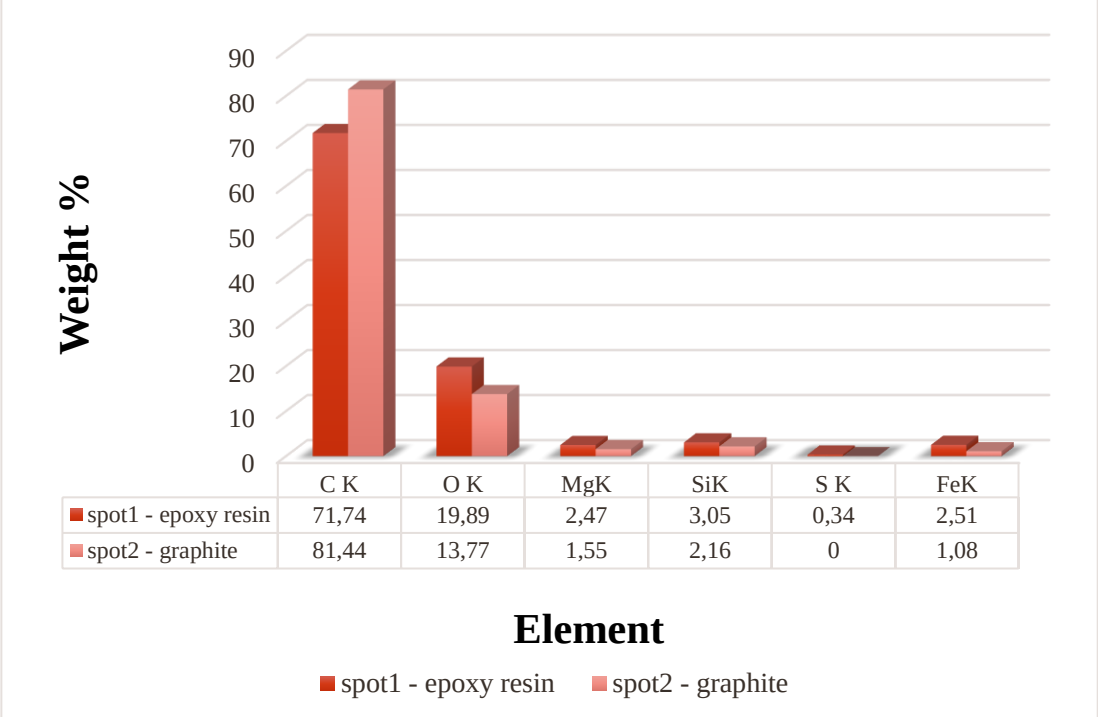

Graphic 5.3 Comparion of element wt% of selected spots indicated in figure 5.7 using EDS analysis.

The EDS analyses show a C/O ratio of spot1 and spot2 punctual analysis of 3.60 (C/O spot 1) and 5.95 (C/O spot 2), respectively. The data of spectra EDS spot 1 related to the spectra of image A3 are reported in the Tab. A9 of the *Appendix A: EDS analyses*, while data of spectra EDS spot2 related to spectra of image A3 are reported in Tab. A10 of the *Appendix A: EDS analyes*. The more abundant wt % of oxygen in the EDS analysis in spot 1 is referred to the epoxy.

Graphite beds are detected in A135A sample and a little portion of its material was extracted and it is attached at the top of a vitreous capillary. The A135A capillary samples are collected from graphite bed of the figures 5.8 a-b. The figure 5.8 shows many graphite beds in A135A sample observed in secondary electron and in back-scatter electron.

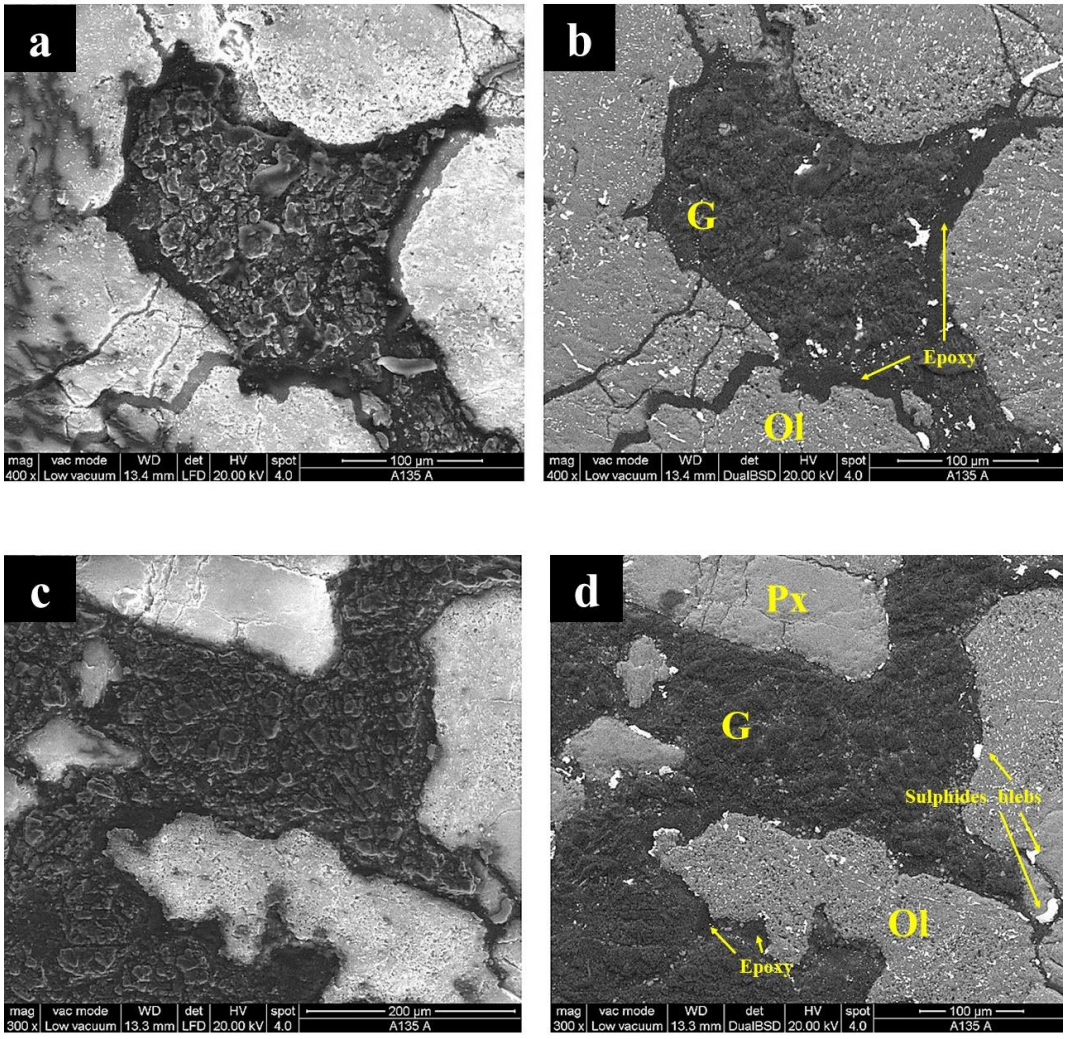

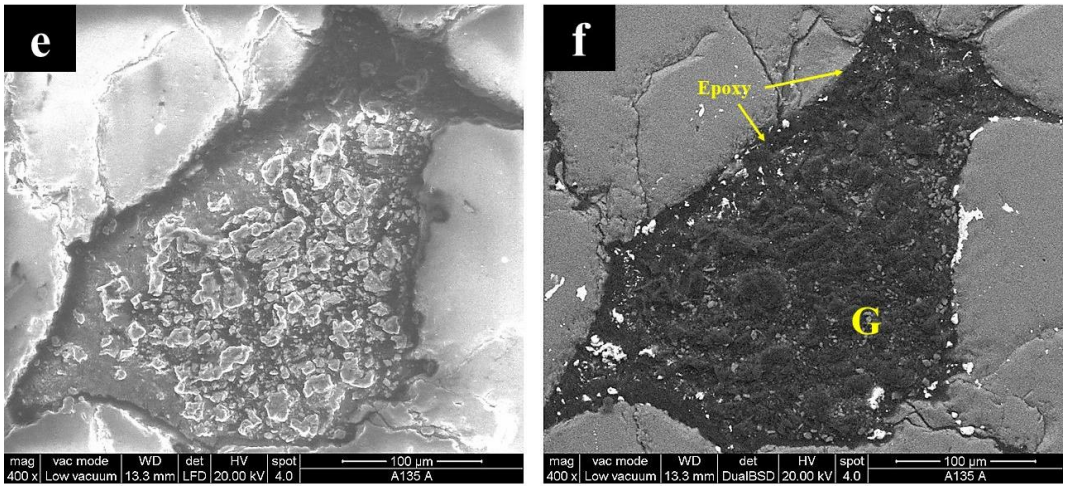

Figures 5.8 SE **(a-c-e)** and BSE **(b-d-f)** image of graphite bed in A135A sample: in the figures are report G (graphite), Px(pyroxene), Ol (olivine), Sulphur blebs and the epoxy resin.

Observation of AHS_209B and AHS_72 appeared different with respect to A135A. The A135A samples shown a less fractures of silicates phases and we do not observe the mosaicized olivine as oppose to AHS_209B and AHS_72 samples. These features could suggest us to attribute a minor shock grade to A135A sample, however more in-depth analysis will occur and the determination of crystallite size of diamond or also of other phases in the samples through micro-XR powder diffraction could give more information for the resolution of this problem.

5.2 *Results from Micro-Raman Spectroscopy (MRS) analyses*

Micro-Raman Spectroscopy (MRS) analysis of carbon phases on the three ureilitic fragments of *ASM* was conducted. Raman spectroscopy is an established method for mineral phase identification. The MRS is a sensitive technique to both characteristic mineral and carbon material, and different minerals usually show not overlapped spectra. MRS is a suitable approach for analysing carbon phases expected in ureilites. They are commonly graphite and diamond, and they have distinct characters in Raman spectrum. The MRS analysis focused on acquisition of Raman spectrum of carbon phases; in detail, the greatest number of Raman spectra collected are of graphite phase with the purpose to estimate the parent body temperature (T_{max}) and acquired information about the formation process of carbon phases.

The change of amorphous carbon to a crystalline structure caused by heating is an irreversible process. When carbonaceous material is heated, defects are lost, and the carbonaceous material organizes to a more structured form (Visser et al., 2018). This process results in a decreasing in the intensity of the so-called disordered bands (or D-bands) relative to the graphite (or G-bands) in Raman spectra (Tuinstra and Koenig, 1970). If a high enough temperature is reached, carbonaceous material can transform into a pure crystalline graphite structure that is characterized by a single sharp peak. Carbon thermometry uses the gradual changes in spectra properties with changing temperature to estimate the peak temperatures experienced by the material and the material's maturity (Beyssac et al., 2002; Busemann et al., 2007).

The carbon materials are great versatility, which arises from the strong dependence of their physical properties on the ratio of sp^2 (like graphite) to sp^3 (like diamond) bonds. There are many forms of sp^2-bonded carbons with various degrees of graphitic ordering, ranging from microcrystalline graphite to glassy carbon. In general, an amorphous carbon can have any mixture of sp^3, sp^2, and even sp^1 sites. The Raman spectra of disordered graphite usually show two quite sharp modes, the *G* peak around 1580–1600 cm^{-1} and the *D* peak around 1350 cm^{-1}.

An important relationship between the ratio of the intensity of D-band and G-band I(D)/I(G), to that of the G-band peak, and crystalline size of graphite (L_a) was noted by Tuinistra and Koenig (1970).

$$\frac{I(D)}{I(G)} = \frac{C(\lambda)}{L_a} \quad (1)$$

In detail, the Tunistra and Koenig *(TK) equation (1)* shows that there is an inversely correlation between L_a and I(D)/I(G) ratio. C of laser used in the measure is of λ=514 nm, which corresponds to ~ 44Å.

The Raman spectrum, in addiction to temperature is considered to depend on:

- clustering of the sp^2 phase;
- bond disorder;
- presence of sp^2 rings or chains;
- the sp^2/sp^3 ratio;

These factors act as competing forces on the shape of the Raman spectra, as shown schematically in the figure 5.9.

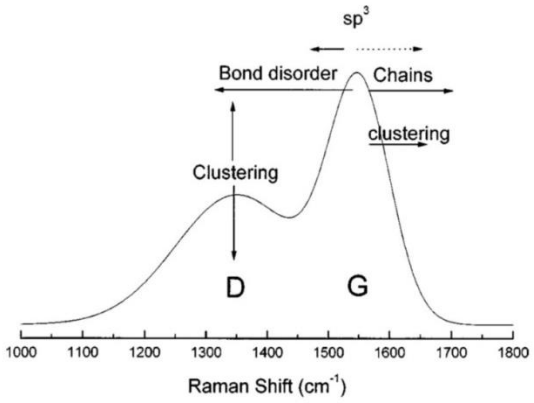

Fig.5.9 Schematic diagram of influences on Raman spectra. A dotted arrow indicated the influence of the sp^3 content on increasing G-position, from Ferrari and Robertson, (2000).

Ferrari and Robertson et al. (2000) defined an *amorphization trajectory* ranging from graphite to defect diamond *(ta*-C) consisting of three stages (Fig. 5.10 a-b):

Stage 1): From graphite to nanocrystalline graphite;

Stage 2): From nanocrystalline graphite to a-C (~20% sp^3);

Stage 3): From a-C (~20% sp^3) to ta-C (~100% sp^3 *ta-C*);

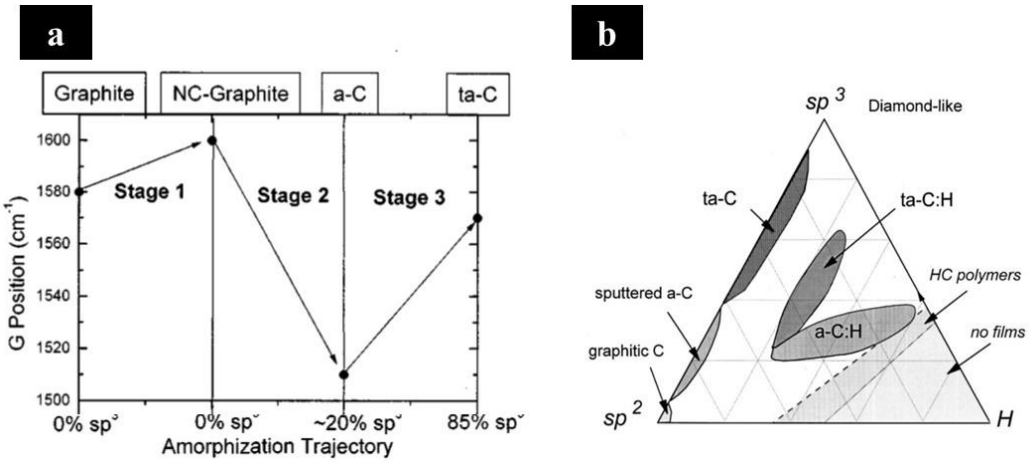

Figures 5.10 a) Amorphization trajectory with a schematic variation of the G-band position and **b)** ternary phase diagram of amorphous carbon. In it are indicated in the corners diamond, graphite and hydrocarbons respectively (Ferrari and Robertson, 2000).

The main effects in the evolution of the Raman spectrum in Stage 1) are as follows:

(a) The G-band peak moves from 1581 cm^{-1} to ~ 1600 cm^{-1};

(b) Three D-band peaks appear and I(D)/I(G) increases following the TK *equation (1)*.

(c) There is no dispersion of the G-band mode.

Although, at first the shift of G-band is really the appearance of a second peak, D'-band, at ~1620 cm^{-1}, which merges in the G-band peak for small grains.

The main changes in the evolution of the Raman spectrum in Stage 2) are:

(a) The G-band peak decreases from 1600 cm^{-1} to ~1510 cm^{-1};

(b) The *TK equation (1)* is no longer valid;

(c) I(D)/I(G) → 0;

(d) Increasing dispersion of the G-peak occurs.

Finally, the main effects in the evolution of the Raman spectrum for Stage 3) are as follows:

(a) The G-band peak increase from ~1510 to ~1570 cm^{-1} (or 1630 cm^{-1});

(b) I(D)/I(G) is very low or 0;

(c) Dispersion of the G-band peak occurs;

Singles Raman spectrum were collected with the inVia Renishaw micro-Raman spectrometer. The samples were excited with a 514 nm solid state laser. The lithospheric diamond takes as standard and all the urelitic samples were analysed at a laser operating power of 1.9 mW (measured without objective, which probably should reduce the operating power of 20-30%). The objective lens of magnification of 50x for AHS_209B (B1, B2, B3, B4), AHS_72 and 100x for A135A was used respectively. Curve fitting of the spectrum were carried out using the software OMNIC for dispersive Raman. A Gaussian + Lorenzian curve was automatically fitted to the Raman spectral peaks, then manually checked and corrected to obtain the best fit.

5.2.1 Micro Raman Point Analyses

The greatest number of Micro-Raman point spectrum collected are of graphite phase. To avoid measuring on polished surface graphite, graphite spectrum was collected on fragments of ASM attached on the top of a vitreous capillary (100μm) collected on fresh fracture of exposure surfaces of AHS_209B, AHS_72 and A135A in epoxy samples. The Raman spectrum of graphite of our samples usually shows three peaks, G and D bands and also the addiction of the D'-band, as G-band lamp:

- G-band at around 1580 cm^{-1}, which is the band inherent to graphite;
- D-band at around 1355 cm^{-1}, which is defect induced band;
- D'-band at around 1620 cm^{-1}, as a shoulder on the G-band;

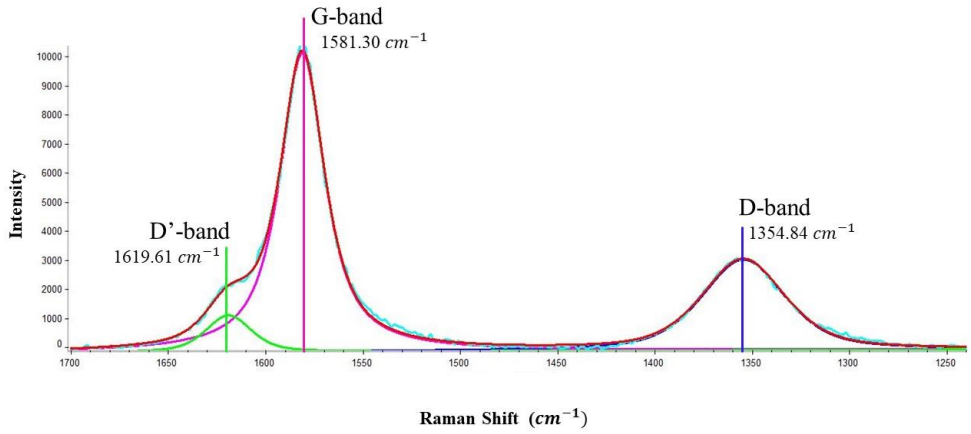

Figure 5.11 Raman spectra of AHS_209B3 sample, where are indicated the peak position of D-band (1354.84 cm^{-1}) in blue, G-band (1581.30 cm^{-1}) in pink and D'-band (1619.16 cm^{-1}) in green.

The figure 5.11 shows the peak position of D, G and D' bands in the Raman spectra of AHS_209B3 sample.

The presence of D'-band at ~1620 cm^{-1}, as lamp of G-band peaks in almost all *ASM* Raman spectrum and the relative I(D)/I(G) ratio suggest to collocate the graphite phase of our samples analysed during this Master thesis in Stage 1) of amorphized trajectory determined by Ferrari and Robertson (2000).

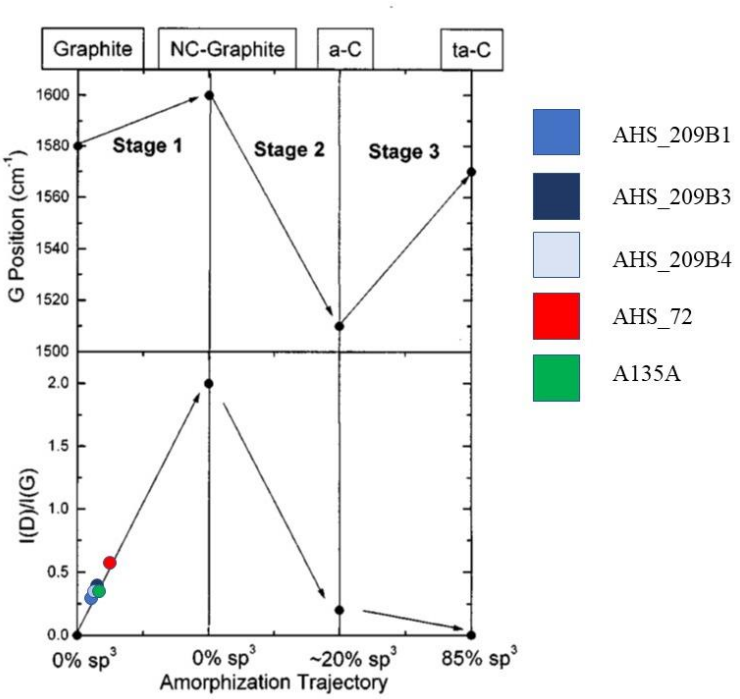

Figure 5.12 Amorphization trajectory, showing a schematic value of the G-bands position and I(D)/I(G) ratio. In detail, blue and light blue spots are the media of the I(D)/I(G) ratio of all Raman acquisition of AHS_209B sample in amorphized trajectory, the red spot indicate the position in amorphization trajectory of the media of the I(D)/I(G) ratio of all Raman acquisition of AHS_72 sample and the green spot indicate the position in amorphization trajectory of the media of the I(D)/I(G) ratio of all Raman acquisition of A135A sample. Modified image from Ferrari and Robertson, 2000.

On the Stage 1) the first shift of G-band is really the appearance of a second peak, D'-band, at ~1620 cm^{-1}, which merges in the G-band peak for small grains. The I(D)/I(G) ratio medium values for each analyzed sample are ~0.331 for AHS_209B1, ~0.418 for AHS_209B3, ~0.380 for AHS_209B4, ~0.636 for AHS_72 and ~0.388 for A135A; these values introduced in the amorphization trajectory of Ferrari and Robertson (2000) are collocated in Stage 1) of the trajectory as reported in the figure 5.12.

All the parameter of Raman spectrum acquisition of AHS_209B, AHS_72 and A135A samples for the I(D)/I(G) ratio are reported in Tab.5.1. The crystalline size of graphite (L_a), defined using the *TK equation (1)* and assuming that *C* (514nm) was ~44Å (Tuinstra and Koenig, 1970) is also reported in Tab. 5.1 .

Table 5.1 Report of height D-bands, height G-bands, I(D)/I(G) ratio and L_a of all Micro-Raman acquisition for each sample of *ASM* analysed

	Sample	**Height D-band**	**Height G-band**	**I(D)/I(G)**	**L_a(nm)**
50x mag	***AHS_209B1***				
	(a)	2452.56	12057.25	0.204	216.3
	(b)	4133.32	12473.31	0.331	132.8
	(c)	5605.44	12780.06	0.439	100.3
	(d)	3344.91	9795.64	0.341	128.8
	(e)	1574.12	4561.31	0.446	127.5
	(f)	1920.12	8420.15	0.228	192.9
50x mag	***AHS_209B3***	**Height D-band**	**Height G-band**	**I(D)/I(G)**	**L_a(nm)**
	(a)	5334.74	8078.09	0.660	66.6
	(b)	2381.80	7976.31	0.298	147.4

	(c)	5652.58	11272.74	0.501	87.8
	(d)	3120.96	10375.35	0.301	146.3
	(e)	5293.12	13890.45	0.3810	115.5
	(f)	3758.84	10284.92	0.365	120.4
50x mag	***AHS_ 209B4***	**Height D-band**	**Height G-band**	**I(D)/I(G)**	**L_a(nm)**
	(a)	7624.69	14647.59	0.521	84.5
	(b)	3204.79	8628.84	0.371	118.5
	(c)	4561.22	11622.16	0.393	112.1
	(d)	3273.30	8028.90	0.408	107.9
	(e)	3753.71	13519.25	0.278	158.5
	(f)	3001.3	9697.13	0.309	142.2
50x mag	***AHS_72***	**Height D-band**	**Height G-band**	**I(D)/I(G)**	**L_a(nm)**
	(a)	4818.56	11381.64	0.423	103.9
	(b)	4602.19	7996.35	0.576	76.5
	(c)	1574.85	3166.71	0.497	88.5
	(d)	6100.16	9181.29	0.664	66.2

	(e)	4994.05	7967.63	0.627	70.2
	(f)	5187.08	10415.22	0.498	88.4
100x mag	***A135A***	**Height D-band**	**Height G-band**	**I(D)/I(G)**	**L_a(nm)**
	(a)	364.40	835.57	0.436	76.5
	(b)	341.16	964.68	0.354	92.5
	(c)	524.96	604.07	0.869	30.5
	(d)	144.61	952.27	0.152	129.5
	(e)	436.60	1294.70	0.337	243.4
	(f)	106.49	589.12	0.181	137.9

The crystalline size of graphite (L_a) estimated for the samples are heterogeneous but always in the range of nanometric scale. This confirmed the choice to attributes the graphite of our samples to Stage 1) of amorphized trajectory of Ferrari and Robertson (2000), which describe the transition of graphite up to nanometric graphite.

Most of the graphitic material in *ASM* have a narrow range of G-band peak centre wave numbers and FWHM in the crystalline graphite. In any spectra acquisitions, considerable higher FWHM (FWHM > 40 cm^{-1}) were present and they are attributable to high disordered carbon defined amorphous carbon (Ross et al., 2011) (Tab.5.3).

Cody et al. (2008) originated an expression for the parent body temperature (T_{max}) in terms of Raman G-band FWHM (Γ_G) of carbonaceous matter in chondrites:

(2) $$T_{max}(°C) = 1594.4 - 20{,}4\Gamma_G - 5.8 \times 10^{-2}\Gamma_G^2$$

The *equation (2)* derived by Cody et al. (2008) was applied to ureilites and Ross et al (2011) applied it to graphite of Almahata Sitta ureilites, giving an average maximum temperature of 990±120 (error was calculated by Cody et al., 2008; Ross et al., 2011).

To obtain the parent body temperature related to our samples, the full widths of the graphite peak at half-maximum intensity (FWHM of G-band) were used for AHS_209B (B1, B3, B4), AHS_72 and A135A. The G-bands of each several acquirements of each sample were divided by a ratio between FWHM of a lithospheric diamond (Dl) measured at the same acquired parameters of the samples (Tab 5.2) and a FWHM of a terrestrial diamond used by Ross et al. (2011) taken as a standard FWHM referred.

Table 5.2 Raman spectra parameters of lithospheric diamond FWHM standard.

Lithospheric diamond	**Peak Center (cm^{-1})**	**Height**	**Std FWHM D(cm^{-1})**	**$\frac{\text{Std FWHM Dl}}{\text{Std FWHM Ross et al 2011}}$**
50x mag	1332.11	43810.01	5.9707	1.99
100x mag	1332.02	2372.77	5.7407	1.91

Applying the *equation (2)* to graphite G-band FWHM data we obtained a range of maximum temperature of the parent body between ~ 1103 (min) and 1360 (max) ±120 °C for AHS_209B, between ~ 1165 (min) and 1294 (max) ±120 °C for AHS_72 and finally between ~ 1249 (min) and 1377(max) ±120 °C for A135A samples of *ASM*. To obtain correct temperatures, the FWHM of the G-bands were corrected with the ratio between the FWHM of lithospheric diamond taken as a standard and FWHM of a terrestrial diamond taken as a standard by Ross et al. 2011 (Tab. 5.2). All the temperatures of several MR point analysis are reported in Tab

5.3. The Raman spectra referred to each sample acquisition with related parameter are in *Appendix B: Micro-Raman Spectroscopy analyses*.

Our results are according with the estimated parent body temperatures resulted by other *ASM* fragments.

Herrin et al. (2010) applied two different pyroxene thermometers of Kretz (1982) and Brey and Köhler (1990) and calculate an equilibrium temperatures of 1190–1250 °C. These temperatures are consistent with the error range of graphite estimated equilibrium temperature of the samples AHS_209B, AHS_72 and A135A of this work.

The temperatures also overlap with pyroxene equilibrium temperatures from the Antarctic augite-bearing ureilites described by Herrin et.(2010).

Table 5.3: All *ASM* (AHS_209B, AHS_72 and A135A) graphite G-band with respective FWHM of several acquisition by inVia Renishaw micro-Raman. The equation (2) was applied to data collected and gave results range temperature among ~1235-1340 °C. The Raman spectra referred to this temperature is in figures B1, B2, B3 and B4 of Appendix B with respectively Tabs B1, B2, B3 and B4.

	Sample	**Peak centre G-band (cm^{-1})**	**FWHM (cm^{-1})**	**FWHM/ 1.99**	**T (°C) Ross**
50x mag	***AHS_ 209B1***				
	(a)	1582.02	22.19	11.15	1360 ±120
	(b)	1581.80	26.74	13.44	1310 ±120
	(c)	1582.49	35.50	17.84	1212±120
	(d)	1582.05	26.85	13.49	1309±120
	(e)	1583.60	30.12	15.14	1272±120
	(f)	1582.55	29.00	14.57	1285±120

50x mag	***AHS_ 209B3***	**Peak centre G-band (cm^{-1})**	**FWHM (cm^{-1})**	**FWHM/ 1.99**	**T (°C) Ross**
	(a)	1584.75	45.00	22.61	1103±120
	(b)	1573.78	33.39	16.78	1236±120
	(c)	1582.74	33.32	16.74	1237±120
	(d)	1581.30	27.60	13.87	1300±120
	(e)	1582.81	29.04	14.59	1284±120
	(f)	1583.31	31.79	15.97	1254±120
50x mag	***AHS_ 209B4***	**Peak centre G-band (cm^{-1})**	**FWHM (cm^{-1})**	**FWHM/ 1.99**	**T (°C) Ross**
	(a)	1581.22	43.40	21.81	1122±120
	(b)	1582.46	26.47	13.30	1313±120
	(c)	1581.89	24.71	12.42	1332±120
	(d)	1580.90	34.86	17.52	1219±120
	(e)	1580.10	22.36	11.23	1357±120
	(f)	1582.14	28.13	14.14	1294±120

50x mag	***AHS_72***	**Peak centre G-band (cm^{-1})**	**FWHM (cm^{-1})**	**FWHM/ 1.99**	**T (°C) Ross**
	(a)	1577.54	32.59	16.38	1244±120
	(b)	1578.96	39.59	19.89	1165±120
	(c)	1581.30	29.12	14.63	1283±120
	(d)	1583.70	32.47	16.32	1246±120
	(e)	1582.72	28.16	14.15	1294±120
	(f)	1582.92	30.01	15.08	1273±120
100x mag	***A135A***	**Peak centre G-band (cm^{-1})**	**FWHM (cm^{-1})**	**FWHM/ 1.91**	**T (°C) Ross**
	(a)	1582.41	24.86	12.99	1320±120
	(b)	1583.80	30.98	16.19	1249±120
	(c)	1582.15	19.73	10.31	1377±120
	(d)	1581.74	22.21	11.61	1345±120
	(e)	1580.46	21.24	11.10	1361±120
	(f)	1582.30	23.08	12.063	1340±120

The Raman spectrum of AHS_209B1, AHS_72 and A135A sample with relative parameter tabs are reported in the *Appendix B: Micron-Raman Spectroscopy analyses.*

5.3 Result from Micro-XR Powder Diffraction analyses (MXR)

Micro X-Ray Power diffraction (*MXR*) data of the *ASM* urelitic sample, AHS_209B, AHS_72 and A135A were collected. The experiments were conducted at Paul Scherrer Institute (PSI), Switzerland, through MS-X04SA beam line. The MS beamline is powered by a short-period (14 mm) in-vacuum, cryogenically cooled and permanent-magnet undulator. The measures were effectuated with a wavelength of the beamline of λ=0,70861 Å, close to Mo wavelength (0.7107 Å).

The Micro X-Ray powder diffraction data could allow to obtain qualitative and quantitative information about diamond, graphite and other minor phases present in the samples. The main aim of these experiments was to understand the crystallite size of the diamonds through line profile analysis fit; qualitative and quantitative analysis was not the aim of this thesis.

X-ray diffraction line profile analysis is a versatile non-destructive method in material research to obtain microstructural information. From the position and broadening of diffraction lines information is obtained about the imperfect crystalline structure in term of effective crystallite (domain) size.

A complete line profile analysis consisted of three stage (Delhez et al., 1982):

(a) Measurements acquirement;
(b) Corrections of the line profile measured and calculation of parameter of fit profile;
(c) Evaluation of parameters obtained.

After the data acquisition, the elaboration through line profile analysis was required using High Score Plus Software package.

To describe the shape of the profiles, analysis exists in terms of *integral breadth* adopting a Voight function. It is possible to use also the full width at half maximum (FWHM), but this parameter does not consider asymmetry features, which are present in many peaks of profiles of the samples (as the graphite peaks).

In fact, the *integral breadth* contained the shape contribute of the crystallite and it is the total area under the peak divided by the peak height, or the width of a rectangle having the same area and the same height as the peak; while *FWHM* is the width of

the diffraction peak at a height half-way between background and the peak maximum *intensity*. The difference among Integral breadth and FWHM is schematically reported in figure 5.13.

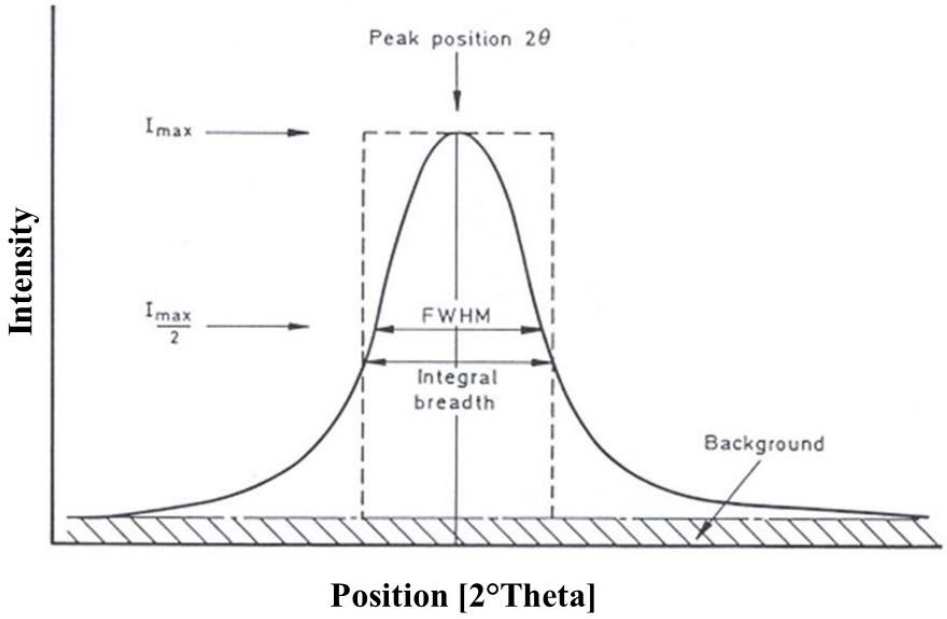

Figure 5.13 The differences between FWHM and Integral breadth in a diffraction peak.

A subtraction of instrumental broadening was necessary using a NAC ($Na_2Ca_3Al_2F_{14}$) standard. It was possible to use NAC standard only because it has an Integral breath less than samples, or therefore with greater crystallite size respect the sample.

A first line profile analysis was conducted on NAC sample through a Voight function to set its refinement parameters as LP analysis standard; the sequent steps are deleted the anchor scan data of NAC, but the refinement parameter remained save anyway on *Refinement Control* tabs.

Suddenly, in the same window of line profile analysis performed on NAC sample, were insert (one by one) the .dat diffraction data file inherent to AHS_209B, AHS_72 and A135A samples. The detailed background subtraction was required for each analysed sample and it was very important to final fitting of line profile analysis.

The individuation of the several peaks on profiles for line profile analysis is essential. Pseudo Voigt profile function was used for all analysed samples, with a *profile base width* set on 12 and a profile fit setting with an *Asymmetry type* set on *Split width and Shape* for obtain the better fit of the line profile, to avoid fit-problems related to peaks asymmetry. In figure 5.14 the line profile analysis fits of diffractograms of AHS_209B are reported.

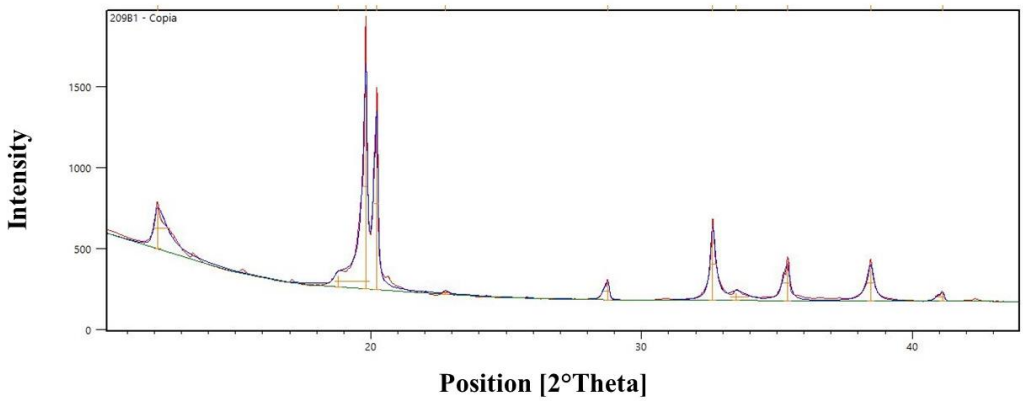

Figure 5.14 The line profile analysis fitting of the AHS_209B1 sample of *ASM*.

The line profile analysis fits of diffractograms of AHS_72 and A135A are reported in figure C 1) of *Appendix C: Micro-XR powder diffraction analyses*.

For the determination of the crystallite size peaks position (2θ°) of diamond was used, not overlapped with other peak position of other phases, and the respectively integral breadth values are inserted to Scherrer *equation (3)* in order to derive crystallite size of diamond.

(3) $$\beta(2\theta) = \frac{K_\beta \times \lambda}{<D>_V \cos\theta_{hkl}}$$

(4) $$\frac{D_V}{K_\beta} = \frac{\lambda}{\cos\theta_{hkl} \times \beta(2\theta)}$$

The Scherrer equation *(3)* gives a correlation between β peaks broadening and the dimension of diffracted domain, the crystallite size *(D_v)*. *K* is a constant value between 0.5 and 1, and it describes the contribution of crystallites shape. *K* is a parameter that depends on the relative orientation of the scattering vector to the

external shape of the crystallite (Langford and Wilson, 1978; Miranda and Sasaki, 2018; Patterson, 1939).

Only two diamond diffraction peaks are not overlapped with graphite peaks at position 32,63 [2θ°] and ~38,47[2θ°]; the crystallite size for these two peaks was estimated for AHS_209B (Tab. 5.4), AHS_72 (Tab.5.5) and A135A (Tab. 5.6).

Further diffraction peaks overlapped with those of other phases are useless because their Integral breath is the result of the contribution from all diffraction peaks overlap. This could give an overestimation of Integral breadth and consequently an underestimation of the crystallite size of diamond.

The figure 5.15 shows the two not overlapped diffraction diamond position peaks on diffractogram of AHS_209B1 sample. On the peak 2θ° position of 32.6 the diamond peak position is overlapped with lonsdaleite phase, but, as explained in chapter 3, lonsdaleite is to consider a diamond defect; lonsdaleite has never been produced or described as a separate, pure material (Nemeth et al., 2014).

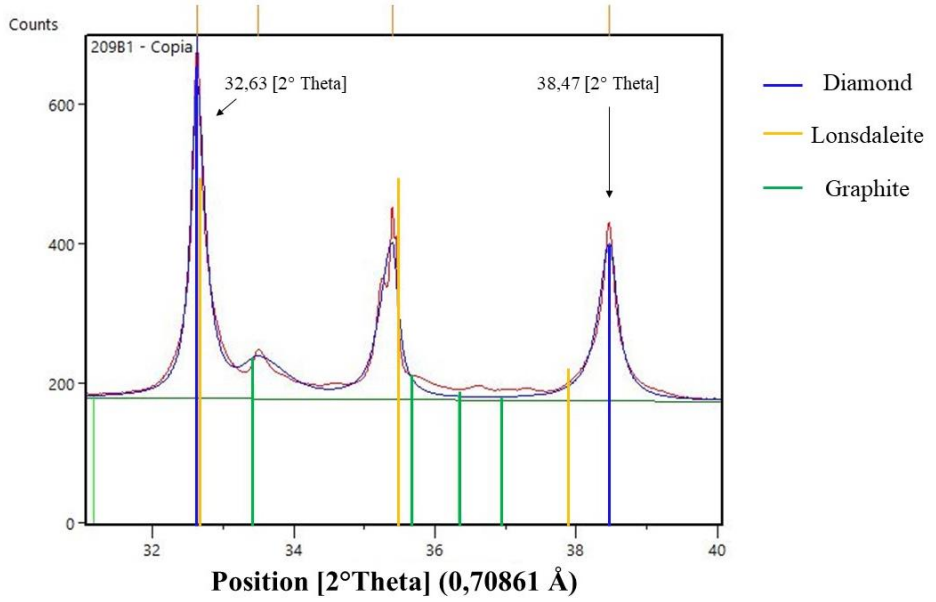

Figure 5.15 Diffractogram of AHS_209B sample where are indicated the not overlapped peak position of diamond phase at 32.63 and 38.47 position 2θ°; the diamond 2θ° position with λ=0,70861 Å is indicated with blue line, while lonsdaleite and graphite with yellow and green lines, respectively.

The crystallite size for AHS_209B sample is ~10 nm (10.9 nm at peak position 32.63 2θ° and 8.9 nm at peak position 38.47 2θ°), for AHS_72 sample is~30-40 nm (42.3 nm at peak position 32.63 2θ° and 27.9 nm at peak position 38.46 2θ°) and finally for A135A sample is ~10 nm (13.7 nm at peak position 32.63 2θ° and 10.9 nm at peak position 38.48 2θ°).

Table 5.4 Crystallite size of diamonds referred to no overlapped peak with graphite peaks of AHS_209B sample

AHS_ 209B1						
λ	**Pos. [2θ°]**	**Pos θ [rad]**	**cos(th)**	**Beta (2θ°)**	**Beta 2θ(rad)**	**D_v (nm)**
0.70861	32.63	0.285	0.960	0.385	0.006723183	10.9
	38.47	0.336	0.944	0.479	0.008355048	8.9

Table 5.5 Crystallite size of diamonds referred to no overlapped peak with graphite peaks of AHS_72 sample

AHS_ 72						
λ	**Pos. [2θ°]**	**Pos θ [rad]**	**cos(th)**	**Beta (2θ°)**	**Beta 2θ(rad)**	**D_v (nm)**
0.70861	32.63	0.285	0.960	0.100	0.001746	42.3
	38.46	0.336	0.944	0.154	0.002692	27.9

Table 5.6 Crystallite size of diamonds referred to no overlapped peak with graphite peaks of A135A sample

A135A						
λ	**Pos. [2θ°]**	**Pos θ [rad]**	**cos(th)**	**Beta (2θ°)**	**Beta 2θ(rad)**	**D_v (nm)**
0.70861	32.63	0.285	0.960	0.308	0.005381339	13.7
	38.48	0.336	0.944	0.395	0.006886738	10.9

The crystallite size estimated from line profile analysis of AHS_209B and A135A samples are similar around ~10 nm, while in AHS_72 sample it is different around ~40 nm; although, both evaluation of the crystallite size of diamond revealed nanometric size.

The graphic 5.4 shows the changing of values of Integral breadth in no-overlapped diamond peak position, at 32.63 2θ°. and 38.48 2θ° position (Tab. 5.4, Tab. 5.5 and Tab. 5.6).

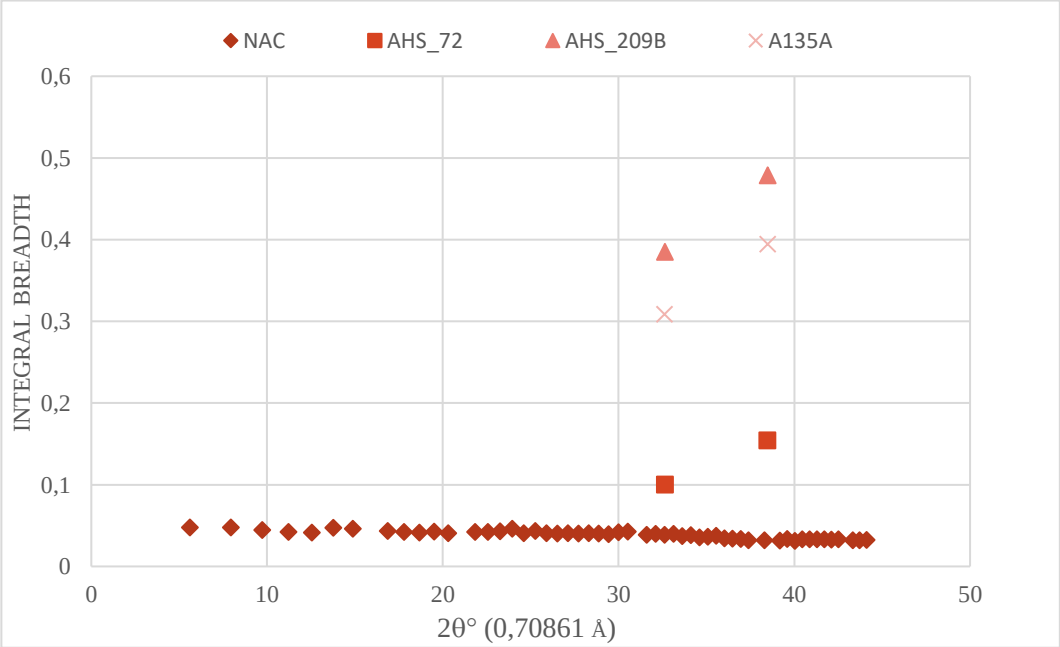

Graphic 5.4 Changing in Integral breath at different not overlapped diamond peaks.

In the diffractograms of the samples of *ASM*, the presence of lonsdaleite lamp suggests that cubic and hexagonal stacking in diamond of samples are present and they are intercalated in complex mode, not simply describing to a simple physical mixture of cubic and hexagonal diamond (Nemeth et al., 2014; Salzmann et al., 2015).

In the future, further analyses of diamond stacking faults will have to be carried out in order to estimate the contribution in the increasing of the integral breadth and consequently the underestimation of crystallite size of diamond with the line profile analysis method.

Chapter VI

Conclusions

6 Conclusions

In this Master Thesis, a detailed study of diamond and graphite in Almahata Sitta meteorite sample AHS_209B, AHS_72 and A135A was conducted using Scanning Electron Microscopy, micro- Raman spectroscopy and micro-XR powder diffraction.

SEM results provide several morphology information of graphite beds and important information about textural aspect of ASM ureilitic fragments during Master thesis. Observation of AHS_209B and AHS_72 appeared different with respect to A135A. The A135A samples shown a less fractures of silicates phases and we do not observe the mosaicized olivine as oppose to AHS_209B and AHS_72 samples. These features could suggest us to attribute a lower shock grade to A135A sample. However, for such sample a deeper analysis would be necessary.

MRS results show that graphite in ASM was not highly crystalline. This is demonstrated by the presence of D′-band at ~1620 cm^{-1}, as lamp of G-band peaks in almost all ASM Raman spectrum of samples. These features and ratio values of I(D)/I(G) between 0.3 and 0.6 suggest to collocate the graphite phase of analysed sample in Stage 1) of amorphized trajectory determined by Ferrari and Robertson (2000). In fact, at first the shift of G-band, noted for the Stage 1) of the amorphized trajectory, is really the appearance of a second peak, D′ at ~1620 cm^{-1} as lamp of G-band; it is the same case of our samples.

The results from *TK equation (1)* characterized the crystalline size of graphite at nanometric scale (~100 nm) and it support the collocation of graphite phases of analyzed samples in Stage 1).

The application of Cody *equation (2)* to graphite G-band FWHM data for AHS_209B, AHS_72 and A135A samples of ASM described a temperature of ~ 1200-1300 (± 120) °C. The assumption that when carbonaceous material is heated, defects are lost and the carbonaceous material is organized in a more structured form (Visser et al., 2018) is due to high temperatures and high pressures applied in a static way and for long periods.

Crystallite size of diamond was determined in each analysed sample using micro-XR powder diffraction and diamond of ~10 nm was found in AHS_209B and A135A samples and of ~30-40 nm in AHS_72; therefore, these results definitively show that diamonds in the analysed samples are nanometric. In addition, we must remark, that each sample here investigated show the presence of lonsdaleite, the defect stacking diamond, which a very typical feature of impact diamonds.

These results allow to discuss a possible explanation for the origin of diamond in ureilites.

The two favoured and possible explanations resulting from our study could be:

(a) Shock formation of diamonds from graphite shock, during shock events experienced by the ureilitic parent body;
(b) CVD of diamonds, which possibly occurred in the solar nebula before accreted to ureilitic parent body or the formation of diamonds can possible after a supernova explosion occurred near the ureilitic parent body (UPB).

These two explanations will then have to be inserted into the evolutionary history of the asteroid $2008TC_3$ (figure 6.1).

The diamonds and stacking disorder diamonds (lonsdaleite) are mixed in the graphite phase present in the samples, which are difficult to explain with a formation of diamond through CVD. These features and the nanometric crystallite size suggest that the diamond formation theory from graphite shock is the most consistent.

As reported before Visser et al. (2018) for static high pressure and temperature conditions, when carbonaceous material is heated, usually defect are lost and carbonaceous material organizes into a more ordered structure; however, if the increase in temperature and pressure are instantaneous, then the carbon phase may have features related to the disorder carbon. Instantaneous high temperatures and pressures events could cause an increase in the structural disorder of the graphite up to ta-C diamond defect (sp^3).

The temperatures obtained by Cody *equation (2)* for ureilitic parent body are a possible temperature range in upper mantle of a hypothetical urelitic parent body

and could have size similar or bigger than the Earth. However, the diamond nanometric crystallite size and the presence of lonsdaleite suggest an impact event of the parent body (or of the asteroid 2008TC_3) with another planetary object, which led to the formation of diamonds with nanometric crystallite size.

The shock event, consequent to the impact, was able to lead to the deformation of the graphite in ta-C defect diamond. Only the graphite that presented an I(D)/I(G) ratio greater than 0.7 underwent this change. The graphite present in the analyzed samples has an I(D)/I(G) ratio lower than 0.7 and probably did not have enough energy to continue the transformation into a ta-C defect diamond.

Finally, these results from AHS_209B, AHS_72 and A135A samples, consisting on the diamond data collected by micro-XR powder diffraction and micro-Raman spectroscopy of graphite phase collected by MRS, suggested that the formation of diamond could be better explained in terms of an impact event investing a pre-existing graphitic or carbonaceous material. Furthermore, as confirmed by Nemeth et al. (2014), the presence of stacking defect diamonds, lonsdaleite, is usually considered to be an asteroid impact marker.

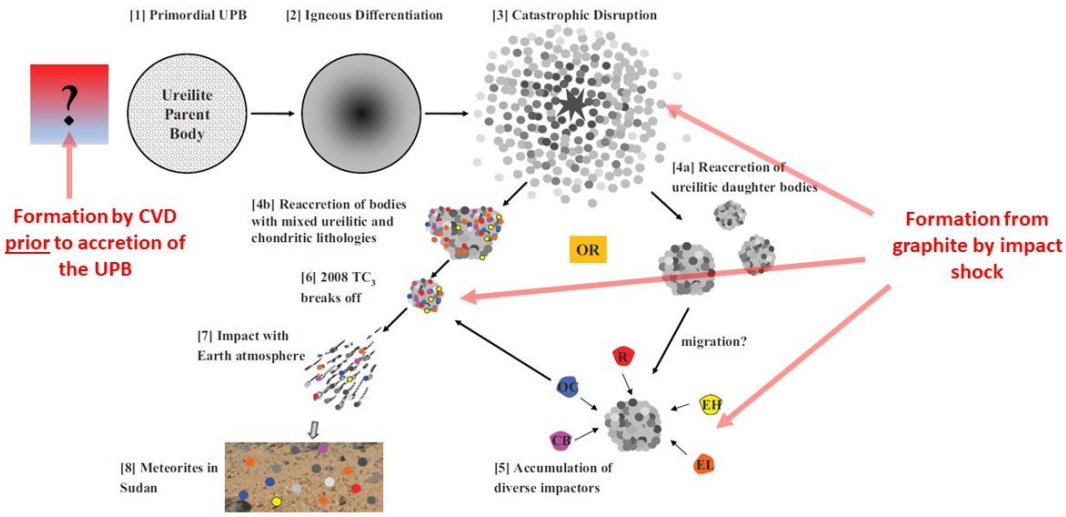

Figure 6.1 Schematic illustration of a possible formation scenario of the late-accreted, second scenario-ureilite asteroid, the break-off asteroid 2008 TC_3, and the origin of Almahata Sitta meteorite. In the figure are indicate the two possible theory proposed to diamond formation: **1)**Formation by CVD prior to accretion of UPB or **2)** Formation from graphite by impact shock (modified image of Horstmann and Bischoff, 2014).

The evolutionary history of this asteroid is schematically shown in figure 6.1. The formation of diamonds, due to impact shock of the graphite, may have occurred in different steps of the evolutionary history of $2008TC_3$ asteroid. The formation of diamonds, due to impact shock of graphite, may have occurred either due to a catastrophic destruction of the UPB, or following the destruction of the UPB due to the re-growth of the residual materials and to the impact of other ureilitic and chondritic objects.

The contribution to the increase of the integral breath and consequently the underestimation of the crystallite dimension of the diamond will have to be analysed. In detail, diamond stacking faults will have to be carried out to estimates the importance of the stacking disorder.

An important analysis for future purposes will be by Transmission Electron Microscopy (TEM) with the final aim to estimate the crystallite size of diamond. However, such crucial technique is destructive and more samples of Almahata Sitta should be available in a close future to carry out TEM analyses and directly confirm what it was possible to retrieve by diffraction in terms of crystallite size.

(7) References:

Beyssac, O., Goffé, B., Chopin, C. and Rouzaud, J. N.: Raman spectra of carbonaceous material in metasediments: A new geothermometer, J. Metamorph. Geol., 20(9), 859–871, doi:10.1046/j.1525-1314.2002.00408.x, 2002.

Bischoff, A., Horstmann, M., Pack, A., Laubenstein, M. and Haberer, S.: Asteroid 2008 TC3-Almahata Sitta: A spectacular breccia containing many different ureilitic and chondritic lithologies, Meteorit. Planet. Sci., 45(10–11), 1638–1656, doi:10.1111/j.1945-5100.2010.01108.x, 2010.

Brey, G. P. and Kohler, T.: Geothermobarometry in 4-phase lherzolites .2. New thermobarometers, and practical assessment of existing thermobarometers, J. Petrol., 31(6), 1353–1378, doi:10.1093/petrology/31.6.1353, 1990.

Busemann, H., Alexander, C. M. O. D. and Nittler, L. R.: Characterization of insoluble organic matter in primitive meteorites by microRaman spectroscopy, Meteorit. Planet. Sci., 42(7–8), 1387–1416, doi:10.1111/j.1945-5100.2007.tb00581.x, 2007.

Cody, G. D., Alexander, C. M. O. D., Yabuta, H., Kilcoyne, A. L. D., Araki, T., Ade, H., Dera, P., Fogel, M., Militzer, B. and Mysen, B. O.: Organic thermometry for chondritic parent bodies, Earth Planet. Sci. Lett., 272(1–2), 446–455, doi:10.1016/j.epsl.2008.05.008, 2008.

Delhez, R., de Keijser, T. H. and Mittemeijer, E. J.: Determination of crystallite size and lattice distortions through X-ray diffraction line profile analysis, Fresenius Z. Anal. Chem., 312(1), 1–16, 1982.

Ferrari, A. C. and Robertson, J.: Interpretation of \textsc{R}aman spectra of disordered and amorphous carbon, Phys. Rev. B, 61(20), 95–107, 2000.

Frondel, C. and Marvin, U. B.: Lonsdaleite, a hexagonal polymorph of diamond [4], Nature, 214(5088), 587–589, doi:10.1038/214587a0, 1967.

Fukunaga, K., Matsuda, J., Nagao, K., Miyamoto, M. and Ito, K.: Noble-gas enrichment in vapour-growth diamonds and the origin of diamonds in ureilite, Nature, 329, 855–857, doi:10.1038/328141a0, 1987.

Göbel, R., Ott, U. and Begemann, F.: On Trapped Noble Gases in Ureilites, J. Geophys. Res., 83(B2), 855–867, doi:10.1029/JB083iB02p00855, 1978.

Goodrich, C. A.: Invited Review Ureilites : A critical review, Meteorit. Soc., 352, 327–352 [online] Available from: http://link.springer.com/10.1007/978-3-319-65179-8, 1992.

GP Vdovykin: Ureilites, Space Sci. Rev., 10, 483–510, 1970.

Herrin, J. S., Zolensky, M. E., Ito, M., Le, L., Mittlefehldt, D. W., Jenniskens, P., Ross, A. J. and Shaddad, M. H.: Thermal and fragmentation history of ureilitic asteroids: Insights from the Almahata Sitta fall, Meteorit. Planet. Sci., 45(10–11), 1789–1803, doi:10.1111/j.1945-5100.2010.01136.x, 2010.

Horstmann, M. and Bischoff, A.: The Almahata Sitta polymict breccia and the late accretion of asteroid 2008 TC3, Chemie der Erde, 74(2), 149–183, doi:10.1016/j.chemer.2014.01.004, 2014.

Jenniskens, P., Shaddad, M. H., Numan, D., Elsir, S., Kudoda, A. M., Zolensky, M. E., Le, L., Robinson, G. A., Friedrich, J. M., Rumble, D., Steele, A., Chesley, S. R., Fitzsimmons, A., Duddy, S., Hsieh, H. H., Ramsay, G., Brown, P. G., Edwards, W. N., Tagliaferri, E., Boslough, M. B., Spalding, R. E., Dantowitz, R., Kozubal, M., Pravec, P., Borovicka, J., Charvat, Z., Vaubaillon, J., Kuiper, J., Albers, J., Bishop, J. L., Mancinelli, R. L., Sandford, S. A., Milam, S. N., Nuevo, M. and Worden, S. P.: The impact and recovery of asteroid 2008 TC3, Nature, 458(7237), 485–488, doi:10.1038/nature07920, 2009.

Jenniskens, P., Vaubaillon, J., Binzel, R. P., Demeo, F. E., Nesvorný, D., Bottke, W. F., Fitzsimmons, A., Hiroi, T., Marchis, F., Bishop, J. L., Vernazza, P., Zolensky, M. E., Herrin, J. S., Welten, K. C., Meier, M. M. M. and Shaddad, M. H.: Almahata Sitta (=asteroid 2008 TC3) and the search for the ureilite parent body, Meteorit. Planet. Sci., 45(10–11), 1590–1617, doi:10.1111/j.1945-5100.2010.01153.x, 2010.

Kretz, R.: Transfer and exchange equilibria in a portion of the pyroxene quadrilateral as

deduced from natural and experimental data, Geochim. Cosmochim. Acta, 46(3), 411–421, doi:10.1016/0016-7037(82)90232-0, 1982.

Langford, J. I. and Wilson, A. J. C.: Scherrer after sixty years: A survey and some new results in the determination of crystallite size, J. Appl. Crystallogr., 11(2), 102–113, doi:10.1107/S0021889878012844, 1978.

Lewis, R. S., Ming, T., Wacker, J. F., Anders, E. and Steel, E.: Interstellar diamonds in meteorites, Nature, 326(6109), 160–162, doi:10.1038/326160a0, 1987.

Lipschutz, M. E. et al.: Origin of Diamonds in the Ureilites, Science (80-.)., 143(3613)(4), 1431–1434, 1964.

Matsuda, J. I., Kusumi, A., Yajima, H. and Syono, Y.: Noble gas studies in diamonds synthesized by shock loading in the laboratory and their implications on the origin of diamonds in ureilites, Geochim. Cosmochim. Acta, 59(23), 4939–4949, doi:10.1016/0016-7037(95)00333-9, 1995.

Miranda, M. A. R. and Sasaki, J. M.: The limit of application of the Scherrer equation, Acta Crystallogr. Sect. A Found. Adv., 74(1), 54–65, doi:10.1107/S2053273317014929, 2018.

Mittlefehldt, D. W., McCoy, T. J., Goodrich, C. A. and Kracher, A.: Non-chondritic meteorites from asteroidal bodies, Planet. Mater., (1988), 4-001-4–196, doi:10.1007/978-1-59745-060-7, 1998.

Miyahara, M., Ohtani, E., El Goresy, A., Lin, Y., Feng, L., Zhang, J. C., Gillet, P., Nagase, T., Muto, J. and Nishijima, M.: Unique large diamonds in a ureilite from Almahata Sitta 2008 TC<inf>3</inf> asteroid, Geochim. Cosmochim. Acta, 163, 14–26, doi:10.1016/j.gca.2015.04.035, 2015.

Nabiei, F., Badro, J., Dennenwaldt, T., Oveisi, E., Cantoni, M., Hébert, C., El Goresy, A., Barrat, J.-A. and Gillet, P.: A large planetary body inferred from diamond inclusions in a ureilite meteorite, Nat. Commun., 9(1), 1327, doi:10.1038/s41467-018-03808-6, 2018.

Nakamuta, Y., Kitajima, F. and Shimada, K.: In situ observation, X–ray diffraction and Raman analyses of carbon minerals in ureilites: Origin and formation mechanisms of diamond in ureilites, J. Mineral. Petrol. Sci., 111(4), 252–269, doi:10.2465/jmps.150906,

2016.

Nemeth, P., Garvie, L. A. J., Aoki, T., Dubrovinskaia, N., Dubrovinsky, L. and Buseck, P. R.: Lonsdaleite is faulted and twinned cubic diamond and does not exist as a discrete material, Nat. Commun., 5(May), 1–5, doi:10.1038/ncomms6447, 2014.

Patterson, A. L.: The scherrer formula for X-ray particle size determination, Phys. Rev., 56(10), 978–982, doi:10.1103/PhysRev.56.978, 1939.

Ross, A. J., Steele, A., Fries, M. D., Kater, L., Downes, H., Jones, A. P., Smith, C. L., Jenniskens, P. M., Zolensky, M. E. and Shaddad, M. H.: MicroRaman spectroscopy of diamond and graphite in Almahata Sitta and comparison with other ureilites, Meteorit. Planet. Sci., 46(3), 364–378, doi:10.1111/j.1945-5100.2010.01157.x, 2011.

Rossi, A. P.: Planetary Geology, Springer., edited by A. P. Rossi and S. Van Gasselt., 2018.

Salzmann, C. G., Murray, B. J. and Shephard, J. J.: Extent of stacking disorder in diamond, Diam. Relat. Mater., 59, 69–72, doi:10.1016/j.diamond.2015.09.007, 2015.

Shaddad, M. H., Jenniskens, P., Numan, D., Kudoda, A. M., Elsir, S., Riyad, I. F., Ali, A. E., Alameen, M., Alameen, N. M., Eid, O., Osman, A. T., Abubaker, M. I., Yousif, M., Chesley, S. R., Chodas, P. W., Albers, J., Edwards, W. N., Brown, P. G., Kuiper, J. and Friedrich, J. M.: The recovery of asteroid 2008 TC3, Meteorit. Planet. Sci., 45(10–11), 1557–1589, doi:10.1111/j.1945-5100.2010.01116.x, 2010.

Stöffler, D., Keil, K. and Edward R.D, S.: Shock metamorphism of ordinary chondrites, Geochim. Cosmochim. Acta, 55(12), 3845–3867, doi:10.1016/0016-7037(91)90078-J, 1991.

Takeda, H., Mori, H. and Ogata, H.: Mineralogy of augite-bearing ureilites and the origin of their chemical trends, Meteoritics, 24(2), 73–81, doi:10.1111/j.1945-5100.1989.tb00947.x, 1989.

Tuinstra, F. and Koenig, J. L.: Raman Spectrum of Graphite, J. Chem. Phys., 53(3), 1126–1130, doi:10.1063/1.1674108, 1970.

Urey, H. C.: Diamonds, meteorites, and the origin of the solar system, , 623–637, 1956.

Visser, R., John, T., Menneken, M., Patzek, M. and Bischoff, A.: ScienceDirect Temperature constraints by Raman spectroscopy of organic matter in volatile-rich clasts and carbonaceous chondrites, Geochim. Cosmochim. Acta, 241, 38–55, doi:10.1016/j.gca.2018.08.037, 2018.

Warren, P. H. and Rubin, A. E.: Pyroxene-selective impact smelting in ureilites, Geochim. Cosmochim. Acta, 74(17), 5109–5133, doi:10.1016/j.gca.2010.05.026, 2010.

Weisberg, M. K., Smith, C., Benedix, G., Herd, C. D. K., Righter, K., Haack, H., Yamaguchi, A., Chennaoui Aoudjehane, H. and Grossman, J. N.: The meteoritical bulletin, No. 97, Meteorit. Planet. Sci., 45(3), 449–493, doi:10.1111/j.1945-5100.2010.01036.x, 2010.

Zolensky, M., Herrin, J., Mikouchi, T., Ohsumi, K., Friedrich, J., Steele, A., Rumble, D., Fries, M., Sandford, S., Milam, S., Hagiya, K., Takeda, H., Satake, W., Kurihara, T., Colbert, M., Hanna, R., Maisano, J., Ketcham, R., Goodrich, C., Le, L., Robinson, G. A., Martinez, J., Ross, K., Jenniskens, P. and Shaddad, M. H.: Mineralogy and petrography of the Almahata Sitta ureilite, Meteorit. Planet. Sci., 45(10–11), 1618–1637, doi:10.1111/j.1945-5100.2010.01128.x, 2010.

(8) APPENDIXES

Appendix A: EDS analysis

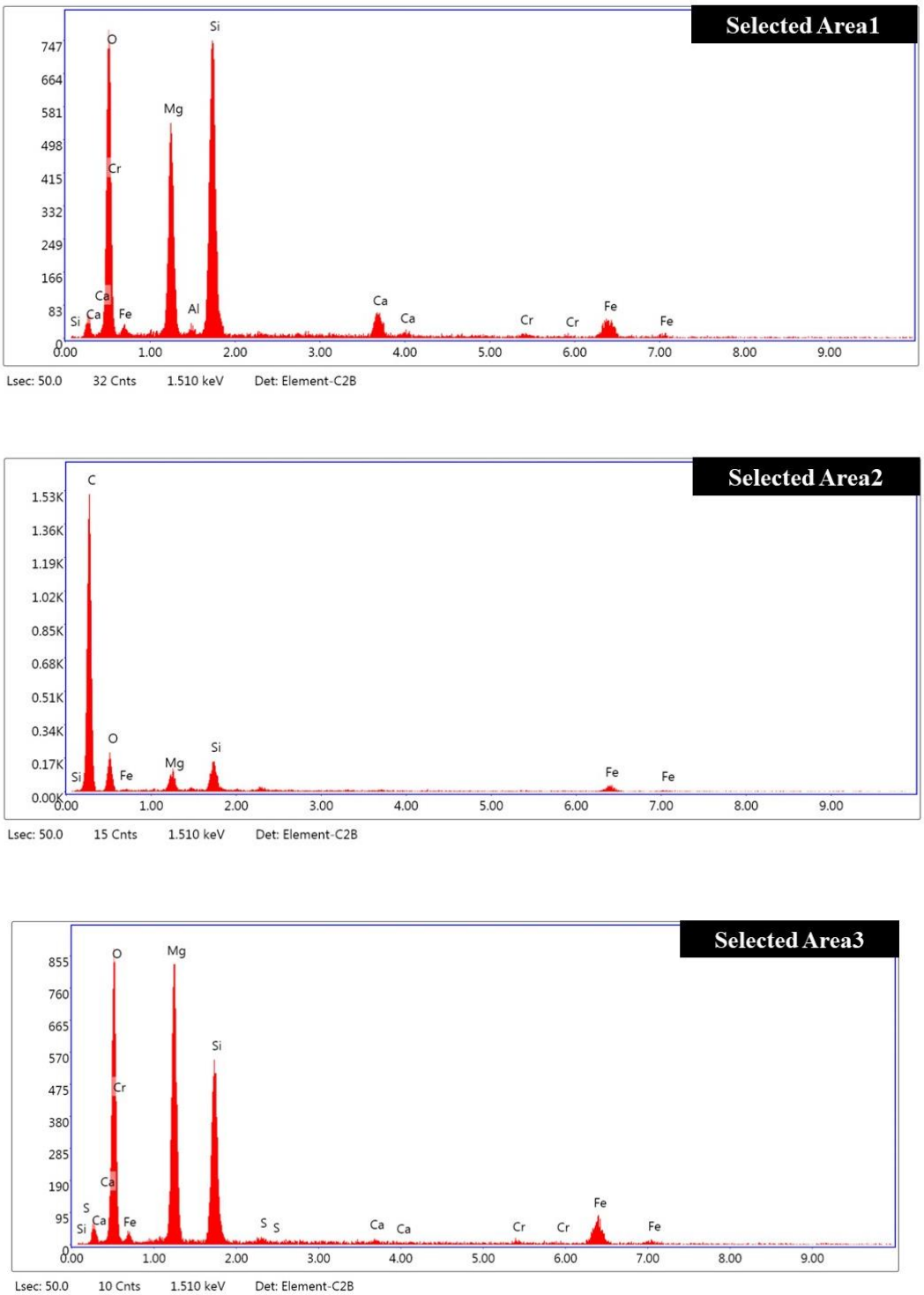

Figure A1) EDS areal spectra analysis of selected Areas of A135A sample which report the semi-quantitative chemical composition of selected Area 1, selected Area 2, selected Area3 referred to figure

Tab.A1) The data acquired by EDS analyses referred to figure 1) selected Area1 of figure 5.5:

Element	Weight %	Atomic %	Net Int.	Error %	K ratio	Z	A	F
O K	41.09	56.21	100.99	9.11	0.1634	1.0651	0.3732	1.0000
Mg K	19.04	17.14	82.17	7.07	0.1093	0.9858	0.5810	1.0024
AlK	0.53	0.43	2.13	48.03	0.0028	0.9496	0.5616	1.0044
SiK	26.05	20.30	129.86	5.66	0.1735	0.9707	0.6849	1.0017
CaK	4.44	2.43	13.85	10.19	0.0391	0.9174	0.9410	1.0192
Cr K	0.86	0.36	1.94	48.92	0.0075	0.8233	0.9885	1.0726
Fe K	7.98	3.13	13.84	11.32	0.0678	0.8185	0.9981	1.0397

Tab.A2) The data acquired by EDS analyses referred to figure 1) selected Area2 of figure 5.5:

Element	Weight %	Atomic %	Net Int.	Error %	K ratio	Z	A	F
C K	73.90	81.17	174.80	6.64	0.4127	1.0181	0.5486	1.0000
O K	19.01	15.68	20.63	15.12	0.0282	0.9728	0.1523	1.0000
Mg K	2.35	1.28	12.70	10.75	0.0143	0.8969	0.6751	1.0026
SiK	3.25	1.53	22.54	7.17	0.0254	0.8821	0.8824	1.0042
Fe K	1.49	0.35	3.13	45.64	0.0129	0.7408	1.0205	1.1506

Tab. A3) The data acquired by EDS analyses referred to figure1) selected Area3 of figure 5.5:

Element	Weight %	Atomic %	Net Int.	Error %	K ratio	Z	A	F
O K	37.32	51.71	110.29	8.32	0.1779	1.0697	0.4456	1.0000
Mg K	29.76	27.14	130.52	6.60	0.1732	0.9902	0.5865	1.0016
SiK	20.12	15.88	92.26	6.82	0.1229	0.9751	0.6255	1.0015
S K	0.30	0.21	1.20	90.54	0.0021	0.9554	0.7175	1.0046
CaK	0.49	0.27	1.54	67.35	0.0043	0.9216	0.9384	1.0242
Cr K	0.67	0.29	1.57	63.66	0.0060	0.8272	0.9939	1.0919
Fe K	11.34	4.50	19.80	9.28	0.0967	0.8223	1.0017	1.0358

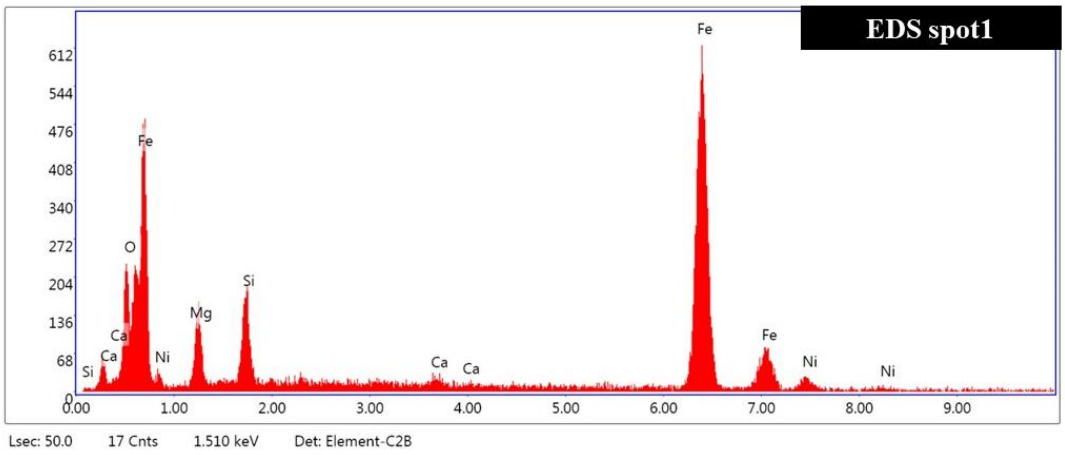
EDS spot1
612
544
476
408
340
272
204
136
68
0
Fe
O
Si
Mg
Ca
Ca
Ni
Ca
Ca
Fe
Ni
Ni
0.00
1.00
2.00
3.00
4.00
5.00
6.00
7.00
8.00
9.00
Lsec: 50.0
17 Cnts
1.510 keV
Det: Element-C2B

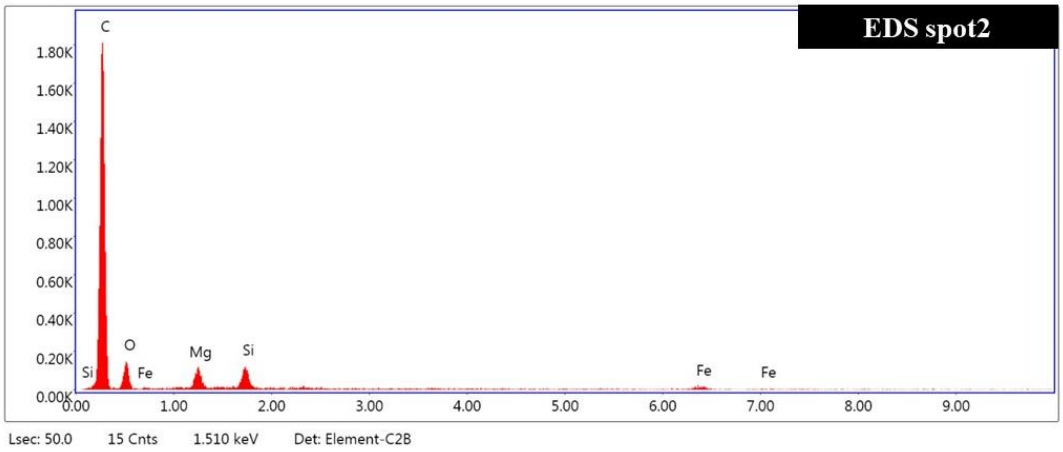
EDS spot2
1.80K
1.60K
1.40K
1.20K
1.00K
0.80K
0.60K
0.40K
0.20K
0.00K
C
O
Si
Fe
Mg
Si
Fe
Fe
0.00
1.00
2.00
3.00
4.00
5.00
6.00
7.00
8.00
9.00
Lsec: 50.0
15 Cnts
1.510 keV
Det: Element-C2B

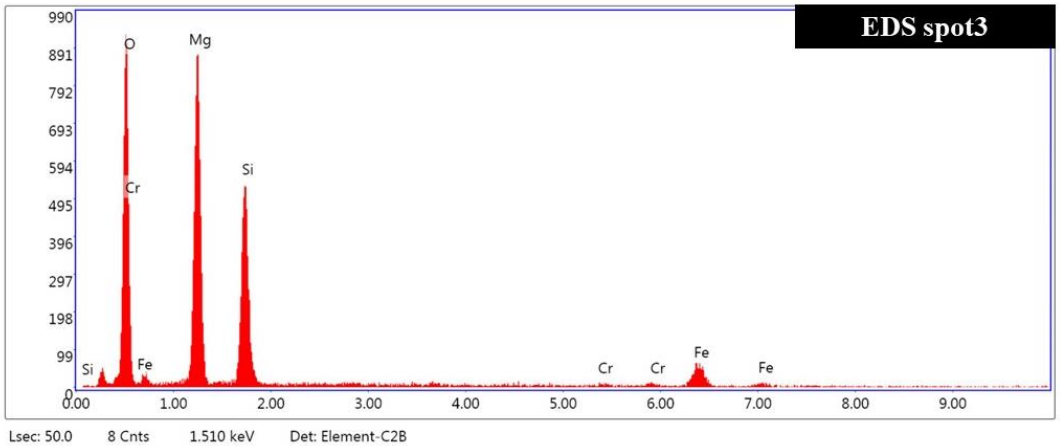
EDS spot3
990
891
792
693
594
495
396
297
198
99
0
O
Mg
Cr
Si
Si
Fe
Cr
Cr
Fe
Fe
0.00
1.00
2.00
3.00
4.00
5.00
6.00
7.00
8.00
9.00
Lsec: 50.0
8 Cnts
1.510 keV
Det: Element-C2B

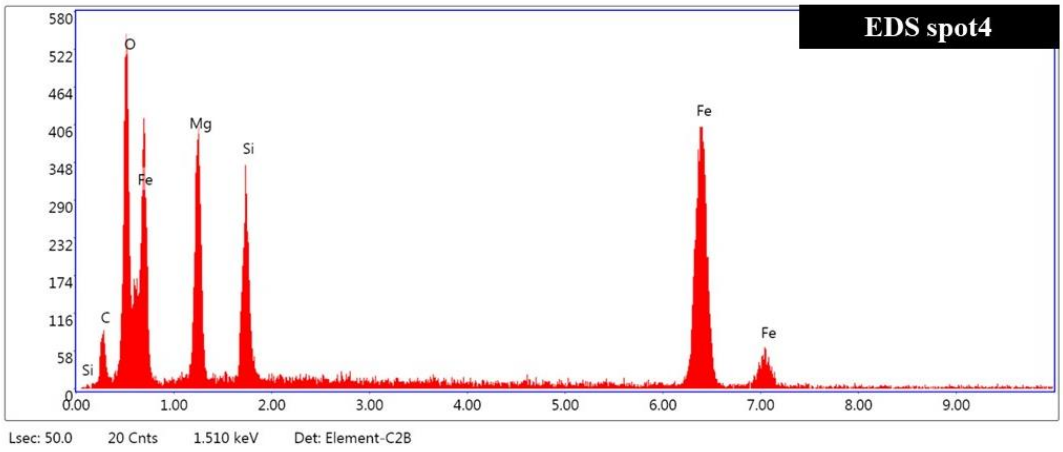

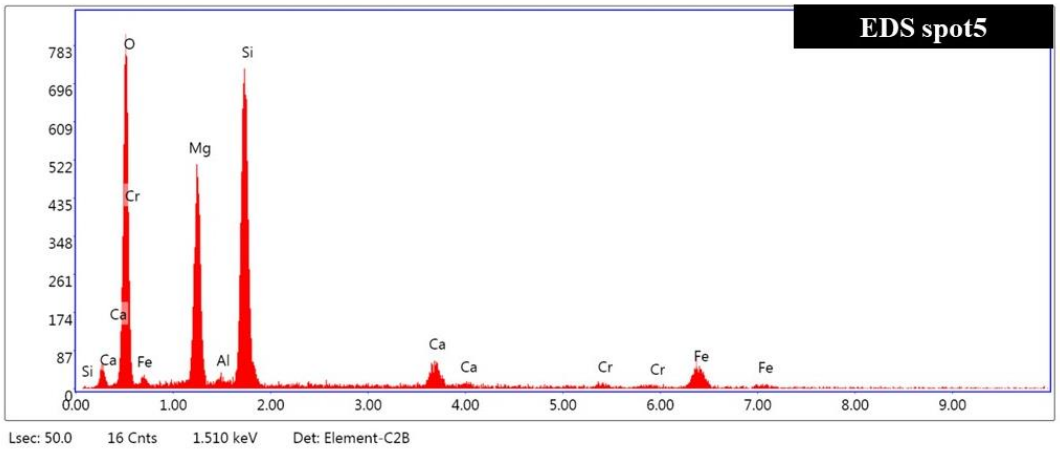

Figure A2) EDS punctual analysis of A135A samples, which report the semi-quantitative chemical composition of spot1, spot2, spot3, spot4 and spot5 referred to figure 5.5

Tab.A4) The data collected by EDS punctual analyses referred to figure 2) EDS spot1 of figure 5.5:

Element	Weight %	Atomic %	Net Int.	Error %	K ratio	Z	A	F
O K	7.58	19.76	28.69	10.25	0.0426	1.2162	0.4625	1.0000
Mg K	7.00	12.02	19.67	13.91	0.0240	1.1315	0.3030	1.0009
Si K	5.82	8.64	28.05	10.65	0.0344	1.1166	0.5283	1.0027
Ca K	0.78	0.81	3.08	40.86	0.0080	1.0612	0.9335	1.0365
Fe K	75.35	56.30	160.56	2.91	0.7223	0.9528	0.9994	1.0067
Ni K	3.48	2.47	5.41	24.00	0.0313	0.9645	0.9265	1.0078

Tab.A5) The data collected by EDS punctual analyses referred to figure 2) EDS spot2 of figure 5.5:

Element	Weight %	Atomic %	Net Int.	Error %	K ratio	Z	A	F
C K	79.45	85.68	219.15	5.92	0.4898	1.0148	0.6075	1.0000
O K	14.34	11.61	15.33	16.61	0.0198	0.9695	0.1425	1.0000
Mg K	2.49	1.33	14.49	10.25	0.0154	0.8939	0.6910	1.0025
Si K	2.26	1.04	16.67	8.16	0.0178	0.8791	0.8910	1.0046
Fe K	1.45	0.34	3.24	26.64	0.0127	0.7382	1.0210	1.1583

Tab.A6) The data collected by EDS punctual analyses referred to figure 2) EDS spot3 of figure 5.5:

Element	Weight %	Atomic %	Net Int.	Error %	K ratio	Z	A	F
O K	38.59	52.56	118.15	7.91	0.1901	1.0657	0.4622	1.0000
Mg K	31.49	28.22	140.84	6.32	0.1864	0.9862	0.5993	1.0016
SiK	19.51	15.14	88.84	6.81	0.1181	0.9711	0.6222	1.0014
Cr K	0.91	0.38	2.12	28.49	0.0081	0.8235	0.9952	1.0892
Fe K	9.50	3.71	16.64	8.51	0.0811	0.8186	1.0022	1.0402

Tab.A7) The data collected by EDS punctual analyses referred to figure 2) EDS spot4 of figure 5.5:

Element	Weight %	Atomic %	Net Int.	Error %	K ratio	Z	A	F
C K	7.60	17.30	8.10	18.24	0.0172	1.1798	0.1916	1.0000
O K	19.46	33.26	75.02	8.73	0.0920	1.1335	0.4173	1.0000
Mg K	15.36	17.28	62.69	9.43	0.0633	1.0525	0.3911	1.0010
SiK	8.17	7.96	48.36	8.52	0.0490	1.0377	0.5765	1.0024
Fe K	49.42	24.20	118.40	3.27	0.4400	0.8807	1.0038	1.0070

Tab.A8) The data collected by EDS punctual analyses referred to figure 2) EDS spot5 of figure 5.5:

Element	Weight %	Atomic %	Net Int.	Error %	K ratio	Z	A	F
O K	41.71	56.95	102.81	9.10	0.1672	1.0650	0.3765	1.0000
Mg K	18.60	16.71	79.11	7.17	0.1058	0.9857	0.5761	1.0023
AlK	0.64	0.51	2.54	37.61	0.0034	0.9495	0.5617	1.0043
SiK	25.45	19.80	126.08	5.69	0.1694	0.9706	0.6843	1.0018
CaK	4.45	2.42	13.80	10.17	0.0392	0.9173	0.9420	1.0195
Cr K	0.92	0.39	2.07	46.01	0.0080	0.8233	0.9888	1.0733
Fe K	8.24	3.22	14.20	10.46	0.0700	0.8185	0.9982	1.0390

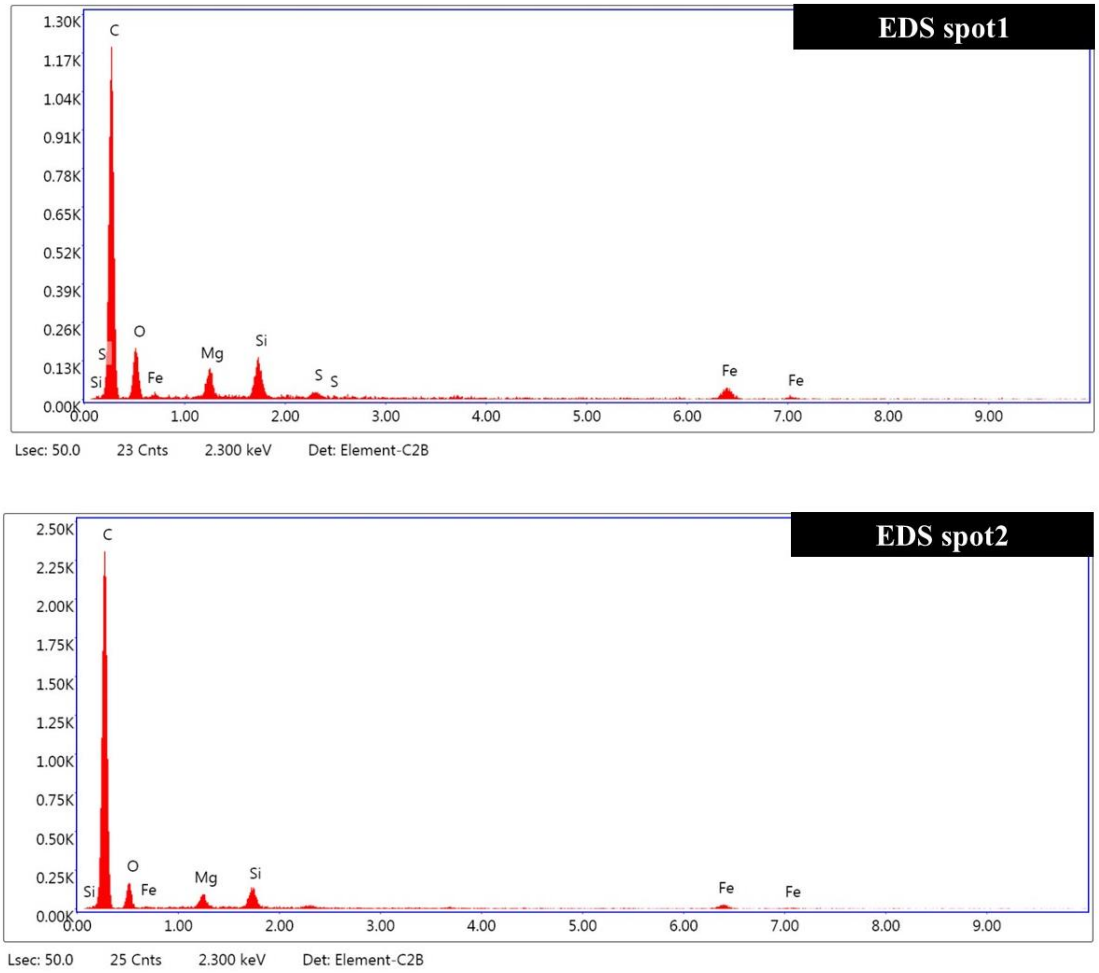

Figure A3) EDS punctual analysis of A135A samples, which report the semi-quantitative chemical composition of spot1 and spot2 referred to figure 5.7

Tab. A9) The data collected by EDS punctual analyses referred to figure 3) EDS spot1 of figure 5.7

Element	Weight %	Atomic %	Net Int.	Error %	K ratio	Z	A	F
C K	71.74	79.83	138.74	7.08	0.3822	1.0211	0.5217	1.0000
O K	19.89	16.62	19.02	15.57	0.0303	0.9758	0.1561	1.0000
Mg K	2.47	1.36	11.25	13.50	0.0147	0.9000	0.6617	1.0024
SiK	3.05	1.45	17.96	8.71	0.0236	0.8852	0.8723	1.0044
S K	0.34	0.14	1.64	66.70	0.0028	0.8665	0.9576	1.0104
Fe K	2.51	0.60	4.41	32.80	0.0213	0.7436	1.0201	1.1157

Tab. A10) The data collected by EDS punctual analyses referred to figure 3) EDS spot2 of figure 5.7

Element	Weight %	Atomic %	Net Int.	Error %	K ratio	Z	A	F
C K	81.44	86.92	281.32	5.41	0.5332	1.0126	0.6466	1.0000
O K	13.77	11.03	16.96	16.53	0.0186	0.9673	0.1396	1.0000
Mg K	1.55	0.82	10.72	13.30	0.0097	0.8917	0.6955	1.0026
SiK	2.16	0.99	19.00	8.39	0.0172	0.8769	0.9031	1.0049
Fe K	1.08	0.25	2.89	49.80	0.0096	0.7363	1.0215	1.1830

Appendix B: Micro-Raman Spectroscopy analysis

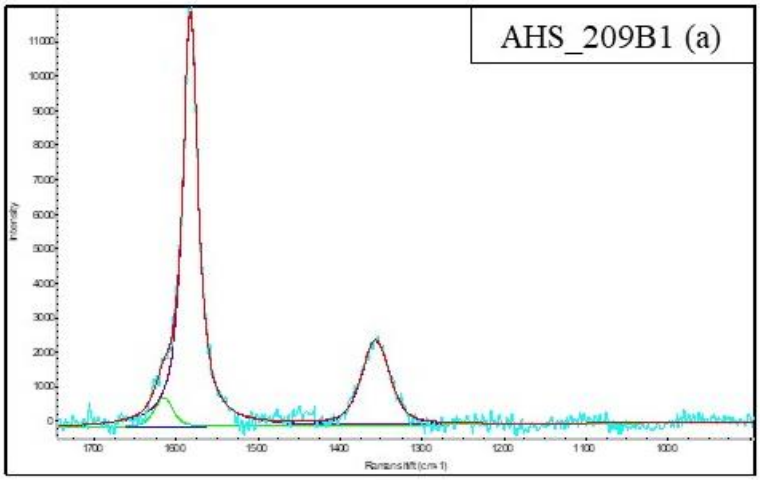

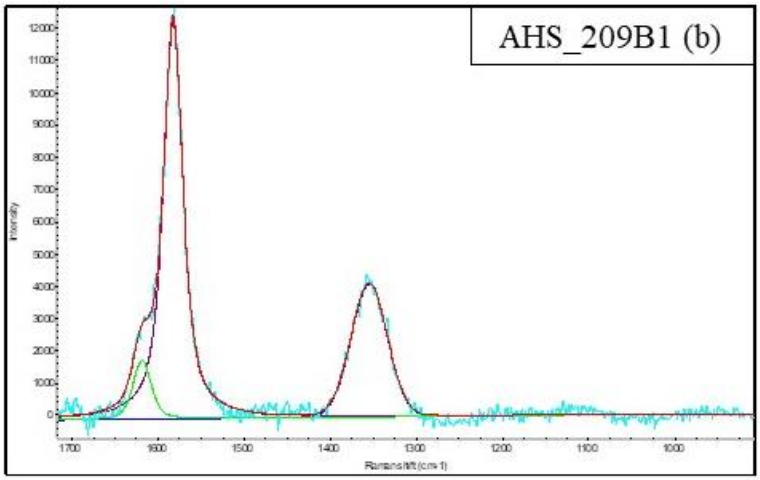

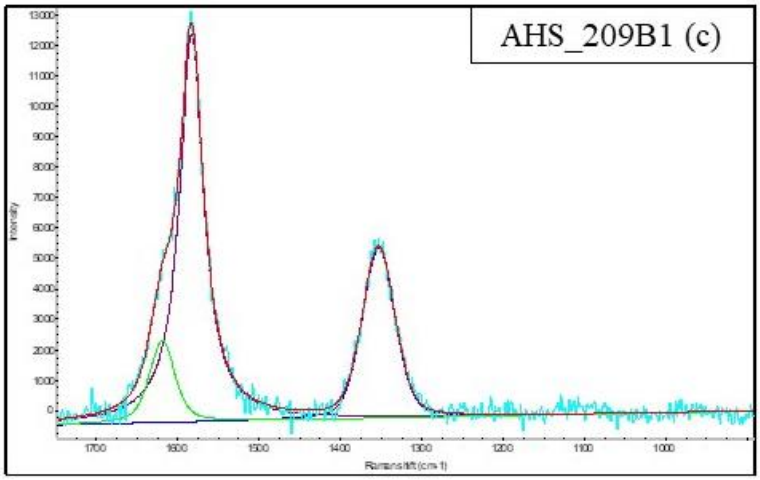

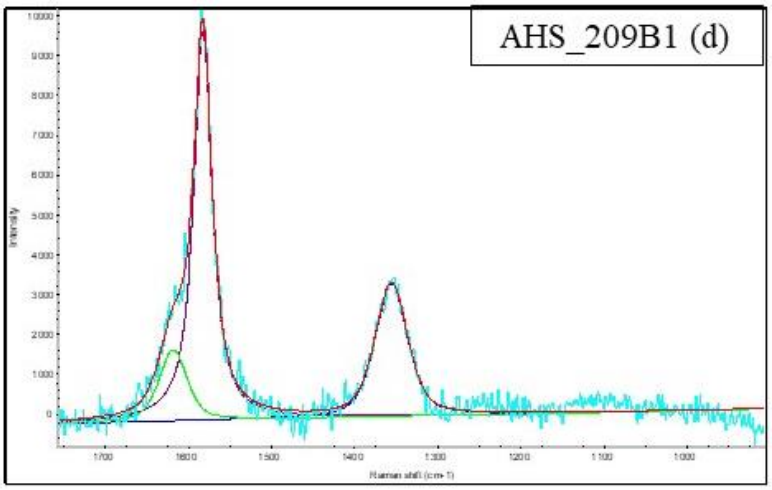

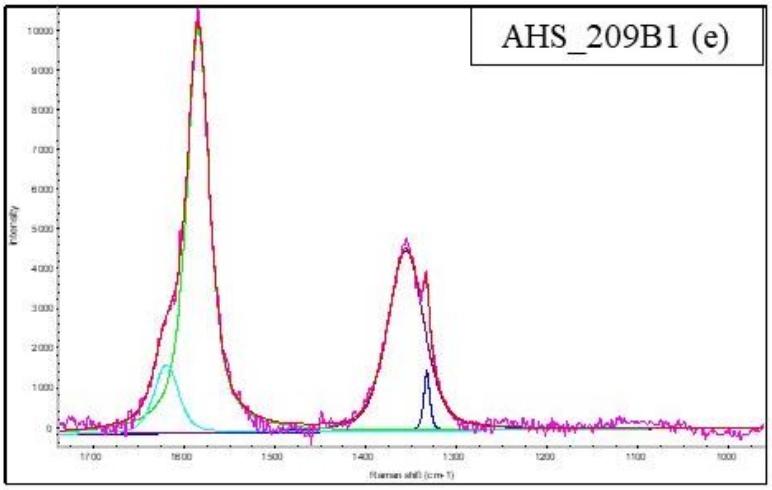

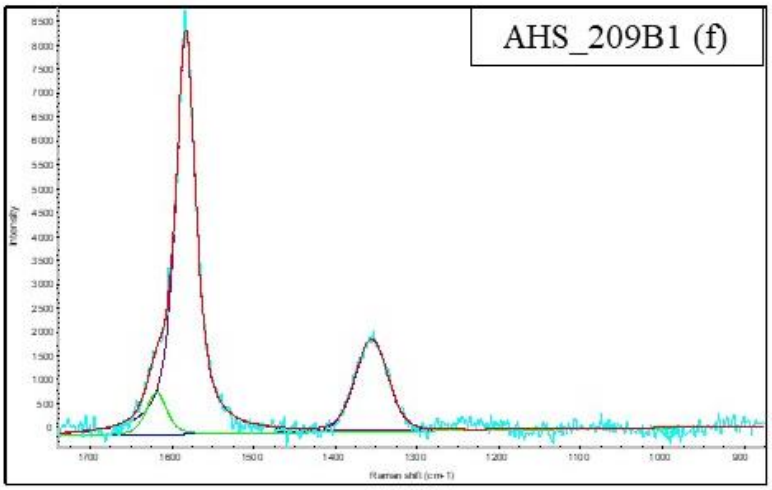

Figures B 1) Raman spectrum of AHS_209B1 sample: Raman acquisition (a), (b), (c), (d), (e) and (f)

Tab B1) Data collected during fit peaks of Raman spectrum of AHS_209B1 samples in (a) acquisition (50x mag;514nm):

AHS_ 209B1 (a)					
Peak	**Center**	**Height**	**FWHM**	**Other**	**Area**
1	1355.7	2452.6	40.6	0.5595	127900.7
2	1582.0	12057.2	22.2	0.1444	399714.9
3	1614.7	852.7	25.9	0.5276	28729.46

Tab B2) Data collected during fit peaks of Raman spectrum of AHS_209B1 samples in (b) acquisition (50x mag; 514nm):

AHS_ 209B1 (b)					
Peak	**Center**	**Height**	**FWHM**	**Other**	**Area**
1	1353.7	4133.3	49.2	0.9579	220935.3
2	1581.8	12473.3	26.7	0.2552	479647
3	1617.8	1829.3	24.8	0.5872	57747.14

Tab B3) Data collected during fit peaks of Raman spectrum of AHS_209B1 samples in (c) acquisition (50x mag; 514nm):

AHS_ 209B1 (c)					
Peak	**Center**	**Height**	**FWHM**	**Other**	**Area**
1	1352.4	5605.4	47.2	0.7183	318675.3
2	1582.6	12780.0	35.5	-0.0037	710620.9
3	1618.7	2718.9	36.6	0.4943	130970.9

Tab B4) Data collected during fit peaks of Raman spectrum of AHS_209B1 samples in (d) acquisition (50x mag; 514nm):

AHS_ 209B1 (d)					
Peak	**Center**	**Height**	**FWHM**	**Other**	**Area**
1	1355.0	3344.9	46.2	0.5187	201393.9
2	1582.0	9795.6	26.8	0.1078	397684.4
3	1617.9	1795.4	39.9	0.4937	94432.26

Tab B5) Data collected during fit peaks of Raman spectrum of AHS_209B1 samples in (e) acquisition (50x mag; 514nm):

AHS_ 209B1 (e)					
Peak	**Center**	**Height**	**FWHM**	**Other**	**Area**
1	1331.8	1574.1	7.5	0.4909	15658.44
2	1354.8	4561.3	46.9	0.6364	266359.3
3	1583.6	10235.9	30.1	0.284	438746.2
4	1618.7	1741.1	31.5	0.5545	70515.53

Tab B6) Data collected during fit peaks of Raman spectrum of AHS_209B1 samples in (f) acquisition (50x mag; 514nm):

AHS_ 209B1 (f)					
Peak	**Center**	**Height**	**FWHM**	**Other**	**Area**
1	1354.9	1920.1	46.7	0.8388	102706
2	1582.5	8420.1	29.0	0.2495	351800.4
3	1618.4	887.8	28.7	0.5821	32555.55

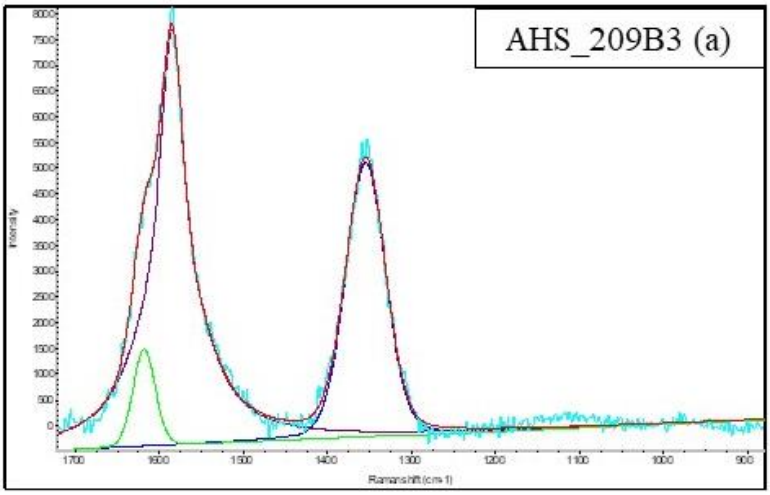
AHS_209B3 (a)
Intensity
Raman shift (cm-1)

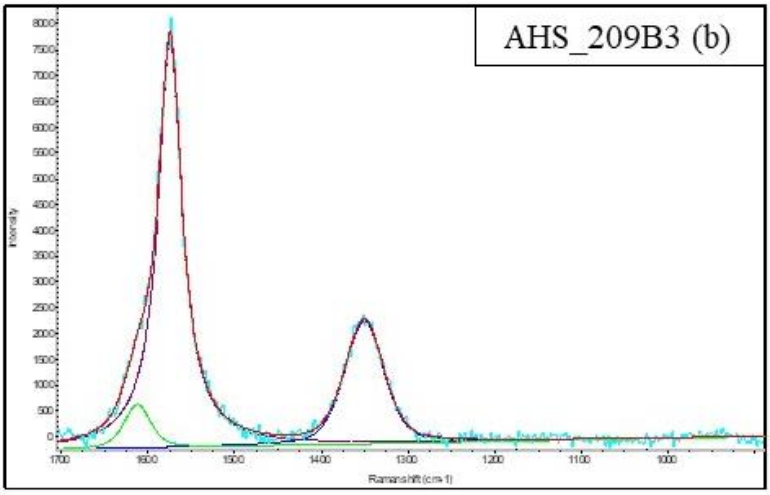
AHS_209B3 (b)
Intensity
Raman shift (cm-1)

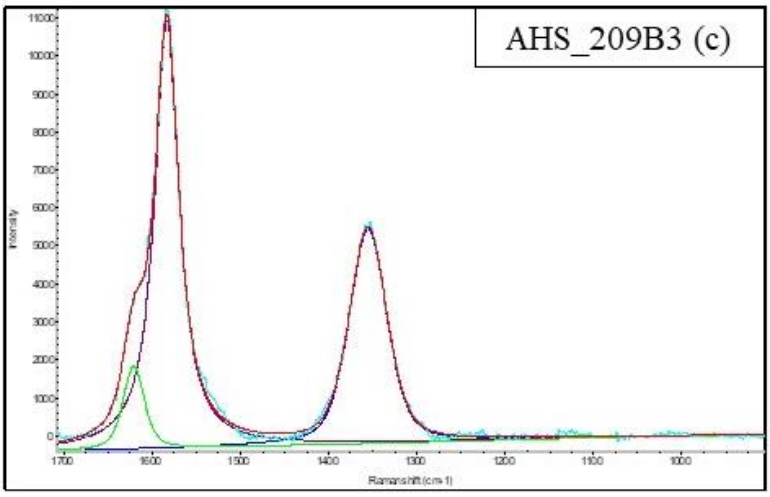
AHS_209B3 (c)
Intensity
Raman shift (cm-1)

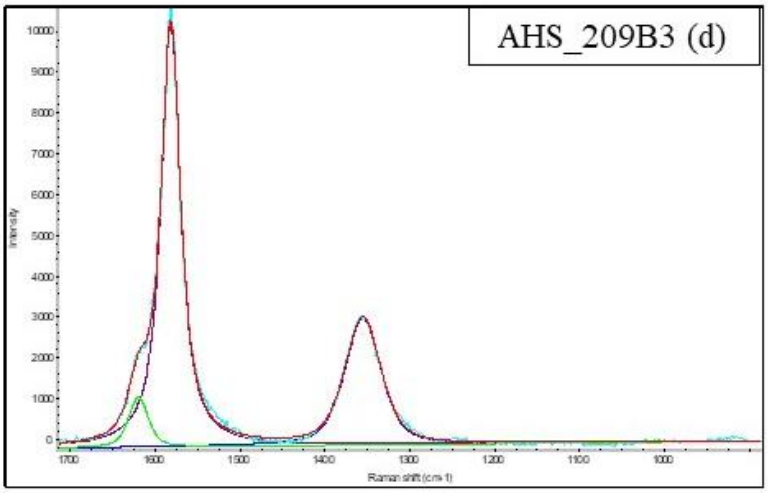

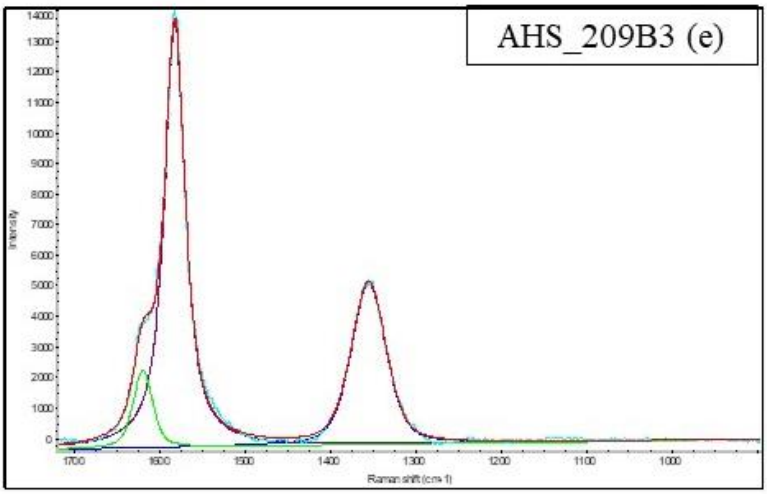

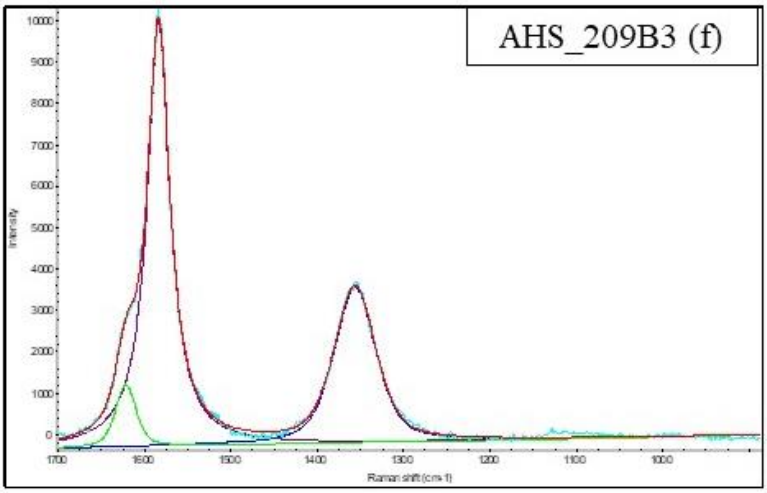

Figures B 2) Raman spectrum of AHS_209B3 sample: Raman acquisition (a), (b), (c), (d), (e) and (f)

Tab B7) Data collected during fit peaks of Raman spectrum of AHS_209B3 samples in (a) acquisition (50x mag; 514nm):

AHS_ 209B3 (a)					
Peak	**Center**	**Height**	**FWHM**	**Other**	**Area**
1	1353.9	5334.7	55.5315	0.8402	338898.4
2	1584.7	8078.1	44.9985	-0.471	653892.2
3	1617.8	1892.4	30.9	0.9103	65004.1

Tab B8) Data collected during fit peaks of Raman spectrum of AHS_209B3 samples in (b) acquisition (50x mag; 514nm):

AHS_ 209B3 (b)					
Peak	**Center**	**Height**	**FWHM**	**Other**	**Area**
1	1349.6	2381.8	53.2	0.6205	158753
2	1573.8	7976.3	33.4	-0.0686	426079.3
3	1611.4	841.2	36.2	0.5236	39658.77

Tab B9) Data collected during fit peaks of Raman spectrum of AHS_209B3 samples in (c) acquisition (50x mag; 514nm):

AHS_ 209B3 (c)					
Peak	**Center**	**Height**	**FWHM**	**Other**	**Area**
1	1354.5	5652.6	50.1873	0.5854	360516.8
2	1582.7	11272.8	33.3198	0.0501	578409.1
3	1620.3	2191.8	28.3535	0.499	81762.17

Tab B10) Data collected during fit peaks of Raman spectrum of AHS_209B3 samples in (d) acquisition (50x mag; 514nm):

AHS_ 209B3 (d)					
Peak	**Center**	**Height**	**FWHM**	**Other**	**Area**
1	1354.8	3120.9	50.4	0.5062	206073.4
2	1581.2	10375.3	27.6	0.1063	433157.2
3	1619.6	1231.6	27.6	0.5009	44660.77

Tab B11) Data collected during fit peaks of Raman spectrum of AHS_209B3 samples in (e) acquisition (50x mag; 514nm):

AHS_ 209B3 (e)					
Peak	**Center**	**Height**	**FWHM**	**Other**	**Area**
1	1354.9	5293.1	48.1	0.601	321808.4
2	1582.8	13890.45	29.1	0.1311	605128.1
3	1620.3	2558.4	26.9	0.5058	90491.07

Tab B12) Data collected during fit peaks of Raman spectrum of AHS_209B3 samples in (f) acquisition (50x mag; 514nm):

AHS_ 209B3 (f)					
Peak	**Center**	**Height**	**FWHM**	**Other**	**Area**
1	1354.9	5293.1	48.1	0.601	321808.4
2	1582.8	13890.5	29.04	0.1311	605128.1
3	1620.3	2558.4	26.9	0.5058	90491.07

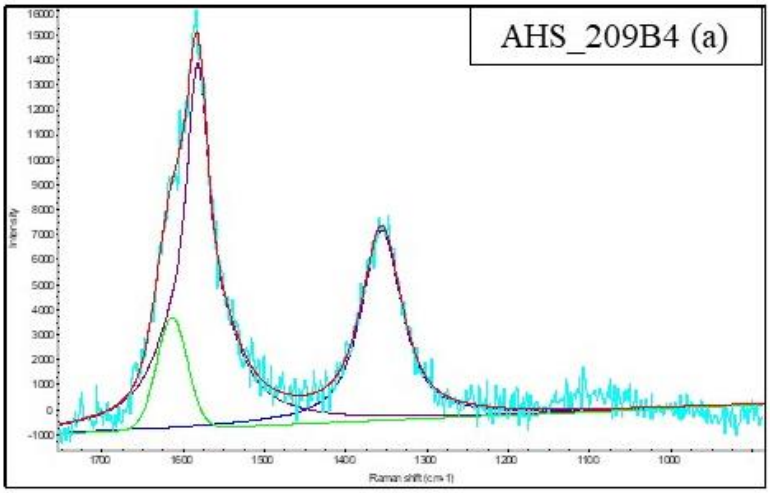
AHS_209B4 (a)
Intensity
Raman shift (cm-1)

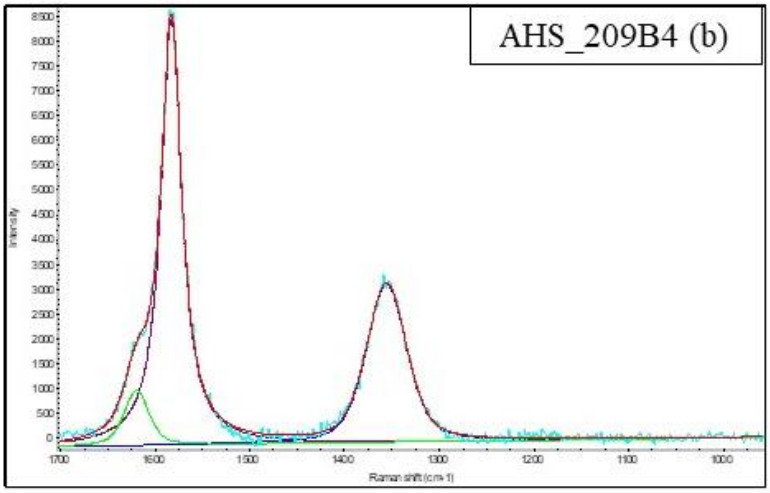
AHS_209B4 (b)
Intensity
Raman shift (cm-1)

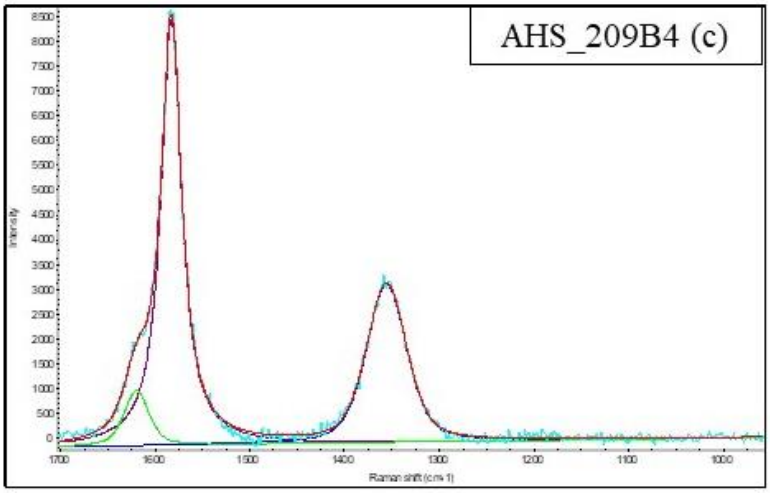
AHS_209B4 (c)
Intensity
Raman shift (cm-1)

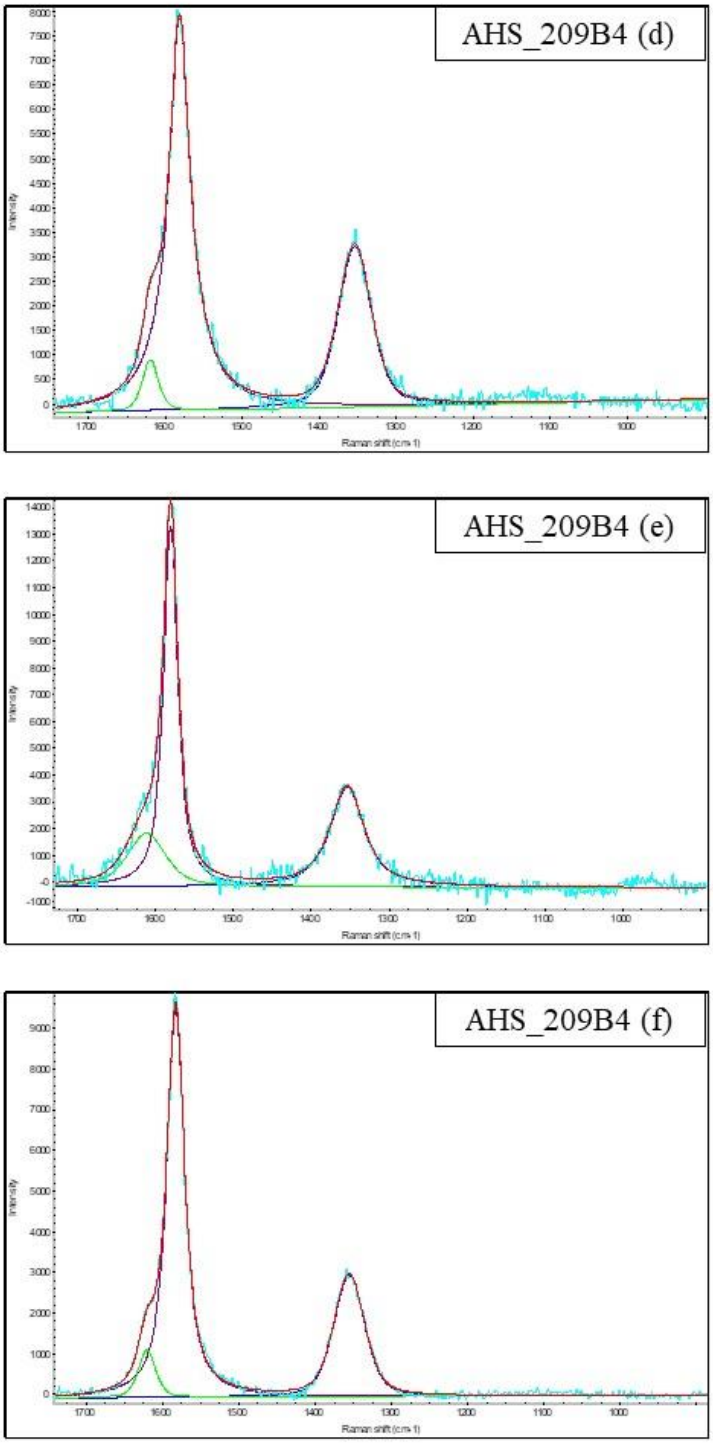

Figures B 3) Raman spectrum of AHS_209B4 sample: Raman acquisition (a), (b), (c), (d), (e) and (f)

Tab B13) Data collected during fit peaks of Raman spectrum of AHS_209B4 samples in (a) acquisition (50x mag; 514nm):

AHS_ 209B4 (a)					
Peak	**Center**	**Height**	**FWHM**	**Other**	**Area**
1	1354.9	7624.7	59.9	0.1963	668370.8
2	1581.2	14647.6	43.4	-0.5351	1164605
3	1612.9	4490.9	44.1	1	210997.1

Tab B14) Data collected during fit peaks of Raman spectrum of AHS_209B4 samples in (b) acquisition (50x mag; 514nm):

AHS_ 209B4 (b)					
Peak	**Center**	**Height**	**FWHM**	**Other**	**Area**
1	1354.9	3204.8	49.9	0.5833	203554.5
2	1582.6	8628.8	26.4	0.0209	355261.4
3	1619.4	1125.6	31.2	0.464	46870.44

Tab B15) Data collected during fit peaks of Raman spectrum of AHS_209B4 samples in (c) acquisition (50x mag; 514nm):

AHS_ 209B4 (c)					
Peak	**Center**	**Height**	**FWHM**	**Other**	**Area**
1	1354.1	4561.2	47.4	0.5104	282967.7
2	1581.9	11622.1	24.70	0.2243	417484.2
3	1618.3	1615.5	29.7	0.5049	62941.12

Tab B16) Data collected during fit peaks of Raman spectrum of AHS_209B4 samples in (d) acquisition (50x mag; 514nm):

AHS_ 209B4 (d)					
Peak	**Center**	**Height**	**FWHM**	**Other**	**Area**
1	1353.2	3273.3	51.0	0.5888	211874.1
2	1580.9	8028.9	34.9	-0.1824	463592
3	1618.9	1054.7	24.5	0.5235	33634.52

Tab B17) Data collected during fit peaks of Raman spectrum of AHS_209B4 samples in (e) acquisition (50x mag; 514nm):

AHS_ 209B4 (e)					
Peak	**Center**	**Height**	**FWHM**	**Other**	**Area**
1	1353.2	3753.7	52.1	0.1826	287755
2	1580.1	13519.2	22.3	0.2044	442705.4
3	1611.3	2002.9	58.2	0.4428	156364.7

Tab B18) Data collected during fit peaks of Raman spectrum of AHS_209B4 samples in (f) acquisition (50x mag; 514nm):

AHS_ 209B4 (f)					
Peak	**Center**	**Height**	**FWHM**	**Other**	**Area**
1	1354.2	3001.3	47.7	0.601	181027.5
2	1582.1	9697.1	28.1	0.1549	405979.3
3	1619.8	1174.9	27.0	0.4969	41835.06

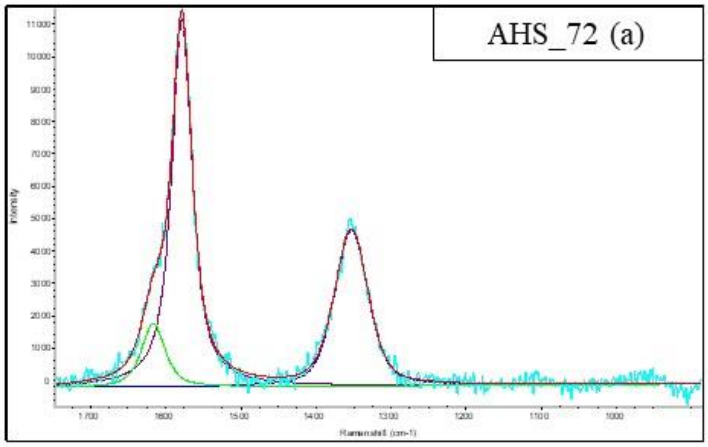
AHS_72 (a)

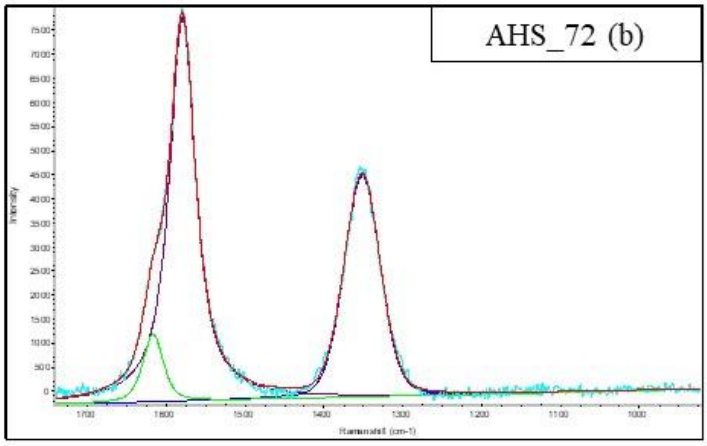
AHS_72 (b)

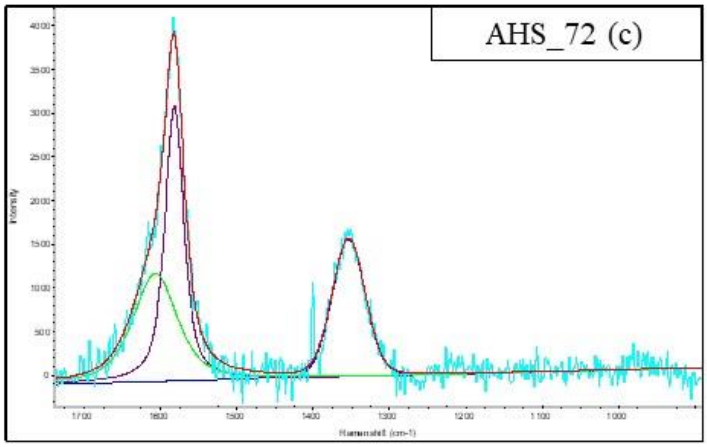
AHS_72 (c)

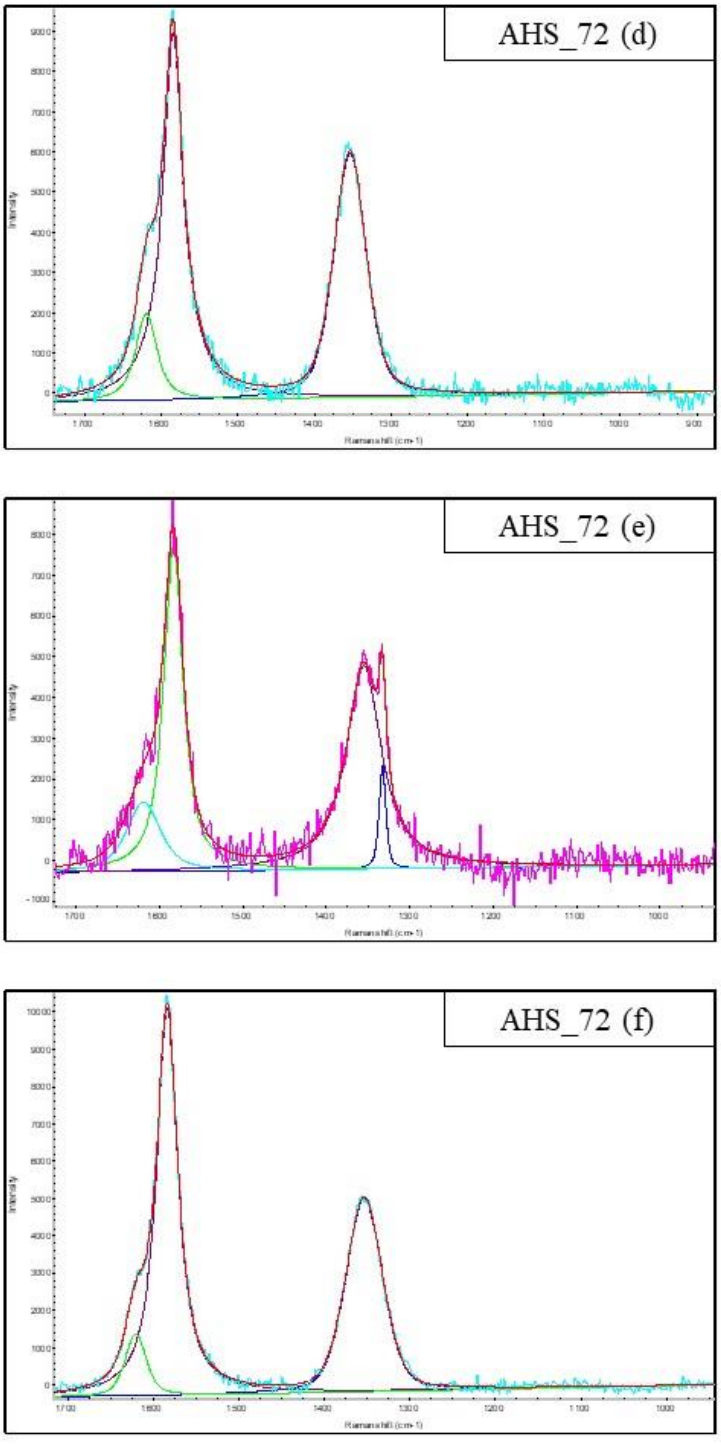

Figures B 4) Raman spectrum of AHS_72 sample: Raman acquisition (a), (b), (c), (d), (e) and (f)

Tab B19) Data collected during fit peaks of Raman spectrum of AHS_72 samples in (a) acquisition (50x mag; 514nm):

AHS_72 (a)					
Peak	**Center**	**Height**	**FWHM**	**Other**	**Area**
1	1351.8	4818.5	52.9	0.6022	321884.8
2	1577.5	11381.6	32.6	0.1617	550667.5
3	1615.7	1964.0	37.3	0.3712	101031.9

Tab B20) Data collected during fit peaks of Raman spectrum of AHS_72 samples in (b) acquisition (50x mag; 514nm):

AHS_72 (b)					
Peak	**Center**	**Height**	**FWHM**	**Other**	**Area**
1	1350.7	4602.2	53.7	0.8173	285483.9
2	1578.9	7996.3	39.6	0.1181	476515.8
3	1616.3	1405.5	30.7	0.5009	56715.79

Tab B21) Data collected during fit peaks of Raman spectrum of AHS_72 samples in (c) acquisition (50x mag; 514nm):

AHS_72 (c)					
Peak	**Center**	**Height**	**FWHM**	**Other**	**Area**
1	1352.9	1574.9	50.8	0.8884	89546.76
2	1581.3	3166.7	29.1	0.3692	127387.4
3	1606.4	1241.0	68.4	0.4226	114807.3

Tab B22) Data collected during fit peaks of Raman spectrum of AHS_72 samples in (d) acquisition (50x mag; 514nm):

AHS_72 (d)					
Peak	**Center**	**Height**	**FWHM**	**Other**	**Area**
1	1352.3	6100.2	49.7	0.594	384023.3
2	1583.7	9181.3	32.5	-0.1687	491833.7
3	1618.7	2171.7	33.2	0.2514	103698.8

Tab B23) Data collected during fit peaks of Raman spectrum of AHS_72 samples in (e) acquisition (50x mag; 514nm):

AHS_72 (e)					
Peak	**Center**	**Height**	**FWHM**	**Other**	**Area**
1	1332.1	2581.9	9.70	0.4969	33046.86
2	1354.4	4994.1	50.6	0.0768	385239
3	1582.7	7967.6	28.2	0.1374	335871.8
4	1618.7	1702.1	48.3	0.3772	113194.5

Tab B24) Data collected during fit peaks of Raman spectrum of AHS_72 samples in (f) acquisition (50x mag; 514nm):

AHS_72 (f)					
Peak	**Center**	**Height**	**FWHM**	**Other**	**Area**
1	1352.6	5187.1	50.5	0.7032	317754.5
2	1582.9	10415.2	30.0	0.0623	479550.6
3	1619.7	1673.4	29.0	0.485	64262.34

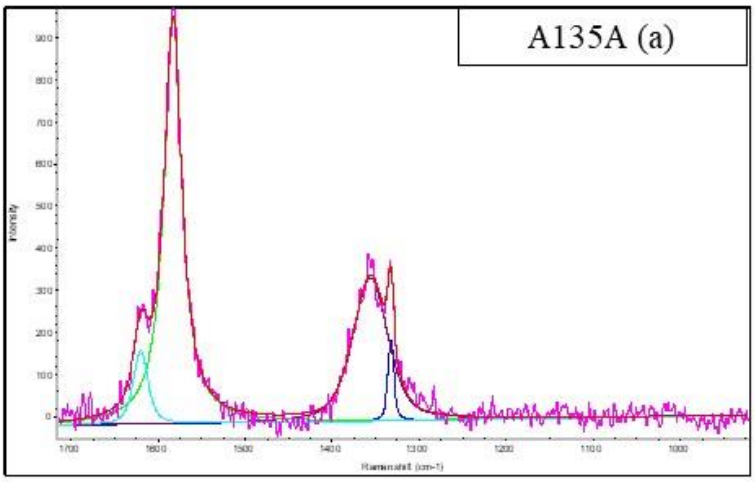
A135A (a)

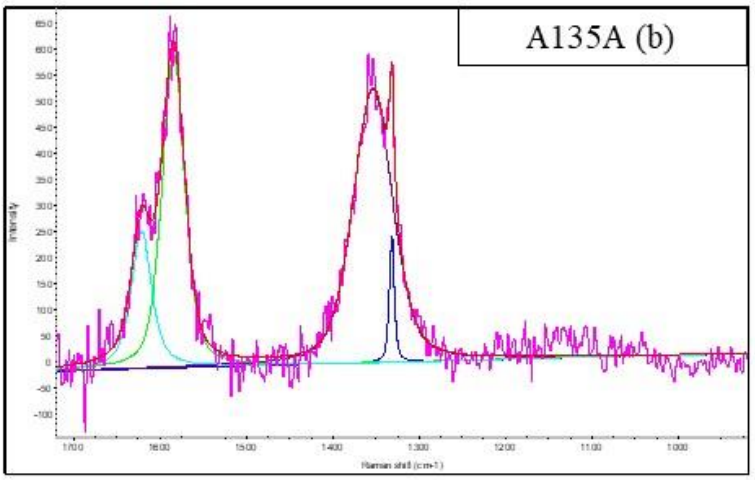
A135A (b)

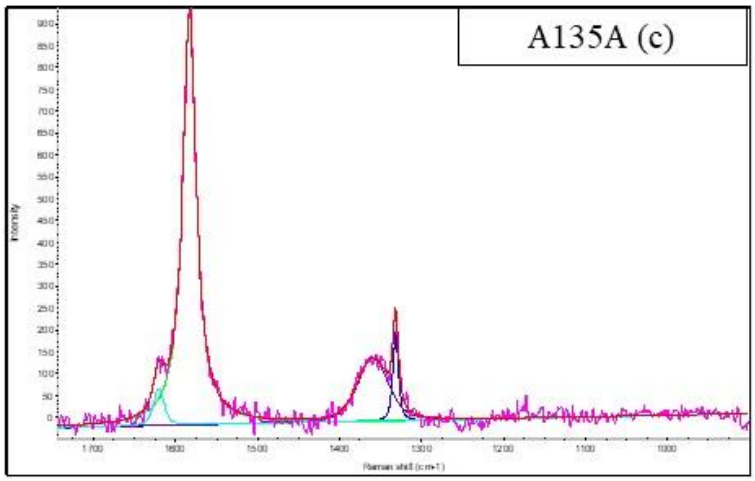
A135A (c)

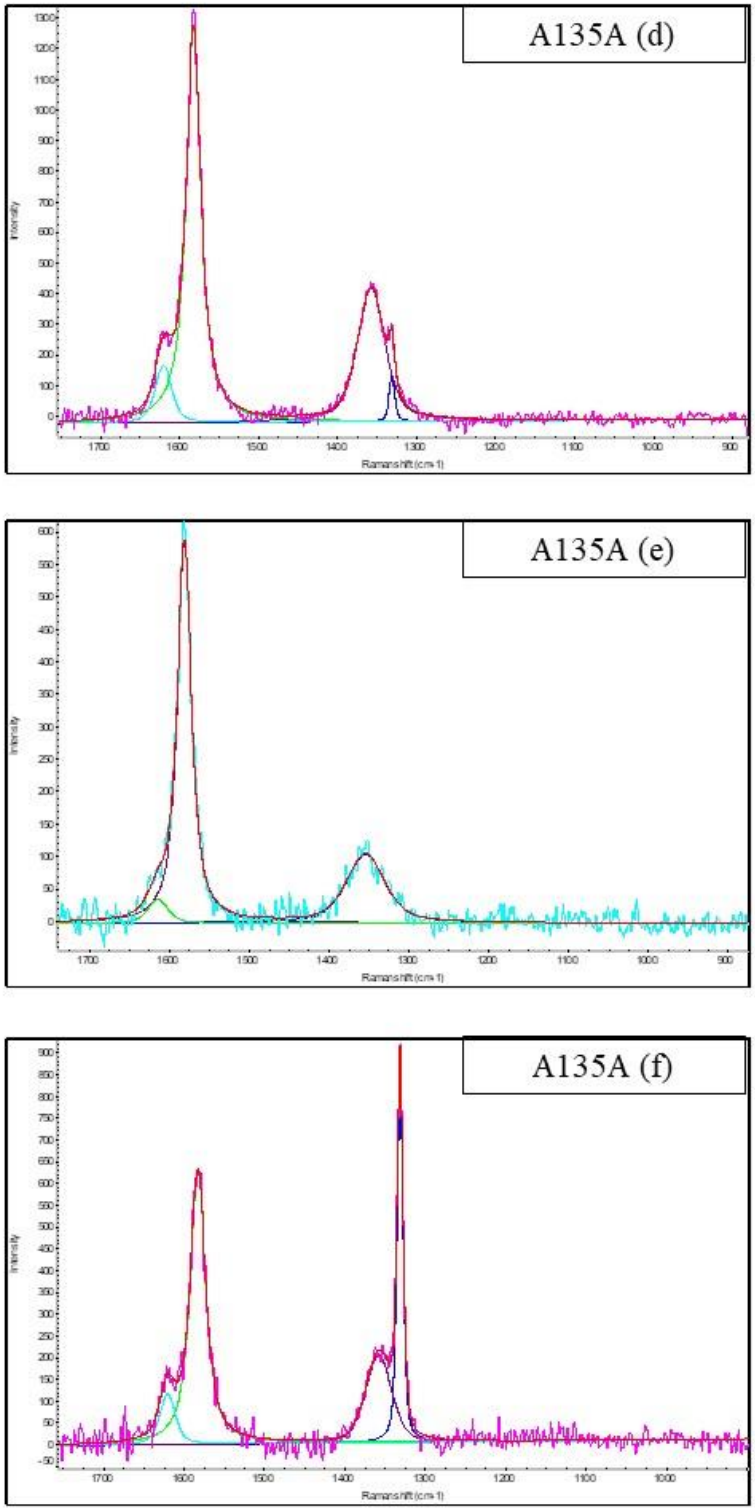

Figures B 4) Raman spectrum of A135A sample: Raman acquisition (a), (b), (c), (d), (e) and (f)

Tab B25) Data collected during fit peaks of Raman spectrum of A135A samples in (a) acquisition (100x mag; 514nm):

A135A (a)					
Peak	**Center**	**Height**	**FWHM**	**Other**	**Area**
1	1331.6	196.9	7.8279	0.4705	2045.349
2	1355.2	341.2	47.6817	0.5516	20946.48
3	1582.4	964.7	24.8648	0.0358	37139.36
4	1619.6	175.4	19.927	0.4353	4713.68

Tab B26) Data collected during fit peaks of Raman spectrum of A135A samples in (b) acquisition (100x mag; 514nm):

A135A (b)					
Peak	**Center**	**Height**	**FWHM**	**Other**	**Area**
1	1330.7	249.8	6.8	0.4517	2582.522
2	1352.7	524.9	54.0	0.6362	35326.6
3	1583.8	604.1	30.9	0.5592	24054.15
4	1620.9	265.3	28.1	0.3181	10470.16

Tab B27) Data collected during fit peaks of Raman spectrum of A135A samples in (c) acquisition (100x mag; 514nm):

A135A (c)					
Peak	**Center**	**Height**	**FWHM**	**Other**	**Area**
1	1330.7	208.8	8.0	0.485	2217.688
2	1358.3	144.6	44.7	0.6213	8110.662
3	1582.1	952.3	19.7	-0.0246	29670.35
4	1619.8	85.9	15.2	0.5055	1710.535

Tab B28) Data collected during fit peaks of Raman spectrum of A135A samples in (d) acquisition (100x mag; 514nm):

A135A (d)					
Peak	**Center**	**Height**	**FWHM**	**Other**	**Area**
1	1330.4	148.4	8.2	0.4838	1612.919
2	1356.7	436.6	41.0	0.46	23911.81
3	1581.7	1294.7	22.2	0.0526	44283.46
4	1619.8	187.3	24.7	0.5153	6041.381

Tab B29) Data collected during fit peaks of Raman spectrum of A135A samples in (e) acquisition (100x mag; 514nm):

A135A (e)					
Peak	**Center**	**Height**	**FWHM**	**Other**	**Area**
1	1353.5	106.5	57.1	0.4373	8174.414
2	1580.5	589.1	21.2	0.1617	18598.93
3	1613.7	36.3	30.1	0.5417	1413.388

Tab B30) Data collected during fit peaks of Raman spectrum of A135A samples in (f) acquisition (100x mag; 514nm):

A135A (f)					
Peak	**Center**	**Height**	**FWHM**	**Other**	**Area**
1	1330.6	866.9	8.8	0.5402	9916.664
2	1357.2	200.7	38.3	0.6806	9394.508
3	1582.3	628.9	23.1	0.1877	21367.85
4	1620.1	117.3	22.8	0.4764	3536.358

Appendix C: *Micro-XR Powder Diffraction analyses*

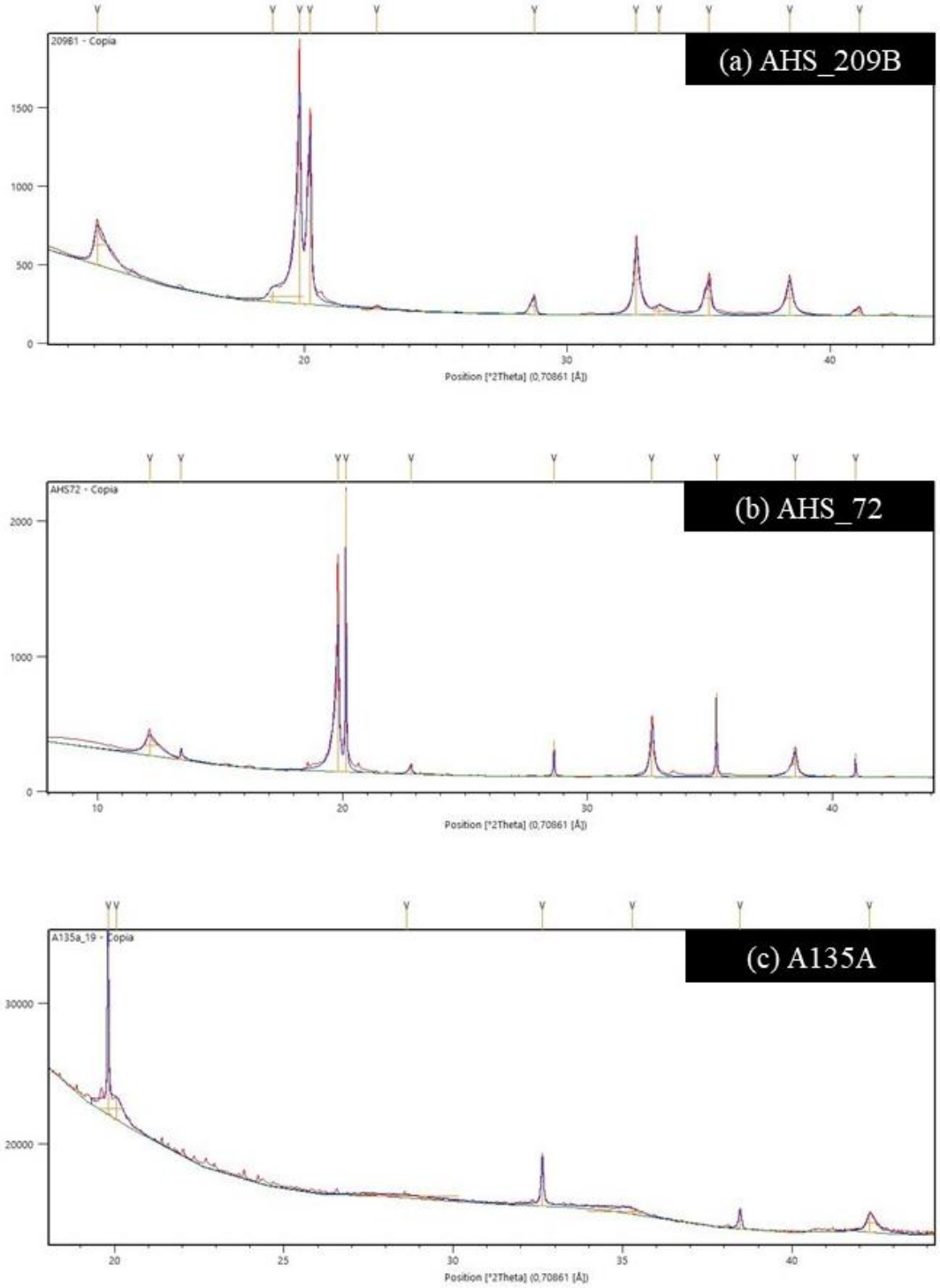

Figures C 1) Line profile analysis fitting of diffractogram of AHS_209B (a), AHS_72 (b) and A135A samples (c).

RINGRAZIAMENTI:

La fine di questo percorso ormai è giunta. Questi due anni di laurea magistrale sembrano esser volati via, anni molto belli e ricchi di emozioni, di soddisfazioni e di accrescimento personale.

Per la riuscita di questa tesi magistrale un mio primo grande ringraziamento va al Professor Nestola che mi ha accompagnata in ambedue le tesi di laurea e che è riuscito a trasmettermi il suo grande entusiasmo per la ricerca scientifica, incrementando ancora di più quello che già mi apparteneva, e con il quale sarò felicissima di continuare a lavorare.
Questo entusiasmo ha potuto prender vita soprattutto nel corso dello svolgimento della tesi magistrale che è stata per me un'esperienza unica e che mi ha messo a diretto contatto con il mondo della ricerca, il quale mi ha lasciato affascinata.
Ringrazio inoltre il gruppo di Pavia con cui abbiamo lavorato in questi mesi, in particolare la Prof. Maria Chiara Domeneghetti, il Prof. Matteo Alvaro, Marta Morana e Mara Murri.

Un enorme grazie va alla mia famiglia, in particolare alla mia mamma Stefania e alla mia sorellona Elena che sono le donne più forti che conosca, sono state sempre presenti in ogni momento e in grado di aiutarmi e supportarmi in ogni difficile istante di questo percorso: mi hanno insegnato a reagire alle difficoltà spronandomi sempre a fare del mio meglio; un grande grazie va alla mia zia Uccia, sempre pronta ad ascoltarmi e darmi un consiglio, alla mia nonna Olga, per il supporto morale con tutte le fantastiche leccornie che mi prepara, e al mio nonno Emilio che sempre mi hanno sostenuta e aiutata a far fronte a questi intensi anni di studio. Ringrazio tanto anche Omar che è sempre pronto a farmi ridere ed in grado di strapparmi un sorriso anche quando non ne avrei voglia. Un grazie anche alla nonna Linda.

Ringrazio ora il mio Riccardo, un punto di riferimento per me e la mia serenità e che ogni giorno di più mi accorgo essere essenziale per la mia felicità; anche in questa occasione ha saputo essere sempre di grande aiuto per affrontare i vari

ostacoli, per poi esserne felici insieme al raggiungimento dell'obbiettivo. Un grazie sincero per avermi supportato, e il più delle volte, sopportato in tutti questi anni universitari.
Questa tesi la dedico alla mia famiglia, sperando di avervi reso orgogliosi di me e sperando che con questo lavoro avrei potuto render orgoglioso anche chi purtroppo in questo giorno di felicità e soddisfazione non può essere qui insieme a noi…

Passiamo ora agli squinternati dei miei amici padovani:
Ringrazio in primis le mie due partners in the University, due amiche con cui fin dal primo anno son stata inseparabile, Sofia e Caterina che si sono "curate" (dopo 5 anni ormai avranno imparato un po' di veneziano) per la maggiore tutte le mie paranoie per gli esami con annesse le relative colazioni scaramantiche del mattino.
A Caterina e Sofia aggiungo anche Veronica, Silvia, ("Puli" per gli amici, che poi la gente non capisce) Lucrezia e Ilaria per ringraziarle, oltre che per il sostegno nelle lunghe ore passate in biblioteca a studiare, anche per le mangiate al sushi e tutte le serate padovane trascorse insieme dove lanciare sarde per qualcuna non corrispondeva solo al nome del locale.
Un grazie particolare al team "I Cicci very tesi" di cui Sofia fa nuovamente parte e Leo, con cui ho affrontato questi intensi mesi di studio e questi giorni composti da "troppe poche ore" per finire la stesura della tesi. Le chat delle 5 del mattino (insieme alle Redbull) sono state essenziali per terminare questa tesi.
Un grazie a Calle e Menga per le vecchie serate mood "Mondo bueo" che tra versi di volpi, screwdriver, paste al tonno e cipolla e risotti non troppo cotti, navigli e NBA sono state irripetibili. Ringrazio Simone per averci insegnato che il limite alla lesità mentale è raggiunto solo alla completa trasformazione in fenicottero.

Ringrazio ora in toto, tutto il fantastico gruppo di colleghi e amici che ho conosciuto qui a Geologia, si è creato un bellissimo clima di amicizia e divertimento che ha aiutato non poco durante i momenti caratterizzati da alta tensione di questi anni (che non sono stati pochi).

Ringrazio le mie coinquiline con cui in questi anni ho convissuto a Padova, conoscere persone nuove e provare l'esperienza della convivenza è stata un'esperienza molto bella. Durante questi anni ho conosciuto persone meravigliose, e tra queste ringrazio in particolare Giulia e Elena con cui ho condiviso la stanza e con cui mi scuso per l'immane casotto presente in camera che cresceva esponenzialmente ogni volta in cui si avvicinava l'avvento della sessione.

Passiamo in quel di Venezia:
Ringrazio la mia poppiera Elisa con cui in quest'anno ricco di impegni ho tentato di dedicarmi nuovamente alla nostra comune passione per la voga alla veneta; un grazie di cuore per tutte le mattine in cui ti sei alzata presto per me per farmi studiare e per tutte le ansie esami/tesi che ti sei dovuta subire (mi farò perdonare con ulteriori uscite con pizzette). Ringrazio Matteo che oltre al "compagno di banco per eccellenza" ci ha aiutato molto in questo percorso di quest'estate.
Ringrazio i miei fantastici amici del liceo con cui mi sembra di essere uscita solo ieri dalle aule del Benedetti e con i quali a distanza di 10 anni (che vecci…) riusciamo ancora a ritrovarci uniti come un tempo anche senza il nemico comune della Bettio. Ringrazio in particolare, Alice e Angela, che malgrado le varie difficoltà logistiche mi hanno sempre supportata in questi anni.
Ringrazio la Elly e Doneddu una coppia di cari amici speciali che ringrazio per essermi stati vicini e aver gioito insieme a me per tutti i traguardi raggiunti.

Grazie mille a tutti quelli che hanno avuto il piacere di essere partecipi e presenti in questo giorno, per me molto importante.